

Journal of Energy Challenges and Mechanics

ISSN 2056-9386

<http://www.nscj.co.uk/JECM/>

Volume 2, Issue 2
September 2015



Featured article:

Hydrothermal carbonization of sewage sludge on industrial scale: energy efficiency, environmental effects and combustion

*Matthias Stucki, Lea Eymann, Gabriel Gerner, Frank Hartmann, Rahel Wanner and Rolf Krebs**

Institute of Natural Resource Sciences, Zurich University of Applied Sciences, Campus Grüental, CH-8820, Wädenswil, Switzerland

Journal of Energy Challenges and Mechanics, volume 2, pages 38-44.



North Sea Conference & Journal LTD
2 Charlestown Walk, Cove Bay, AB12 3EZ, Aberdeen, Scotland, United Kingdom
<http://www.nscj.co.uk/JECM/> | jecm@nscj.co.uk | +44(0)1224 875635



TABLE OF CONTENTS

pages

[Article 1](#): GASFLOW simulations for cryogenic tank loss of vacuum scenarios 29-37
J.R. Travis¹ and D. Piccioni Koch^{2}*

¹*Engineering & Scientific Software, Inc., 2128 S. Ensenada Circle, Rio Rancho, NM 87124, USA*

²*Steinbuch Centre for Computing (SCC), Karlsruhe Institute of Technology (KIT), Postfach 3640, 76021 Karlsruhe, Germany*

[Article 2](#): Hydrothermal carbonization of sewage sludge on industrial scale: energy efficiency, environmental effects and combustion 38-44

Matthias Stucki¹, Lea Eymann¹, Gabriel Gerner¹, Frank Hartmann¹, Rahel Wanner¹ and Rolf Krebs^{1}*

¹*Institute of Natural Resource Sciences, Zurich University of Applied Sciences, Campus Grüental, CH-8820, Wädenswil, Switzerland*

[Article 3](#): Identification of Lithium-Ion Physics-Based Model Parameter Values 45-55

*Ryan Jobman, M. Scott Trimboli, and Gregory L. Plett**

Department of Electrical and Computer Engineering, University of Colorado Colorado Springs, Colorado Springs, CO 80918, USA

[Article 4](#): Governing the market entry of marine energy by symptom-adapted interventions: (i) Reduction of detail complexity; and (ii) Managing dynamically complex tasks 57-61

Ralf Bucher^{1}, Ian Bryden²*

¹*University of Edinburgh, Institute for Energy Systems, Mayfield Road, Edinburgh, EH9 3JL, UK*

²*University of the Highlands and Islands, Ness Walk, Inverness, IV3 5SQ, UK*

[Article 5](#): Law of inertia and the primal energy in the cellular automaton universe 62-67

Simon Berkovich

Department of Computer Science, The George Washington University, Washington, DC 20052, USA

[Article 6](#): On the optimisation of a cylinder/plate configuration with the aim to improve the energy harvesting of vortex induced vibrations 68-74

Till Biedermann, Frank Kameier, Robert Heinze*

Institute of Sound and Vibration Engineering ISAVE, University of Applied Sciences Duesseldorf, Duesseldorf 40474, Germany



GASFLOW simulations for cryogenic tank loss of vacuum scenarios

用 GASFLOW 模拟真空环境下低温罐损失

J.R. Travis¹ and D. Piccioni Koch^{2*}

¹ Engineering & Scientific Software, Inc., 2128 S. Ensenada Circle, Rio Rancho, NM 87124, USA

² Steinbuch Centre for Computing (SCC), Karlsruhe Institute of Technology (KIT), Postfach 3640, 76021 Karlsruhe, Germany

daniela.piccioni@kit.edu

Accepted for publication on 27th February 2015

Abstract - The Computational Fluid Dynamic (CFD) code GASFLOW was used to simulate Loss of Vacuum scenarios for studying the safety performance of high-pressure hydrogen vessels for vehicular storage applications. For these simulations, the real gas equations of state (EoS) for hydrogen based on the Leachman's NIST reference model and a modified van der Waals model were used. The GASFLOW simulations show good agreement with previous simulation results and with data.

Keywords – Computational Fluid Dynamic Code, Real Gas Equations of State for Hydrogen, High-pressure Hydrogen Vessel Loss of Vacuum, Hydrogen Energy.

I. INTRODUCTION

Hydrogen represents one of the most favorable gases as a future alternative energy source. However, in the automotive field, several challenges must be overcome before the introduction of hydrogen fuel cell vehicles on a large scale can become possible. One key hurdle is the development of efficient and safe hydrogen storage technologies and, in particular, the realization of high-pressure hydrogen vessels for long term viability.

The Computational Fluid Dynamic (CFD) code GASFLOW [1, 2, 3] was used to simulate Loss of Vacuum scenarios for studying the safety performance of high-pressure hydrogen vessels for vehicular storage applications. The simulations presented in this paper were carried out in the frame of the “CryoSys” project [4], whose partners were the Bayerische Motoren Werke (BMW) Group, the Karlsruhe Institute of Technology (KIT), AIRBUS Operations and ET Energie Technologie. The main aim of this project was the development of Cryo-compressed Hydrogen (CCH₂) vessels for automotive applications (CryoSys vessels) and, in particular, the realization of Al-liner carbon-fiber/epoxy tanks of Type III [5]. GASFLOW has been extended to include real

gas equations of state (EoS) for hydrogen [6,7]. These EoS options include Leachman's NIST reference model [8, 9] and a modified van der Waals model [6,7].

Three simulations are presented in this paper as Loss of Vacuum representative:

1. For a reference case, the outer steel shell of the vessel is removed and the Carbon-Fiber-Epoxy (CFE) surface is directly exposed to ambient air;
2. The outer shell is intact, but there is outside loss of vacuum with the ambient air leaking into the annulus; and
3. The outer shell is intact, but there is inside loss of vacuum with hydrogen leaking from the tank into the annulus.

An exact solution for constant volume heating can be found for various initial conditions. Another exact solution for an ideal discharge, the isentropic solutions, can be found for the cryogenic tank blowdown into the vacuum volume. The time required to achieve the equilibrium state is simulated and presented.

All heating solutions require a temperature-dependent natural convective heat transfer coefficient model to account for the outer surface, either CFE or outer Aluminum shell, boundary condition; this accounts for the cryogenic tank cylindrical geometry interacting with ambient air conditions at 1 atmosphere and 300 K. This model has been implemented into GASFLOW and is described in detail in this paper.

The GASFLOW simulations show good agreement with previous simulation results and with data.

II. AN EXACT SOLUTION HEATING MODEL

The idea behind the exact heating solution is that in a loss of vacuum situation, the insulation of the tank is no longer functioning because ambient air leaks in the vacuum space. In

time, no matter what the heat transfer, the tank will warm to the ambient temperature (300 K) and the pressure in the tank will be as the exact heating model solution shows. Leachman's

NIST hydrogen equation of state [8, 9] can be used to compute an exact solution for constant volume heating. We present the solution in the following manner:

1. Select an initial temperature; for example, 40 K.
2. Select a range of initial pressures; for example, 2.5 MPa to 25 MPa in increments of 2.5 MPa.
3. Compute the hydrogen densities for the selected initial temperature and each pressure value by inverting the NIST pressure equation

$$p = p(\rho, T). \quad (1)$$

4. Select a final temperature; for example, 300 K, or select a final pressure; for example 40.2 MPa (when the mechanical safety vent opens [10]).

5. Compute the final pressure using the selected final temperature or compute the final temperature using the selected final pressure and the hydrogen densities found in step 3.

We have plotted this exact heating solution in Figures 1 and 2.

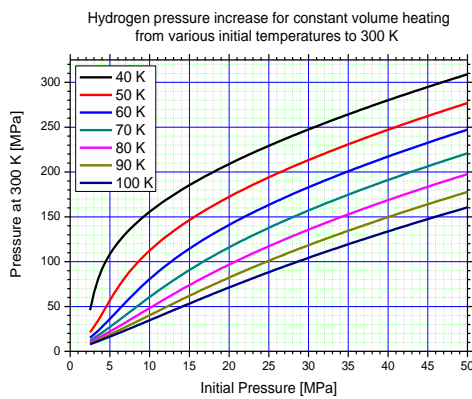


Figure 1. An exact pressure solution for hydrogen constant volume heating from a given initial temperature and pressure to the final temperature at 300 K.

An example can be demonstrated by selecting an initial pressure 30 MPa and temperature 65 K, and then reading from Figure 1, we see the final pressure is roughly 170 MPa (actually 169.46 MPa).

Perhaps a more relevant representation of this exact heating solution is to select the final pressure based on the opening of the mechanical safety vent at 40.2 MPa \pm 3% [10]. Figure 2 gives this result.

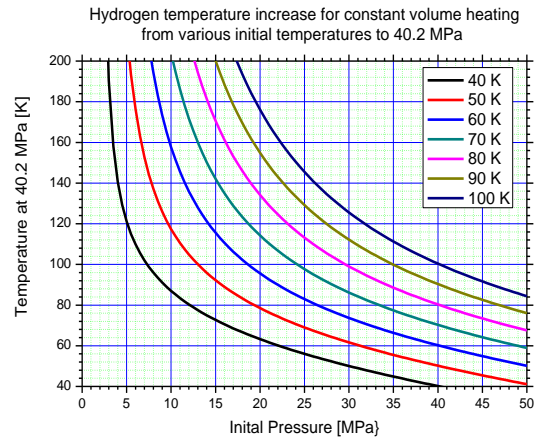


Figure 2. An exact temperature solution for hydrogen constant volume heating from a given initial temperature and pressure to the final pressure at 40.2 MPa.

The same example as before (initial conditions: 30 MPa and 65 K) shows that heating the CryoSys Tank from 65 K to 80 K increases the pressure to 40.2 MPa where the mechanical safety vent opens to protect the integrity of the tanks.

III. GASFLOW CRYOSYS TANK GEOMETRIC MODEL, INITIAL CONDITIONS, AND BOUNDARY CONDITIONS

The GASFLOW geometric model is a right-circular cylinder. The inner diameter is 279 mm and the length is 1872.87 mm yielding a free volume of 114.5 liters. The interior structures have been removed for simplicity. The mesh consists of 3 radial cells, 13 azimuthal cells, and 52 axial cells for a total of 2,028 cells. As a mesh convergence test, we doubled the number of cells in each coordinate (6 radial, 26 azimuthal, 104 axial: totally 16,224 cells without significant differences between the coarse and medium mesh representation.

For all reported simulations, the initial conditions inside the tank are: pressure 30 MPa, temperature 65 K, and density 66.253 kg/m³.

The boundary conditions are as follows:

1. For the case where the outer steel shell is removed, the tank wall is a composite structure with 4.0 mm aluminum and 9.5 mm carbon-fiber epoxy.
2. For the case where the outer aluminum shell is intact but the annulus is filled with air to a volume equaling 40 liters (outside loss of vacuum) in less than 1 minute [10], the gap width is 15mm with a 4 mm outer aluminum shell.
3. For the case where the Aluminum shell is intact but the annulus is filled from the inside with hydrogen to a volume equaling 40 liters (inside loss of vacuum) through an orifice with a diameter of 0.18 mm [10].

In all cases, the outermost structural surface (CFE or Aluminum) is coupled to the ambient (0.101325 MPa and 300 K) with the natural convective heat transfer coefficient described below.

The first two cases, the reference bare CFE tank and the outside loss of vacuum, are straight forward simulations, while the inside loss of vacuum case is extremely complex. In the next section, we will focus our attention to the inside loss of vacuum scenario, and then return to the reference bare CFE tank and outside loss of vacuum in section V.

IV. INSIDE LOSS OF VACUUM

A. The Isentropic Scenario

As mentioned above, the CryoSys Tank, 114.5 liter volume, is initially at 30 MPa, 65 K, and 66.253 kg/m³, which gives an initial mass equaling 7.586 kg. Should one open an exit hole (assumed to be an orifice with a 0.18 mm diameter [10]), an isentropic expansion into the vacuum gap, 40 liter volume, would result in pressure equilibrium with average density equaling 49.1 kg/m³. Since the process is isentropic, one can readily find the exact final thermodynamic state for both tank and vacuum gap as 43.049 K and 5.6754 MPa. Table 1 provides a quick summary of the initial and final states.

Table 1. Summary of the Exact Isentropic Inside Loss of Vacuum Solution.

| CryoSys Tank | Vacuum Volume | Total Volume |
|--|---|---|
| 0.1145 m ³ | 0.040 m ³ | 0.1545 m ³ |
| P = 30 MPa T = 65 K ρ = 66.253 kg/m ³ | P = 0 MPa T = 0 K ρ = 0 kg/m ³ | P = 5.6754 MPa T = 43.049 K ρ = 49.10 kg/m ³ |

Figure 3 provides a simple schematic of the physical processes, namely the discharge or blowdown of the CryoSys Tank into the vacuum volume, while the T-S diagram in Figure 4 shows the stated processes: initial condition in the CryoSys Tank labeled “A”. initial condition in the vacuum volume labeled “E”, and the final or equilibrium condition labeled “B”.

The CryoSys Tank discharge and the vacuum volume filling are as follows:

A → B is the discharge path taken in the CryoSys Tank.

E → D shows that initially the discharge expansion into the vacuum volume results in temperatures and pressures less than the triple point, which would produce solid hydrogen.

D → C shows that as the vacuum volume filling continues a two-phase mixture of liquid and vapor occupies this volume. Figure 5 shows the quality and pressure as a function of temperature during this process. Note that near “D” a three-phase mixture can occur.

C → B is the vacuum volume vapor condition as the final equilibrium state is approached.

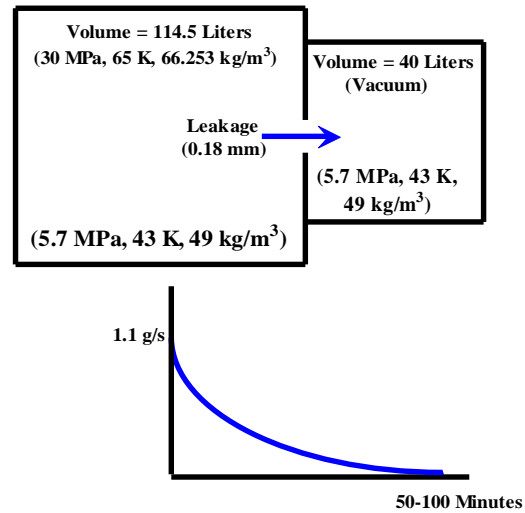


Figure 3. Schematic diagram illustrating the Inside Loss of Vacuum scenario.

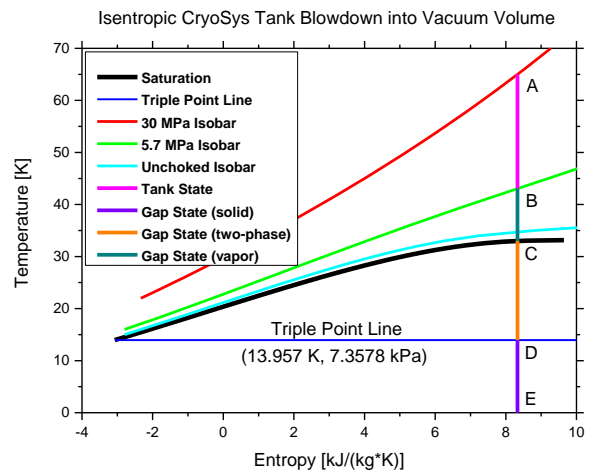


Figure 4. T-S diagram showing the Inside Loss of Vacuum thermodynamic paths.

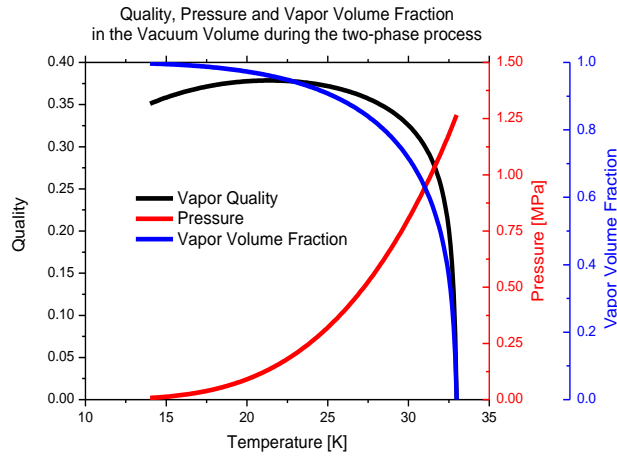


Figure 5. Quality, Pressure and Vapor Volume Fraction in the Vacuum Volume during the two-phase process (D \rightarrow C in Figure 4).

As the CryoSys Tank discharges, the flow is at first choked and then unchokes as will be seen later in this analysis. For references purposes, the unchoked isobar condition is presented in Figure 6. This means a choked discharge exists until the choked pressure decreases to the pressure in the vacuum volume, the unchoked isobar (1.77 MPa at 34.758 K), at which time the discharge becomes unchoked. It is clear that the discharge remains single phase at the discharge orifice and after unchoking the conditions in both volumes are single-phase.

We know the involved thermodynamic states, so what remains to find is the time to achieve these states. This requires determining the solution for the following system of equations for the conservation of mass and energy:

$$\frac{d}{dt}(\rho_T V_T) = -C_d \dot{m}_t \quad (2)$$

$$\frac{d}{dt}(\rho_T I_T V_T) = -C_d \dot{m}_t \left(h + \frac{V^2}{2} \right)_t \quad (3)$$

$$\frac{d}{dt}(\rho_{VV} V_{VV}) = C_d \dot{m}_t \quad (4)$$

$$\frac{d}{dt}(\rho_{VV} I_{VV} V_{VV}) = C_d \dot{m}_t \left(h + \frac{V^2}{2} \right)_t \quad (5)$$

During the discharge initial phase when the flow is choked, one can determine the choked or critical mass flow rate, \dot{m}_t , by solving the coupled equations [11]

$$s(T_T, \rho_T) = s(T_t, \rho_t) \quad (6)$$

$$2[h(T_T, \rho_T) - h(T_t, \rho_t)] = w(T_t, \rho_t)^2, \quad (7)$$

for the choked temperature, T_t , and density, ρ_t , and knowing the tank temperature, T_T , and density, ρ_T , gives the choked mass flow rate as

$$\dot{m}_t = \rho_t \cdot A \cdot w(T_t, \rho_t). \quad (8)$$

When the choke pressure, $p(T_t, \rho_t)$, is less than the vacuum volume pressure, $p(T_{VV}, \rho_{VV})$, the flow unchokes and the discharge velocity is found from

$$w(T_t, \rho_t) = \sqrt{2[h(T_t, \rho_t) - h(T_{VV}, \rho_{VV})]}, \quad (9)$$

where the unchoked mass flow rate is

$$\dot{m}_t = \rho_{VV} \cdot A \cdot w(T_t, \rho_t). \quad (10)$$

For the following solution of Equations (2-10), the discharge coefficient, C_d , is unity. In Figure 6 the time-dependent pressure is given for the CryoSys Tank, Vacuum Volume, and choked (unchoked) orifice pressure. Note that the flow becomes unchoked when the orifice pressure is less than the Vacuum Volume pressure. This occurs at approximately 2100 s.

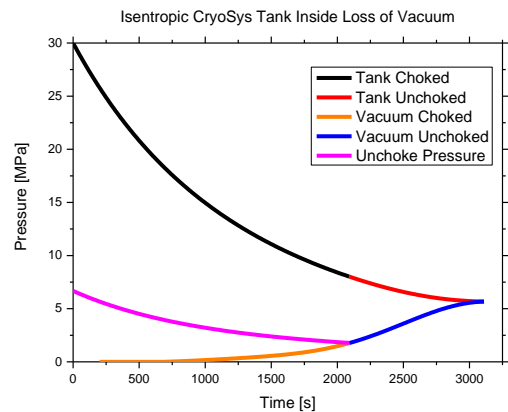


Figure 6. Time-dependent pressures for the isentropic Inside Loss of Vacuum solution of Equations (2-10).

In Figures 7-9, the densities, temperatures, and discharge mass flux are presented, respectively, for the isentropic Inside Loss of Vacuum solution of Equations (2-10).

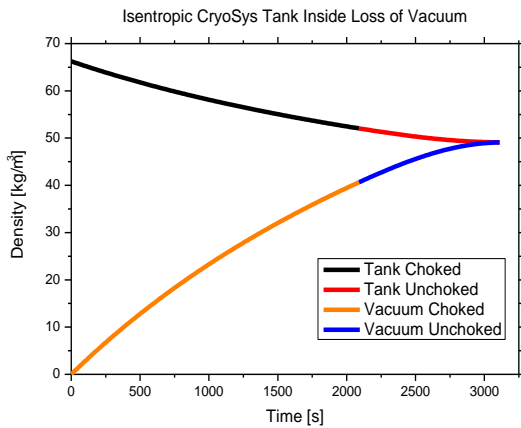


Figure 7. Time-dependent densities for the isentropic Inside Loss of Vacuum solution of Equations (2-10).

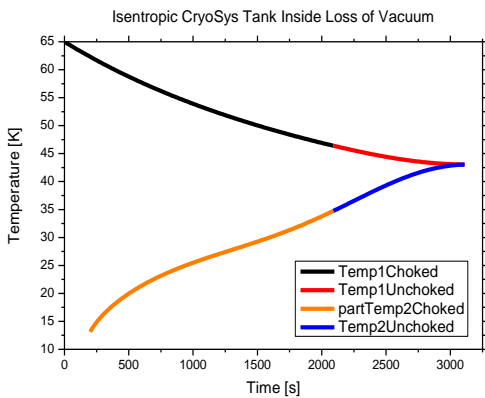


Figure 8. Time-dependent temperatures for the isentropic Inside Loss of Vacuum solution of Equations (2-10).

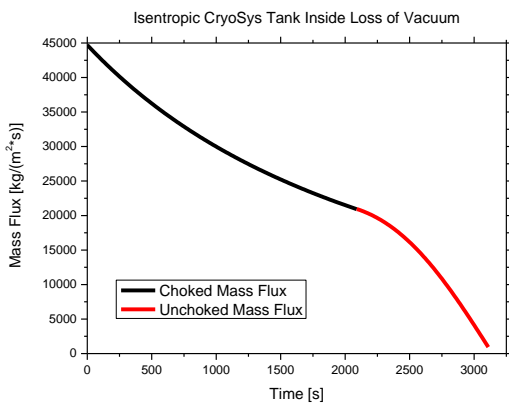


Figure 9. Time-dependent mass flux for the isentropic Inside Loss of Vacuum solution of Equations (2-10).

Observe that the final state is reached in about 3200 s with final state values identical to those given in Table 1. One can see from Figure 8 the timings for each of the vacuum volume processes given in Figure 4. We summarize these timings in Table 2.

TABLE 2. TABULATION OF THE VACUUM VOLUME PROCESSES SHOWN IN THE T-S DIAGRAM (FIGURE 4) AND OBSERVED IN FIGURE 8.

| Vacuum Volume processes shown in Figure 4 | Observed time from Figure 8 (seconds) |
|---|---------------------------------------|
| E → D: Solid-phase | 200 |
| D → C: Two-phase | 1675 |
| C → B: Single-phase | 1325 |
| TOTAL | 3200 |

B. The External Heat Transfer Scenario

In actuality, as the blowdown from the CryoSys Tank into the vacuum volume occurs, there is heat transferred to the outer Aluminum shell by natural convection from the ambient conditions (1 atmosphere at 300 K).

Hydrogen thermal conductivity will play a major role during the CryoSys heating. Using the serial mixing rule for multiphase mixtures, we construct a typical hydrogen temperature-dependent thermal conductivity in Figure 10 by using the discharge results presented above.

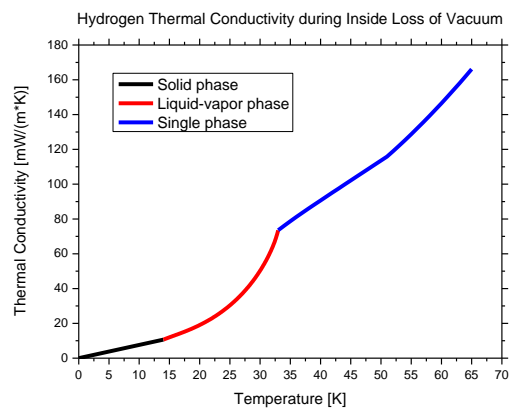


Figure 10. A typical Hydrogen temperature-dependent thermal conductivity behavior for the multiphase processes for the isentropic discharge scenario shown above.

Following the work of Spang [12], the average Nusselt Number for a horizontal cylinder is given by

$$Nu(T_m) = \frac{h \cdot D}{k(T_m)} = \left\{ \sqrt{Nu_0} + \left[\frac{Gr(T_m) \cdot Pr(T_m)}{300} \right]^{\frac{1}{6}} \right\}^2 ; Nu_0 = 0.36 , \quad (11)$$

$$\left[1 + \left(\frac{0.5}{Pr(T_m)} \right)^{\frac{9}{16}} \right]^{\frac{16}{9}}$$

where the Grashof Number is

$$Gr(T_m) = \frac{D^3 \cdot g \cdot \rho(T_m)^2 \cdot \beta(T_m) \cdot |T_{surf} - T_{amb}|}{\mu(T_m)^2} , \quad (12)$$

the Prandtl Number is

$$Pr(T_m) = \frac{\mu(T_m) \cdot c_p(T_m)}{k(T_m)} , \quad (13)$$

where all fluid properties are evaluated at the mean temperature

$$T_m = \frac{1}{2} (T_{surf} + T_{amb}) . \quad (14)$$

Correlation (Equation 11) is judged to be valid for

$$10^{-4} \leq Gr \cdot Pr \leq 4 \cdot 10^{14} \quad \text{and} \quad 0.022 \leq Pr \leq 7640 .$$

The air properties at 101.325 kPa are required to compute the time-dependent heat transfer coefficient between the CFE or steel shell surface and ambient conditions. These time-dependent properties are taken from Kays and Crawford [13]. Least Squares approximations have been found and are also shown in the following three Figures (11-13).

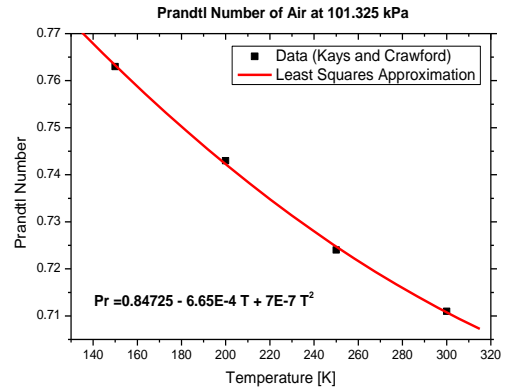


Figure 11. Air Prandtl Number as a Function of Temperature at 101.325 kPa.

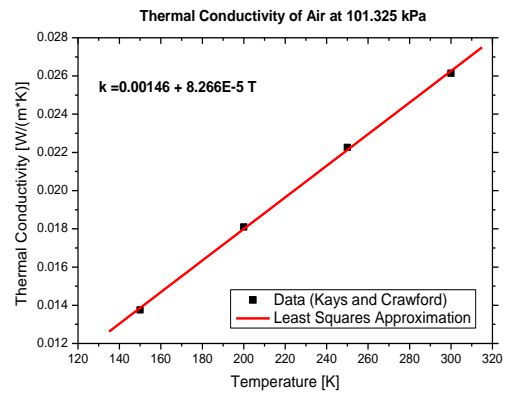


Figure 12. Air Thermal Conductivity as a Function of Temperature at 101.325 kPa.

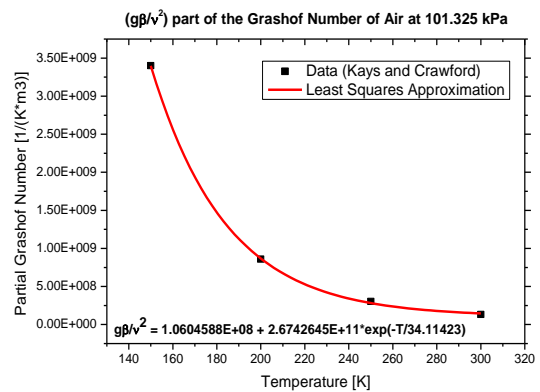


Figure 13. Air Partial Grashof Number as a Function of Temperature at 101.325 kPa.

A heat flow energy balance for a cylindrical system from the ambient conditions to the inside of the CryoSys Tank can be constructed as

$$q = \frac{2\pi L(T_{\infty} - T_{inside})}{\frac{1}{r_1 h_{inside}} + \frac{\ln(r_2/r_1)}{k_{Al}(T)} + \frac{\ln(r_3/r_2)}{k_{CFE}(T)} + \frac{\ln(r_4/r_3)}{k_{MII}(T)} + \frac{\ln(r_5/r_4)}{k_{Al}(T)} + \frac{1}{r_5 h_{outside}}} \quad (15)$$

where the temperature-dependent thermal conductivities are given in Figures 14-16 and the outside heat transfer coefficient, $h_{outside}$, is computed from Equation (11). Table 3 summarizes the geometry given in Equation (15).

TABLE 3. GEOMETRY DESCRIPTION GIVEN IN EQUATION (15)

| Radial Position | Distance (m) | Description |
|-----------------|--------------|---|
| r1 | 0.1395 | Inner CryoSys Tank $\leq r1$ |
| r2 | 0.1435 | $r1 \leq$ inner Al shell \leq $r2$ |
| r3 | 0.153 | $r2 \leq$ CFE \leq $r3$ |
| r4 | 0.168 | $r3 \leq$ MII \leq $r4$ |
| r5 | 0.172 | $r4 \leq$ outer Al shell \leq $r5$ |
| | | Ambient $\geq r5$ |

With nearly stagnation conditions in the CryoSys tank, the inside heat transfer coefficient, h_{inside} , can be approximated by $h_{inside} = k_{H2}/r_1$, where the single phase hydrogen thermal conductivity can be found as a function of pressure and temperature from Figure 17.

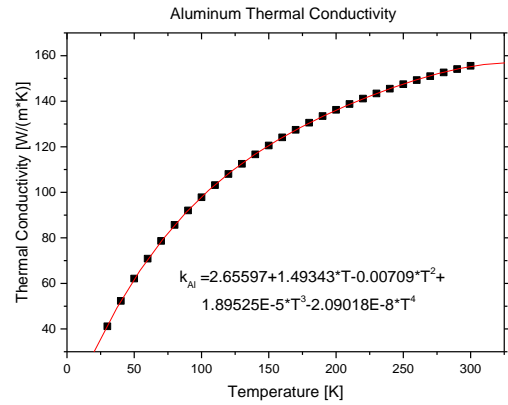


Figure 14. Aluminum thermal conductivity as a function of temperature.

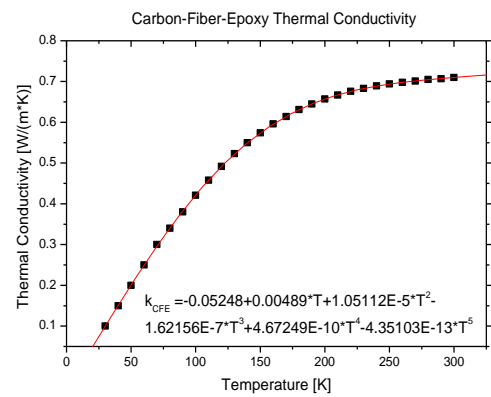


Figure 15. Carbon-Fiber-Epoxy thermal conductivity as a function of temperature.

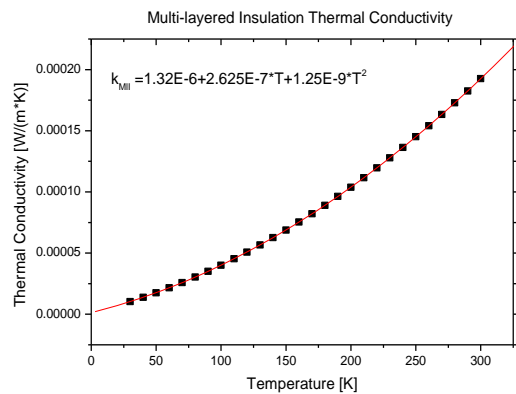


Figure 16. Multi-layered Insulation thermal conductivity as a function of temperature.

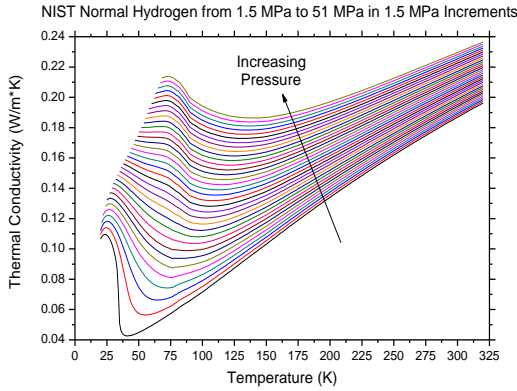


Figure 17. Single phase hydrogen thermal conductivity as a function of pressure and temperature.

As the discharge from the CryoSys Tank into the vacuum volume destroys the multi-layered insulation effectiveness, the thermal conductivity changes as a pure insulating material as shown in Figure 16 to a thermal conductivity described by Figure 10 in the multiphase states for temperatures less than 33 K. For temperatures greater than 33 K, the single phase thermal conductivity given in Figure 17 is incorporated into the analysis.

Since little is known about the discharge coefficient, we have simulated the inside loss of vacuum using three values; namely, 1.0, 0.6, and 0.3. The time-dependent internal CryoSys Tank pressure and average temperature are shown in Figures 18-19, respectively. Note the pressure in Figure 18 when the mechanical safety vent opens.

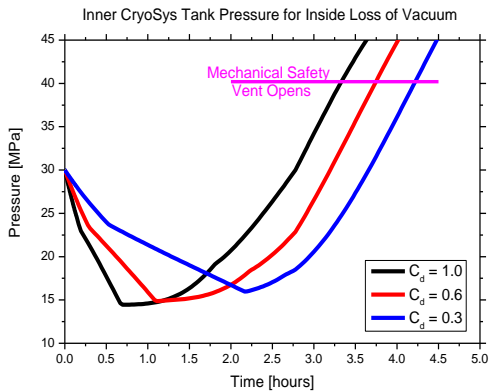


Figure 18. Inner CryoSys Tank pressure during the inside loss of vacuum for three discharge coefficients.

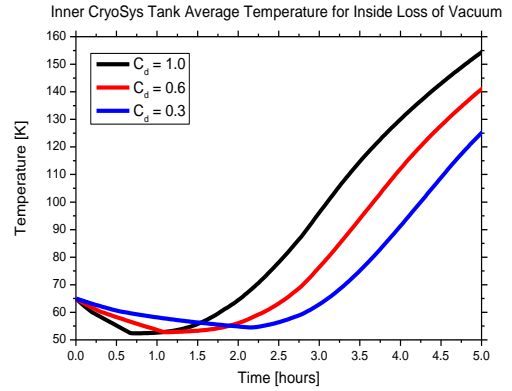


Figure 19. Inner CryoSys Tank average temperature during the inside loss of vacuum for three discharge coefficients.

The initial temperature of the outer Aluminum shell is nearly at the ambient temperature because of the multi-layered insulation’s super-efficiency. During the 5 hour simulation times presented in Figures 18-19, the outer shell is cooled by the very low temperature occurring in the vacuum volume. In Figure 20, we present the outer shell’s average temperature.

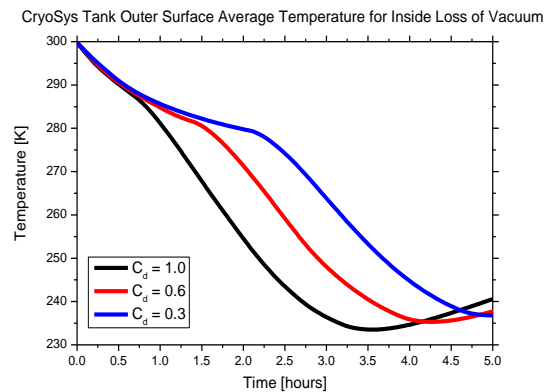


Figure 20. Outer shell average temperature during the inside loss of vacuum for three discharge coefficients.

V. BARE SHELL AND OUTSIDE LOSS OF VACUUM

The time-dependent CryoSys Tank pressures and average tank temperatures for the bare CFE shell and the inside loss of vacuum are presented in Figs. 21 and 22. The exact constant volume heating solution from Section II is seen to be fulfilled in both cases.

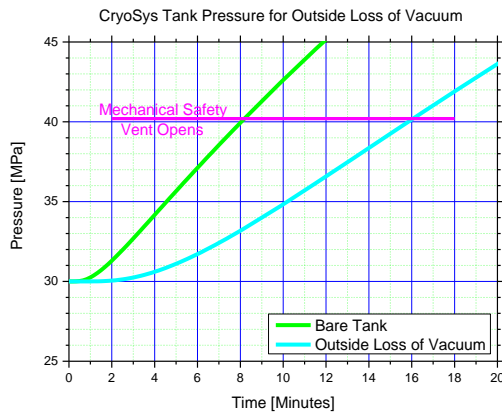


Figure 21. GASFLOW Outside Loss of Vacuum simulation for the CryoSys Tank Pressure.

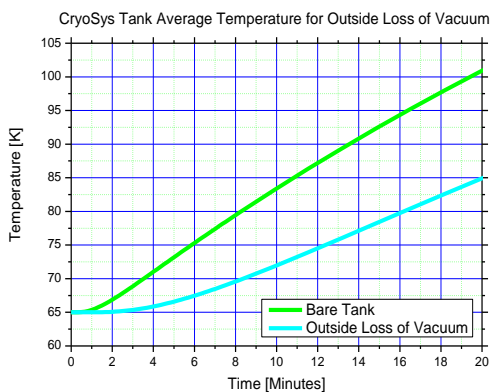


Figure 22. GASFLOW Outside Loss of Vacuum simulation for the CryoSys Tank Average Temperature.

VI. DISCUSSION

As expected, the fastest tank heating case is the bare CFE (steel shell removed) where the CFE surface is exposed directly to ambient conditions. The loss of vacuum from inside, where hydrogen fills the annulus, heats and pressurizes faster than the loss of vacuum from outside, where air fills the annulus.

With the thermal diffusivity for hydrogen being roughly 7 times that of air, the loss of vacuum heating time for the air filled annulus is longest, showing that air is a far better insulator than hydrogen.

The simulations show that the steel shell removed loss of vacuum case heats to within 25 K of the ambient temperature (300 K) in a little more than 5 hours where the inside loss of vacuum (hydrogen filling the annulus) requires nearly double that amount of time (> 10 hours). The outside loss of vacuum (air filling the annulus) then shows about 30 hours to heat within 25 K of the ambient.

ACKNOWLEDGEMENTS

This work was carried out in collaboration with the Institute for Nuclear and Energy Technology (IKET) of the Karlsruhe Institute of Technology (KIT)

REFERENCES

- [1] J.R. Travis, P. Royle, J. Xiao, G.A. Necker, R. Redlinger, J.W. Spore, K.L. Lam, T.L. Wilson, C. Mueller and B.D. Nichols, "GASFLOW: A Computational Fluid Dynamics Code for Gases Aerosols, and Combustion", VOLUME 1, Theory and Computational Model, Karlsruher Institut für Technologie (KIT), Karlsruhe, 2011.
- [2] J.R. Travis et al., "GASFLOW: A Computational Fluid Dynamics Code for Gases, Aerosols, and Combustion", VOLUME 2, User's Manual, Karlsruher Institut für Technologie (KIT), Karlsruhe, 2011.
- [3] P. Royle, J.R. Travis and J. Kim, "GASFLOW -A Computational Fluid Dynamics Code for Gases Aerosols, and Combustion", VOLUME 3, Assessment Manual, Forschungszentrum Karlsruhe GmbH, Karlsruhe, 2008.
- [4] Dr. Kunze / Dr. Kircher, BMW Group, "CRYOSYS-SYSTEMVALIDIERUNG KRYODRUCK-FAHRZEUGTANK.", NIP-VOLLVERS AMMLUNG, BERLIN, 7./8. NOVEMBER, 2011.
- [5] H. Barthélémy, "Hydrogen storage – Industrial perspectives", *Int. J. of Hydrogen Energy*, **37**, 17364-17372, 2012.
- [6] J.R. Travis, J. Xiao, Z. Xu, D. Piccioni Koch and T. Jordan, „Real-gas Equations-of-State for the GASFLOW CFD code“, *Int. J. of Hydrogen Energy*, **38**, 8132-8140, 2013.
- [7] J.R. Travis and D. Piccioni Koch, "GASFLOW Analysis for the HySIM Hydrogen Refueling Benchmark", *Proc. 2nd International Congress on Energy Efficiency and Energy Related Materials (ENEFM2014)*, 16-19 October, 2014, Oludeniz, TURKEY.
- [8] J. Leachman, „Fundamental Equations of State for Parahydrogen, Normal Hydrogen, and Orthohydrogen“, *Masters of Science Thesis*, University of Idaho, 2007.
- [9] J.W. Leachman, R.T. Jacobsen, S.G. Penoncello and E.W. Lemmon, „Fundamental Equations of State for Parahydrogen, Normal Hydrogen, and Orthohydrogen“, *J. Phys. Chem. Ref. Data*, **38**, 721, 2009.
- [10] O. Kircher, (BMW Group), Private communication, February, 2011.
- [11] J.R. Travis, W. Breitung, D. Piccioni Koch and T. Jordan, „A Homogeneous Non-equilibrium Two-phase Critical Flow Model“, *Int. J. of Hydrogen Energy*, **37**, 17373-17379, 2012.
- [12] B. Spang, "Correlations for Convective Heat Transfer", Chemical Engineers' Resource Page. [Online]. Available: www.cheresources.com.
- [13] W.M. Kays and M.E. Crawford, M. E., "Convective Heat and Mass Transfer", McGraw-Hill, 1993.



Hydrothermal carbonization of sewage sludge on industrial scale: energy efficiency, environmental effects and combustion

工业规模污水污泥的水热碳化：能源效率，环境影响和燃烧

Matthias Stucki¹, Lea Eymann¹, Gabriel Gerner¹, Frank Hartmann¹, Rahel Wanner¹ and Rolf Krebs^{1*}

¹Institute of Natural Resource Sciences, Zurich University of Applied Sciences, Campus Grüental, CH-8820, Wädenswil, Switzerland

rolf.krebs@zhaw.ch

Accepted for publication on 29th June 2015

Abstract - In an increasing number of countries sewage sludge must be disposed of using thermal treatment. Currently, the necessary drying of the sewage sludge, after mechanical dewatering, is often accomplished using thermal methods that need large amounts of heat energy.

In this study we investigated hydrothermal carbonization (HTC) on industrial scale as an energy efficient alternative to thermal drying processes. An energy balance calculation and an assessment of the environmental effects of HTC compared to current sludge treatments were performed for a sewage treatment plant in Emmen, Switzerland. Furthermore HTC coal was burned in a sludge combustion plant, where fossil fuels could be temporarily substituted by HTC coal. Compared to the current sewage sludge drying process, it was possible to reduce the heat demand by up to 62 % and the electricity demand by up to 69 % by using HTC. A detailed life cycle assessment showed little differences of HTC compared to the thermal drying process using waste heat. However there are significant advantages of HTC compared to the thermal drying process using fossil fuels. HTC shows the most promise in terms of minimising environmental impact, provided optimization measures are applied, such as reducing phosphorus and nitrogen in the HTC process water, recycling phosphorus, using the waste heat or using renewable energy sources (e.g. sewage gas, wood chips or green electricity). Significant environmental benefits can be achieved if the HTC coal produced is used as a substitute for fossil fuels, for example in the cement industry, lignite power plants or sludge combustion plants.

Keywords – Hydrothermal carbonization, sewage sludge, energy balance, life cycle assessment, combustion.

I. INTRODUCTION

Every year, about 10 million tons of dry matter (DM) of sewage sludge is produced in the European Union, of which 37 % is recycled in agriculture [1]. However the application of sewage sludge to agricultural land is increasingly being restricted due to contamination with heavy metals, microorganisms, and a range of hazardous organic substances which can pose a threat to the soil, vegetation, animals, and humans. The thermal treatment of sewage sludge has emerged as an attractive disposal solution. Thermal treatment alternatives include mono-combustion and co-combustion in waste incineration plants and the use of dried sewage sludge matter as a surrogate fuel in cement kilns. Dewatering is a very important pretreatment step for sewage sludge before incineration. However, the established mechanical dewatering technologies for sewage sludge yield a maximum of 35% dry matter [2]. To further dry the sewage sludge by thermal methods, a large amount of energy is necessary, most of which is used to remove the moisture by evaporation [3].

The energetic benefit of mechanical expression coupled with the hydrothermal carbonization process (HTC) as compared to a conventional mechanical expression coupled with thermal drying of sewage sludge has been confirmed on laboratory scale [4]. HTC is a hydrothermal process where the solids are converted to a char-like product called HTC coal. The chemical reactions take place with the biomass fully surrounded by water. Under high temperature (180 – 220 °C)

and a pressure of approximately 20 bar, water is separated from the organic biomass by dehydration, one of the main reactions in the entire process. After carbonization, the mechanical dewaterability of non-stabilized and stabilized sludge is increased significantly. During chemical dehydration hydroxyl groups are eliminated. The calculated energy consumption for drying non-stabilized sewage sludge was lowered by up to 62 % by HTC [4].

However, no such evidence has been collected on an industrial scale and it is not clear if the laboratory scale results can be extrapolated to industrial scale plants. Moreover, comprehensive investigations of the environmental impact related to this process are still scarce. While several studies assessed the environmental impact of different sewage sludge treatment options [5-9], the authors of these studies did not include a scenario using HTC. This study therefore compares the environmental impacts of HTC with those of conventional thermal treatment options. For this purpose, an energy balance was calculated for HTC and five conventional sewage sludge disposal options were compared to three alternatives including HTC using a life cycle approach.

There is currently no combustion plant exclusively designed for HTC-coal combustion. As an alternative, co-incineration experiments were carried out at a sludge incineration plant. The goal of these experiments was to investigate if the sewage sludge combustion plant could be operated with HTC-coal without harming the plant and if HTC coal could be a substitute for fossil fuel.

II. MATERIAL AND METHODS

Carbonization of sewage sludge



Kläusli
2011

Fig.1, AVA-CO2 Industrial hydrothermal carbonization pilot plant in Karlsruhe, Germany

The stabilized sewage sludge used in this study was collected from a wastewater treatment plant near Karlsruhe (Germany) with a dry matter content of 21 % and an original pH of 7.9. The pH was stabilized at 6.5 by the addition of sulphuric and acetic acid. The carbonization of the sewage sludge was performed in a 14 m³ carbonization tank run by AVA-CO2 in Karlsruhe (Fig. 1). The process time was close to 5 hours at a median temperature of 210 °C and a pressure of 21 to 24 bar. The slurry produced was cooled to 20°C and then mechanically dewatered using a membrane filter press. A pressure of 7.5 bar was applied and HTC coal with 55% to 70% dry matter was produced. The upper heating values of

the sewage sludge and the HTC coal (precision 120 kJ/kg) were analysed before the combustion experiments.

Life Cycle Assessment

The environmental impacts of the HTC of sewage sludge were analysed using life cycle assessment (LCA), following the ISO 14040-14044 guidelines [10, 11]. LCA modelling was performed using SimaPro 7.3.3 software [12] and background data from the ecoinvent Centre [13]. The goal of the LCA was to identify the most relevant factors contributing to the life cycle environmental impacts of the HTC process and to compare the HTC process with other sewage sludge treatment processes from an environmental perspective. The modelling was based on virtual and real installations at a sewage treatment plant (STP) in Emmen, Switzerland. The functional unit of the LCA was defined as “the disposal of one annual population equivalent sewage sludge from the catchment area of the Emmen sewage treatment plant”, which is equal to a sewage amount of 27.5 kg dry matter. The alternatives analysed for the disposal of the sewage sludge are listed in Table 1. The non-HTC alternatives are based on [14].

TABLE 1, ALTERNATIVES ANALYSED FOR SEWAGE SLUDGE DISPOSAL

| | | |
|---------|----|---|
| HTC | 1A | HTC process, combustion in cement industry |
| | 1B | HTC process, combustion in lignite power plant |
| | 1C | HTC process, mono-combustion and phosphorus recovery |
| Non-HTC | 2A | Digestion, on site mono-combustion and phosphorus recovery |
| | 2B | No digestion, on site mono-combustion and phosphorus recovery |
| | 2C | Digestion, sewage sludge disposal in municipal waste incinerator |
| | 2D | Digestion, sewage sludge drying on site and combustion in cement industry |
| | 2E | Digestion, sewage sludge drying and combustion in cement industry |

Inventory data on the material and energy consumption in the HTC process as well as the composition of the process water were obtained from AVA-CO2 using a questionnaire. The

steam required for the HTC process is produced by burning sewage gas. For the non-HTC systems, the included processes are inputs and emissions from the sewage sludge pre-treatment, the digestion, the combustion of sewage gas in a combined heating and power system, the purification of sewage gas for feeding into the natural gas grid, the gas flare, the sewage dewatering, the sludge drying (with waste heat), transportation processes, as well as the disposal of the sewage sludge through combustion in a sludge incinerator, a municipal waste incinerator, or a cement plant.

TABLE 2, CREDITS FOR RENEWABLE PRODUCTS

| Renewable products | Credits in model |
|--|---|
| Heat fed into district heat grid | Heat from natural gas |
| Sewage gas fed into natural gas grid and burned in cars | Combustion of natural gas in cars |
| Application of recovered phosphorus for agriculture use | Application of conventional phosphorus fertilizer for agriculture use |
| Cement from cement plant using HTC coal | Cement from conventional cement plant |
| Electricity from burning HTC coal in lignite power plant | Electricity from conventional lignite power plant in Germany |

In addition to the above mentioned processes, the HTC alternatives include the HTC process itself and the HTC process water treatment. HTC coal could be burned in a mono-combustion plant, a cement plant or a lignite power plant. For the renewable products from the different disposal routes, environmental credits were given using an avoided-burden approach (see Table 2).

In addition, an alternative scenario was considered in which natural gas is used for both the conventional thermal sludge drying and the HTC process. The selected life cycle impact assessment (LCIA) indicators and the methods used are presented in Table 3.

TABLE 3, LIFE CYCLE IMPACT ASSESSMENT (LCIA) INDICATORS

| Criterion | Indicator | Unit | Source |
|--|---|-------------------------|-----------------|
| Conservation of non-renewable energy sources | Cumulative energy demand of non-renewable energy source | MJ-eq. | [15] |
| Conservation of non-renewable materials | Cumulative energy demand of materials and minerals | MJ-eq. | [16] |
| Climate Change | Global warming potential | kg CO ₂ -eq. | [17] |
| Eutrophication | Eutrophication potential | kg PO ₄ -eq. | [18] |
| Human toxicity | Human toxicity potential | kg 1,4-DCB-eq. | [18] |
| Eco-toxicity | Aquatic and terrestrial eco-toxicity potentials | kg 1,4-DCB-eq. | [18] |
| Highly radioactive wastes | Volume of highly radioactive wastes | cm ³ | Elementary flow |

Combustion experiments

At the sewage sludge incineration plant (SVA) in Switzerland, approximately 2.7 tons of sewage sludge (approximately 30 %DM content) is usually burnt per hour.



Fig.2, Screw conveyor for transporting sewage sludge and HTC coal into the oven of the sewage sludge incineration plant (SVA)

Approximately 150 m³ of natural gas was required per hour. On 17th September 2013, a dose of approximately 7.5kg HTC-coal per minute was added to the combustion process during three different time periods (from 12:55 to 13:02 h; from 13.15 to 14:03 h and from 15.10 to 17:02 h) (Fig. 2).

III. RESULTS

Life Cycle Assessment

The thermal energy balance of the hydrothermal carbonization of sewage sludge is compared to the conventional sludge drying process in Fig.3. The energy required by the conventional drying process to increase with a dry matter

(DM) content of the sewage sludge from 20 % to 92 % was 6.8 MJ heat and 0.26 kWh electricity per kilogram DM [14]. 92 % DM is the target value for sewage sludge in order for it to be burned in cement kilns.

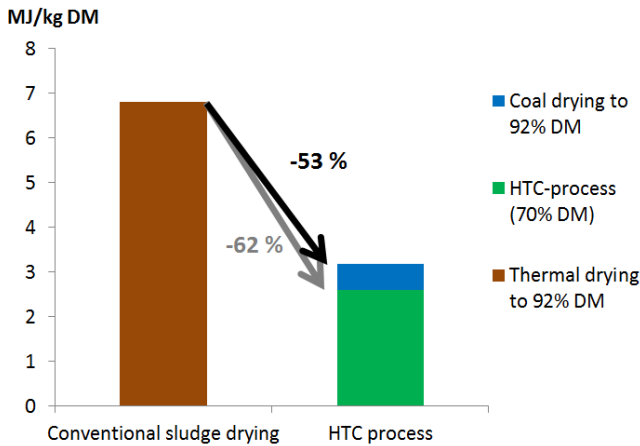


Fig.3. Comparison of the heat requirement for conventional sludge drying and hydrothermal carbonization for the drying of sewage sludge with a dry matter content of 21.3 % to a dry matter content of 92 %

The hydrothermal carbonization of sewage sludge produces HTC coal with a 70 % DM and requires 2.6 MJ heat and 0.08 kWh electricity per kilogram DM. In order to achieve a 92 % DM in the HTC coal, another 0.34 litre of water per kilogram DM must be evaporated, which requires an additional 0.6 MJ of heat and 0.02 kWh of electricity. In total, hydrothermal carbonization reduces the heat consumption for sludge drying by 53 %. Since there is sufficient waste heat from the HTC process to increase the DM content of the HTC coal from 70% DM to 92 % DM, the heat energy requirement to achieve a DM content equivalent to the conventional process is reduced by an additional 9 % (62 % in total). These results confirm the laboratory results from [4], which reports a 61 % heat energy reduction potential for HTC of sewage sludge.

Similar to the reduction of heat energy, also electric energy can be reduced by up to 69 %, if HTC is applied instead of conventional drying.

The greenhouse gas (GHG) emissions resulting from the different methods of sewage sludge disposal and the GHG credits for the replacement of fossil fuels are presented in Fig. 4. The results show that the carbonization process (in black) makes only a small contribution to the overall global warming potential of the different disposal routes. In those cases where dried sewage sludge or HTC coal can be substituted for fossil fuels in cement kilns or power plants, the environmental credits outweigh the GHG emissions from the sewage sludge processing and disposal.

An overview of the life cycle impact assessment results for all impact indicators and sewage disposal routes is presented in Table 4. In several cases, the environmental credits exceed the environmental burdens.

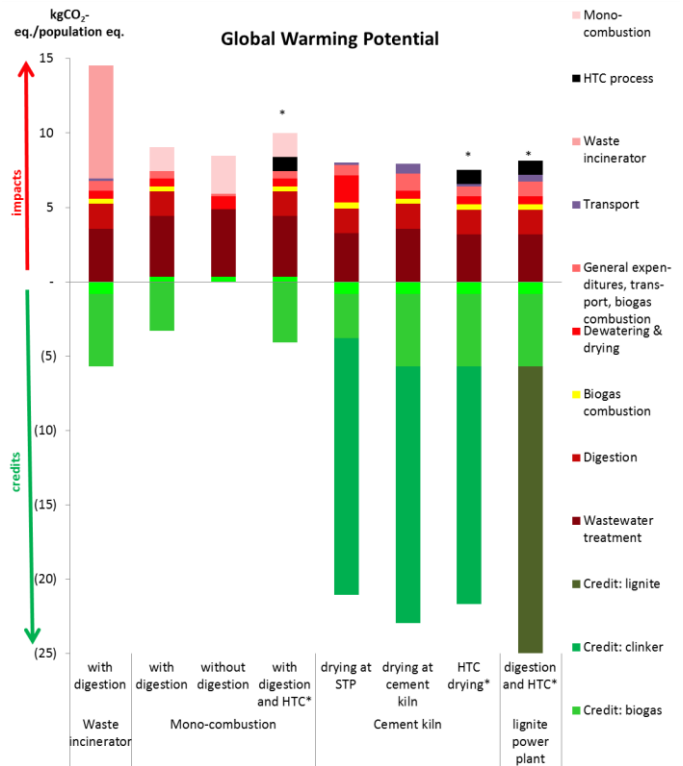


Fig.4. Comparison of greenhouse gas emissions of different ways of sewage sludge disposal. Environmental burdens (red colours) are juxtaposed with environmental credits (green colours). Alternatives with a HTC process are marked with a “*”.

Since the heat requirements for most processes are considered to be met by waste heat from burning dried sewage sludge, the main contribution to the non-renewable energy indicator comes from the share of nuclear power in the electricity used in the sewage treatment plant. The same share of nuclear power also determines the results for the radioactive waste indicator.

The mineral indicator value is heavily influenced by the precipitating agent used in the STP. High credits are awarded when phosphorus is recovered from the sewage and used as a substitute for conventional phosphorus fertilizer.

Eutrophication also receives high credit for phosphorus recovery due to the reduction in phosphorus emissions from conventional phosphorus production. For this indicator the alternatives with HTC show higher impacts than disposal routes without HTC because HTC process water has increased nitrate and ammonia concentrations.

The results for the different toxicity indicators are highly influenced by the dioxin and heavy metal emissions from the waste incinerators and the heavy metal input to the environment from using the recovered phosphorus in agriculture.

As shown in Fig. 4, there are only minor differences between the environmental impact of HTC and of conventional sludge disposal using recycled waste heat for the thermal drying step. However, if treatment plants use fossil fuels for thermal drying, HTC has significant environmental benefits (Fig.5).

TABLE 4, LCIA RESULTS (ENVIRONMENTAL IMPACT VERSUS ENVIRONMENTAL CREDITS) PER POPULATION EQUIVALENT

| | | Waste incinerator | | Mono-combustion | | Cement kiln | | | Lignite power plant |
|---|---------|-------------------|----------------|-------------------|-------------------------|---------------|-----------------------|-------------|---------------------|
| | | with digestion | with digestion | without digestion | with digestion and HTC* | drying at STP | drying at cement kiln | HTC drying* | digestion and HTC* |
| Global warming potential (kg CO ₂ eq) | Impact | 14.0 | 9.5 | 9.3 | 10.5 | 7.4 | 6.9 | 7.0 | 7.3 |
| | Credits | -5.7 | -4.1 | -0.8 | -4.9 | -21 | -23 | -22 | -25 |
| Non-renewable energy (MJ) | Impact | 247 | 298 | 354 | 326 | 248 | 197 | 190 | 195 |
| | Credits | -116 | -83 | -14 | -99 | -221 | -261 | -251 | -321 |
| Minerals (exergy) (MJ) | Impact | 2.0 | 0.7 | 0.7 | 0.7 | 0.8 | 0.6 | 0.6 | 0.6 |
| | Credits | -0.0 | -3.6 | -3.6 | -3.6 | -2.5 | -2.5 | -2.3 | -0.0 |
| Eutrophication (g PO ₄ ³⁻ eq) | Impact | 14.2 | 4.0 | 4.3 | 10.5 | 3.2 | 3.3 | 9.0 | 9.2 |
| | Credits | -0.7 | -51 | -51 | -51 | -3.0 | -3.2 | -3.1 | -16 |
| Human toxicity (kg 1,4-DB eq) | Impact | 7.8 | 2.8 | 3.0 | 3.2 | 1.5 | 0.7 | 1.0 | 1.0 |
| | Credits | -0.2 | -0.1 | -0.1 | -0.1 | -0.5 | -0.6 | -0.5 | -0.2 |
| Aquatic ecotoxicity (kg 1,4-DB eq) | Impact | 0.29 | 2.77 | 2.78 | 2.77 | 0.05 | 0.04 | 0.04 | 0.04 |
| | Credits | - | - | - | - | - | - | - | - |
| Terrestrial ecotoxicity (kg 1,4-DB eq) | Impact | 0.07 | 0.30 | 0.30 | 0.30 | 0.15 | 0.14 | 0.13 | 0.06 |
| | Credits | - | - | - | - | - | - | - | - |
| Highly radioactive wastes (cm ³) | Impact | 104 | 161 | 187 | 174 | 136 | 99 | 94 | 95 |
| | Credits | -2.4 | -1.7 | -0.1 | -2.0 | -4.6 | -5.5 | -5.2 | -4.0 |

observed after adding the HTC coal to the combustion process. Such effects would have been expressed by a massive increase in the oven quoin temperature to a critical value of approximately 920°C (red chart in fig. 6).

TABLE 5, CALORIFIC VALUES (INCLUDING DRY MATTER) OF THE MATERIALS USED FOR THE COMBUSTION EXPERIMENT

| | Calorific value in MJ/kg (kWh/kg) at 85% DM for HTC-coal and 30% DM for sewage sludge | Calorific value in MJ/kg DM (kWh/kg DM) |
|---------------|---|---|
| HTC-coal | 12.5 (3.5) | 14.7 (4.1) |
| Sewage Sludge | 3.3 (0.9) | 11 (3.1) |

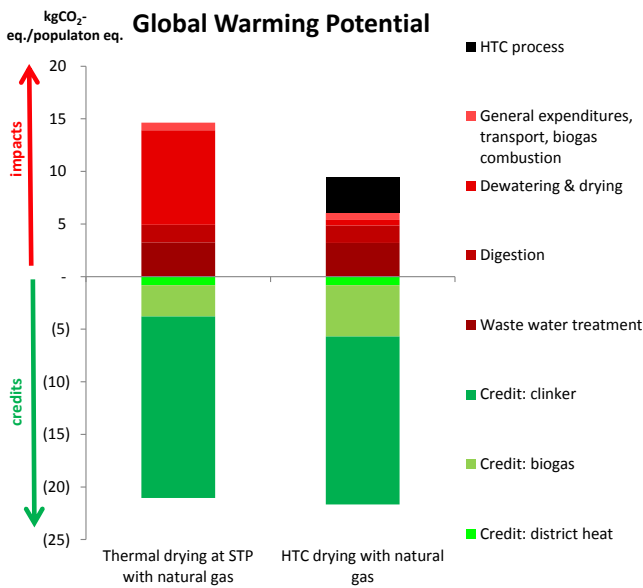


Fig.5, Global warming potential of sewage sludge disposal in a cement plant if the thermal drying and the HTC processes are fueled by natural gas. Environmental impacts (red colors) are juxtaposed with environmental credits (green colors).

Combustion experiments

The calorific value and the dry matter of the burned HTC-coal were significantly higher than the sewage sludge (Table 5). No negative effects on the sewage sludge incineration plant were

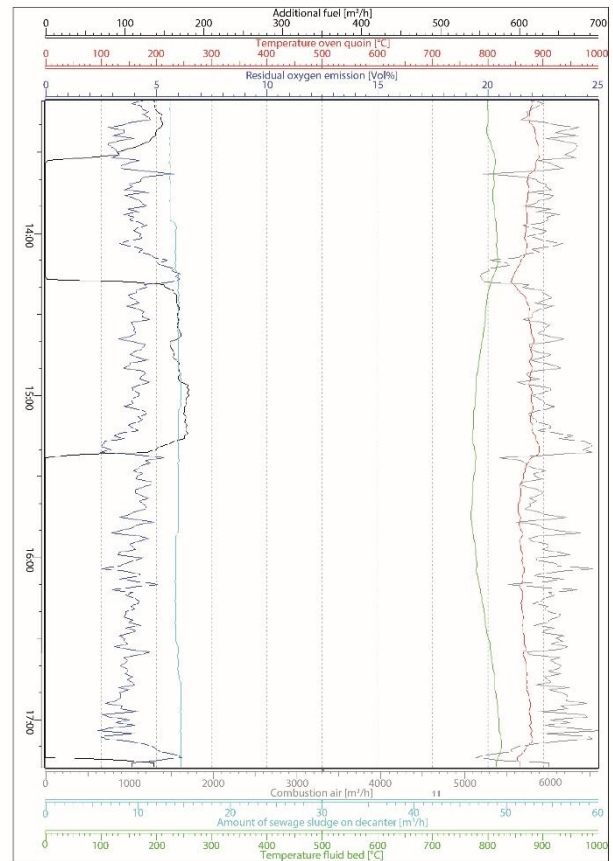


Fig.6, Change in different parameters during HTC coal addition to the sewage sludge combustion plant in Winterthur (17.10.2013); black: fossil fuel in m³/h; red: oven quoin temperature, in °C; blue: residual oxygen emission in Vol%; grey: combustion air in m³/h; blue-green: amount of sewage sludge on decanter in m³/h; green: fluid bed temperature in °C. Approximately 7.5kg HTC-coal was added per minute to the combustion process from 12:55 to 13:02 h; from 13.15 to 14:03 h and from 15.10 to 17:02 h.

In this experiment the regular biogas was turned off entirely for a total of almost 2 hours during all three periods of HTC coal addition to the combustion process (black chart in figure 6) This is equivalent to an approximate saving of 300m³ of biogas.

IV. CONCLUSION

Hydrothermal carbonization of sewage sludge reduced the energy requirement compared to conventional drying of sewage sludge by up to 62 %. These results correspond very well to results from laboratory experiments [4]. Under the following conditions, the hydrothermal carbonization of sewage sludge is particularly environmentally favourable:

- Waste heat, if available, or other local renewable energy sources, such as sewage gas, are used in the HTC process.
- Green electricity is used for HTC process, e.g. generated with sewage gas.
- Further reduction of the nitrogen and phosphorus freight in the process water.
- Phosphorous is recovered and recycled.
- HTC coal is used as a substitute for fossil fuels (e.g. in cement kiln or power plant).
- The HTC process is implemented in situations where the carbonization process can replace conventional sewage sludge drying with fossil fuels.

The use of HTC coal as a substitute for fossil fuels and the associated reduction in GHG emissions were also analysed by [19]. They identified a large potential for mitigating greenhouse gas emissions by substituting heating oil in auxiliary sewage sludge incineration firings with HTC coal. These findings support the results of the present study.

Under certain conditions, the HTC process can bring significant environmental advantages compared to conventional thermal sewage sludge drying. This paper shows that substituting fossil fuels in lignite power plants and cement kilns with HTC coal is particularly environmentally favourable.

Burning HTC coal in sewage sludge combustion plants is feasible and can it can be used as a substitute for natural gas for at least limited periods of time. In such plants, downstream phosphorous recovery from the combustion residues is also possible.

ACKNOWLEDGEMENTS

This research was funded by the Swiss Federal Office for the Environment. The authors gratefully appreciate the help and support of AVA-CO₂, which is responsible for the operation of the industrial HTC pilot plant in Karlsruhe (D). Furthermore, we thank Sybille Büsler Knöpfel from treeze Ltd. who kindly provided us with the life cycle inventories published in [14] and very kindly supported the present study.

REFERENCES

- [1] Milieu Ltd, WRc, RPA. Environmental, economic and social impacts of the use of sewage sludge on land. final report. Part III: Project interim reports. European Commission; 2010. Report No.: DG ENV.G.4/ETU/2008/0076.
- [2] Raynauda M, Vaxelairea J, Oliviera J, Dieudé-Fauvelb E, Baudezb J. Compression dewatering of municipal activated sludge: Effects of salt and pH. *Water Research*. 2012;46(14):4448-56.
- [3] Fytilli D, Zabaniotou A. Utilization of sewage sludge in EU application of old and new methods - A review. *Renewable and Sustainable Energy Reviews*. 2008;12(1):116-40.
- [4] Escala M, Zumbühl T, Koller C, Junge R, Krebs R. Hydrothermal carbonization as an energy-efficient alternative to established drying technologies for sewage sludge: A feasibility study on a laboratory scale. *Energy Fuels*. 2013 01/17; 2013/03;27(1):454-60.
- [5] Hong J, Hong J, Otaki M, Jolliet O. Environmental and economic life cycle assessment for sewage sludge treatment processes in japan. *Waste Management*. 2009;29:696-703.
- [6] Bridle T, Skrypski-Mantele S. Assessment of sludge reuse options: A life-cycle approach. *Water Science and Technology*. 2000;41(8):131-5.
- [7] Houillon G, Jolliet O. Life cycle assessment of processes for the treatment of wastewater
urban sludge: Energy and global warming analysis. *Journal of Cleaner Production*. 2005;13:287-99.
- [8] Lederer J, Rechberger H. Comparative goal-oriented assessment of conventional and alternative sewage sludge treatment options. *Waste Management*. 2010;30:1043-56.
- [9] Suh Y, Rousseaux P. An LCA of alternative wastewater sludge treatment scenarios. *Resources, Conservation and Recycling*. 2002;35:191-200.
- [10] International Organization for Standardization (ISO). Environmental management - life cycle assessment - principles and framework. Geneva: 2006. Report No.: ISO 14040:2006; Second Edition 2006-06.
- [11] International Organization for Standardization (ISO). Environmental management - life cycle assessment - requirements and guidelines. Geneva: 2006. Report No.: ISO 14044:2006; First edition 2006-07-01.
- [12] PRé Consultants. SimaPro 7.3.3. 2012;7.3.3, ecoinvent data v2.2.
- [13] ecoinvent Centre. Ecoinvent data v2.2, ecoinvent reports no. 1-25. swiss centre for life cycle inventories. .2010.
- [14] Bättig M, Klingler G, Büsler S, Frischknecht R, Schulthess Rv, Küttel P. Vergleich verschiedener entsorgungswege des klärschlammes aus der region luzern mittels multikriterienanalyse und ökobilanzen. Zürich, Uster, Luzern, Schweiz: Bundesamt für Umwelt (BAFU), Kanton Luzern, Dienststelle Umwelt und Energie (uwe), Recycling Entsorgung Abwasser Luzern (REAL); 2011.

[15] Hischer R, Weidema B, Althaus H, Bauer C, Frischknecht R, Doka G, et al. Implementation of life cycle impact assessment methods. CD-ROM. Dübendorf, CH: Swiss Centre for Life Cycle Inventories; 2010. Report No.: ecoinvent report No. 3, v2.2.

[16] Boesch ME, Hellweg S, Huijbregts MAJ, Frischknecht R. Applying cumulative exergy demand (CExD) indicators to the ecoinvent database. *Int J LCA*. 2007;12(3):181-90.

[17] IPCC. The IPCC fourth assessment report. Cambridge: Cambridge University Press.; 2007.

[18] Guinée JB,(final editor), Gorrée M, Heijungs R, Huppes G, Kleijn R, de Koning A, et al. Life cycle assessment; an operational guide to the ISO standards; part 3: Scientific background. Den Haag and Leiden, The Netherlands: Ministry of Housing, Spatial Planning and Environment (VROM) and Centre of Environmental Science (CML); 2001.

[19] Vogt R, Fehrenbach H. Maßnahmenplan zur Umsetzung einer vorbildhaften klimafreundlichen abfallentsorgung im land berlin. Heidelberg, Deutschland: Senatsverwaltung für Stadtentwicklung und Umwelt; 2012.



Identification of lithium-ion physics-based model parameter values

锂离子基于物理的模型参数值辨识

Ryan Jobman, M. Scott Trimboli, and Gregory L. Plett*

Department of Electrical and Computer Engineering, University of Colorado Colorado Springs, Colorado Springs, CO 80918, USA

gplett@uccs.edu

Accepted for publication on 10 January 2015

Abstract - Physics-based lithium-ion cell models are a promising alternative to equivalent-circuit models for future battery management systems. However, they also have many more parameter values that must be measured or inferred to make the model match the behaviors of a real cell. This “system identification” problem is significant, and in the past has relied on cell teardown and complex and costly electrochemical experiments to determine the required parameter values.

In this paper, we propose a methodology that minimizes the need for cell teardown and any accompanying electrochemical experimentation. Instead, the model equations are reformulated, and specific cell-level laboratory tests are crafted such that the current–voltage response isolates certain sets of parameter values in the model. These tests are executed on standard cell cycling equipment. Simple and fast optimization procedures then compute the parameter values directly from the specialized lab-test data.

We present results based on a virtual (simulated) cell, where “truth” values for the electrochemical parameters are known for comparison purposes. In most cases, the identified parameters have relative identification error less than 1%.

Keywords - physics-based model; lithium-ion model; measuring lithium-ion model parameters; system identification

I. INTRODUCTION

Battery management systems require cell models to estimate state of charge, state of health, available energy and power. Presently, due to their computational simplicity and robustness, equivalent-circuit models (ECMs) are very widely used [1]. These models execute quickly and have relatively few parameter values to optimize to make the model calculations fit laboratory current–voltage cell-test data. However, ECMs lack the predictive capability of physics-based models (PBMs). For example, while

equivalent-circuit models can predict a cell’s current–voltage behaviors well, they cannot predict internal cell electrochemical variables such as lithium concentrations or electric potentials at different spatial locations internal to the cell. Knowledge of these internal variables is critical to being able to predict and control the instigators of premature aging or unsafe operating conditions.

Physics-based models [2] present possible opportunities to control cells to slow aging [3–4]. But, they come with a cost. One challenge when using PBMs is their computational complexity, but reduced-order models (ROMs) overcome this concern [5–8]. Another challenge is that PBMs also have many more parameter values that must be measured or inferred to make the model equations match the behaviors of a real lithium-ion cell. This “system identification” problem is significant, and in the past has been done either:

1) By the cell builders, who know the materials and related values because they chose them in their design, or

2) By cell teardown and electrochemical and physical tests designed to measure specific parameter values. This option is costly and requires operators having a high level of training. Further, measured parameter values sometimes differ significantly depending on the measurement techniques used and it is not necessarily possible to measure all needed parameter values, so some must be fit by optimizing model predictions to current–voltage data collected from the cell.

More recently, Forman et al. reported work done to use cell current–voltage data to identify these parameter values [9]. In their work, they found that they could identify many but not all parameters of a PBM. This paper presented an important advance in the field—it showed that (at least many of the) parameters can be identified from current–voltage data—but

the method was not very practical since it took a supercomputing cluster 3 weeks to solve the optimizations.

In this paper, we propose a new approach to PBM parameter identification that significantly reduces the number of electrochemical tests that must be performed. If electrode materials are unknown, a cell teardown is still needed to find electrode open-circuit potential (OCP) relationships. Otherwise, no teardown is necessary and simple cell-level laboratory tests are run to isolate groups of parameters in the model to identify their values. Once data are collected, the required CPU time for optimization is several minutes on a desktop computer versus weeks on a supercomputer. This, combined with a suitable ROM, makes PBMs accessible for practical BMS.

We proceed by first reformulating the PBM in terms of new dimensionless grouped parameters. The original set of parameters is not completely observable from the current–voltage data, but the grouped parameters are. This set of grouped parameters is sufficient to be able to simulate all cell electrochemical variables, so the simplified model does not lose generality. The reformulation also removes the need to identify 11 parameter values, which significantly simplifies the system-identification problem. If the full original set of parameters is needed for some reason, a cell teardown can supply the missing dimensions relatively easily.

Next, we will describe cell tests to determine the cell static OCP relationships. Then, we present a way to use pulse tests to identify the majority of the PBM parameters. Finally, we show how to use electrochemical impedance spectroscopy (EIS) to find the remaining values.

We present results based on a virtual (simulated) cell, where “truth” values for the electrochemical parameters are known for comparison purposes. The virtual cell’s coupled PDE model is simulated using COMSOL and the same set of experiments that would be executed in a laboratory. The current–voltage data from the simulation are used to identify the cell’s parameter values: these identified values are compared to the known “truth” values. In most cases, the identified parameters have relative error less than 1%.

II. REFORMULATING THE PDE MODEL

2.1. ORIGINAL PDE MODEL

We assume a standard Doyle–Fuller–Newman pseudo-2d model of a lithium-ion battery cell. This model is derived in detail in [8] and is reviewed here. It comprises four partial-differential equations (PDEs) describing electrical potential and concentrations of lithium in both the solid and electrolyte, plus one algebraic equation describing lithium flux density from solid to electrolyte. The PDEs have boundary conditions at the cell edges and/or junctions between cell regions. In the following, 1d spatial location $x = 0$ is the location of the negative-electrode current collector, $x = L^{\text{neg}}$ is the negative-electrode/separator boundary, $x = L^{\text{neg}} + L^{\text{sep}}$ is the separator/positive-electrode boundary, and $x = L^{\text{tot}} = L^{\text{neg}} + L^{\text{sep}} + L^{\text{pos}}$ is the location of the positive-electrode current collector.

1d radial location $r = 0$ is at a particle center and $r = R_s$ is at the surface of a particle.

Potential in the solid active materials at any point in the negative and positive electrodes $\phi_s(x,t)$ in V is defined by the following PDE and associated boundary conditions:

$$\begin{aligned} \frac{\partial}{\partial x} \sigma_{\text{eff}} \frac{\partial}{\partial x} \phi_s - a_s F j &= 0 \\ \frac{\partial}{\partial x} \phi_s \Big|_{x=L^{\text{neg}}} &= \frac{\partial}{\partial x} \phi_s \Big|_{x=L^{\text{neg}}+L^{\text{sep}}} = 0 \\ \frac{\partial}{\partial x} \phi_s \Big|_{x=0} &= \frac{\partial}{\partial x} \phi_s \Big|_{x=L^{\text{tot}}} = -\frac{i_{\text{app}}}{A \sigma_{\text{eff}}}. \end{aligned}$$

In these equations, σ_{eff} is the effective electronic conductivity of the solid matrix in S m^{-1} and a_s is the specific interfacial surface area of the solid particles in $\text{m}^2 \text{m}^{-3}$ (equivalently, in m^{-1}).

Potential in the electrolyte $\phi_e(x,t)$ in V at any point in the cell is defined by the following PDE and associated boundary conditions:

$$\begin{aligned} \frac{\partial}{\partial x} \left(\kappa_{\text{eff}} \frac{\partial}{\partial x} \phi_e + \kappa_{D,\text{eff}} \frac{\partial}{\partial x} \ln c_e \right) + a_s F j &= 0 \\ \kappa_{\text{eff}} \frac{\partial}{\partial x} \phi_e + \kappa_{D,\text{eff}} \frac{\partial}{\partial x} \ln c_e \Big|_{x=0} &= 0 \\ \kappa_{\text{eff}} \frac{\partial}{\partial x} \phi_e + \kappa_{D,\text{eff}} \frac{\partial}{\partial x} \ln c_e \Big|_{x=L^{\text{tot}}} &= 0. \end{aligned}$$

Here, κ_{eff} is the effective ionic conductivity of the electrolyte in the porous media in S m^{-1} , and t_+^0 is the unitless transference number of the lithium ions with respect to the solvent in the electrolyte. These equations use the shorthand

$$\kappa_{D,\text{eff}} = \frac{2RT(t_+^0 - 1)}{F} \kappa_{\text{eff}},$$

so $\kappa_{D,\text{eff}}$ is not really a free parameter once all other parameters are known.

Lithium concentration in the solid active materials $c_s(x,r,t)$ in mol m^{-3} at any point in the negative and positive electrodes is defined by the following PDE and associated boundary conditions:

$$\begin{aligned} \frac{\partial c_s}{\partial t} &= \frac{1}{r^2} \frac{\partial}{\partial r} \left(D_s r^2 \frac{\partial c_s}{\partial r} \right) \\ D_s \frac{\partial c_s}{\partial r} \Big|_{r=R_s} &= -j \quad \text{and} \quad D_s \frac{\partial c_s}{\partial r} \Big|_{r=0} = 0. \end{aligned}$$

Here, D_s is the diffusivity of lithium in the solid in $\text{m}^2 \text{s}^{-1}$.

Lithium concentration in the electrolyte $c_e(x,t)$ in mol m^{-3} at any point in the cell is defined by the following PDE and associated boundary conditions:

$$\begin{aligned} \frac{\partial(\varepsilon_e c_e)}{\partial t} &= \frac{\partial}{\partial x} D_{e,\text{eff}} \frac{\partial}{\partial x} c_e + a_s (1 - t_+^0) j \\ \frac{\partial c_e}{\partial x} \Big|_{x=0} &= 0 \quad \text{and} \quad \frac{\partial c_e}{\partial x} \Big|_{x=L^{\text{tot}}} = 0. \end{aligned}$$

Here, $D_{e,\text{eff}}$ is the effective diffusivity of the lithium ion in the electrolyte in the porous media, in $\text{m}^2 \text{s}^{-1}$, and ε_e is the unitless volume fraction of the electrolyte in the porous media (also known as the porosity of the media).

Finally, lithium flux density from the solid active materials $j(x,t)$ in $\text{mol m}^{-2} \text{s}^{-1}$ to the electrolyte at any point in the negative and positive electrodes is defined by the following algebraic equation:

$$j = k_0(c_e)^{1-\alpha}(c_{s,\text{max}} - c_{s,e})^{1-\alpha}(c_{s,e})^\alpha \times \left\{ \exp\left(\frac{(1-\alpha)F}{RT}\eta\right) - \exp\left(\frac{-\alpha F}{RT}\eta\right) \right\}$$

$$\eta = \phi_s - \phi_e - U_{\text{ocp}}(c_{s,e}) - FR_{\text{film}}j.$$

In these equations, k_0 is a reaction-rate constant, $c_{s,e}$ is the concentration of lithium at the particle surface, $c_{s,\text{max}}$ is the concentration of lithium in the solid when all lithium sites are occupied, R_{film} is the resistivity of a surface film in Ωm^2 and U_{ocp} is the open-circuit-potential function of the active materials, in V.

Initial concentration of lithium in the electrolyte is denoted by $c_{e,0}$. Initial concentration of lithium in the solid active materials is determined from cell state of charge z via

$$c_{s,0} = c_{s,\text{max}}(\theta_0 + z(\theta_{100} - \theta_0)).$$

Here, θ_0 is the unitless electrode stoichiometry when the cell is at 0% state of charge and θ_{100} is the stoichiometry when the cell is at 100% state of charge.

Table I lists the complete set of parameters that are required if one wishes to simulate the PDE model. (The ordering of parameters in the table is the same order with which they were introduced in this section.) Further, one also needs to know the open-circuit potential (OCP) functions for the two electrode active materials. A total of 35 values must be identified, plus the two OCP functions.

2.2. REFORMULATED PDE MODEL

A close examination of the PDE model reveals that a number of the PBM parameters never appear in isolation but always appear in groups. For example, κ_{eff} is always multiplied by current-collector plate area A and divided by cell-region length L in every equation in which it appears. Therefore, we can make a lumped parameter κ_{tot} that combines these three values into a single parameter. When we do this for all such groups of parameters, neither A nor L appear by themselves in any of the remaining equations. This means that they, as well as several other individual parameters, are not uniquely observable from current–voltage data. So we must reformulate the PDE model in terms of grouped parameters that can be observed from current–voltage data. When we do so, we find that the resulting grouped parameters are dimensionless.

We begin by defining a dimensionless spatial variable \bar{x} such that $0 \leq \bar{x} \leq 1$ in the negative electrode, $1 \leq \bar{x} \leq 2$ in the separator, and $2 \leq \bar{x} \leq 3$ in the positive electrode:

TABLE I, LIST OF PARAMETERS FOR ORIGINAL PDE MODEL

| Negative electrode | Separator | Positive electrode |
|------------------------------------|------------------------------------|------------------------------------|
| $\sigma_{\text{eff}}^{\text{neg}}$ | | $\sigma_{\text{eff}}^{\text{pos}}$ |
| a_s^{neg} | | a_s^{pos} |
| L^{neg} | L^{sep} | L^{pos} |
| A | | |
| $\kappa_{\text{eff}}^{\text{neg}}$ | $\kappa_{\text{eff}}^{\text{sep}}$ | $\kappa_{\text{eff}}^{\text{pos}}$ |
| D_s^{neg} | | D_s^{pos} |
| R_s^{neg} | | R_s^{pos} |
| $\varepsilon_e^{\text{neg}}$ | $\varepsilon_e^{\text{sep}}$ | $\varepsilon_e^{\text{pos}}$ |
| $D_{e,\text{eff}}^{\text{neg}}$ | $D_{e,\text{eff}}^{\text{sep}}$ | $D_{e,\text{eff}}^{\text{pos}}$ |
| t_+^0 | | |
| k_0^{neg} | | k_0^{pos} |
| $c_{s,\text{max}}^{\text{neg}}$ | | $c_{s,\text{max}}^{\text{pos}}$ |
| α^{neg} | | α^{pos} |
| $R_{\text{film}}^{\text{neg}}$ | | $R_{\text{film}}^{\text{pos}}$ |
| $c_{e,0}$ | | |
| θ_0^{neg} | | θ_0^{pos} |
| $\theta_{100}^{\text{neg}}$ | | $\theta_{100}^{\text{pos}}$ |

$$\bar{x} = \begin{cases} x/L^{\text{neg}} & 0 \leq x \leq L^{\text{neg}} \\ \frac{x-L^{\text{neg}}}{L^{\text{sep}}} & L^{\text{neg}} \leq x \leq L^{\text{neg}} + L^{\text{sep}} \\ \frac{x-L^{\text{neg}}-L^{\text{sep}}}{L^{\text{pos}}} & L^{\text{neg}} + L^{\text{sep}} \leq x \leq L^{\text{pos}}. \end{cases}$$

Similarly, we define a dimensionless radial variable $\bar{r} = r/R_s$ such that $0 \leq \bar{r} \leq 1$.

Next, we define “total” grouped parameters:

$$\sigma_{\text{tot}} = \frac{\sigma_{\text{eff}}A}{L}, \quad \kappa_{\text{tot}} = \frac{\kappa_{\text{eff}}A}{L}, \quad \kappa_{D,\text{tot}} = \frac{\kappa_{D,\text{eff}}A}{L},$$

$$D_{s,\text{tot}} = \frac{D_s}{R_s^2}, \quad D_{e,\text{mod}} = \frac{D_{e,\text{eff}}Ac_{e,0}}{L(1-t_+^0)^2}, \quad R_{\text{film,tot}} = \frac{R_{\text{film}}}{a_sAL},$$

$$k_{\text{step}} = \frac{a_s k_0 \sqrt{c_{e,0}}}{\varepsilon_s}, \quad L_{e,\text{mod}} = \frac{\varepsilon_e AL c_{e,0}}{(1-t_+^0)^2}.$$

We also define new electrochemical variables:

$$j_{\text{tot}} = a_s AL j,$$

$$n_s = a_s AL R_s c_s / 3,$$

$$c_{e,\text{ratio}} = c_e / c_{e,0}.$$

These new parameter and electrochemical-variable definitions allow us to reformulate the PDE model.

Electrical potential in the solid active materials at any point in the negative and positive electrodes is now defined by the following PDE and associated boundary conditions:

$$\sigma_{\text{tot}} \frac{\partial^2}{\partial \bar{x}^2} \phi_s - F j_{\text{tot}} = 0$$

$$\left. \frac{\partial}{\partial \bar{x}} \phi_s \right|_{\bar{x}=1} = \left. \frac{\partial}{\partial \bar{x}} \phi_s \right|_{\bar{x}=2} = 0$$

$$\left. \frac{\partial}{\partial \bar{x}} \phi_s \right|_{x=0} = \left. \frac{\partial}{\partial \bar{x}} \phi_s \right|_{\bar{x}=3} = -\frac{i_{\text{app}}}{\sigma_{\text{tot}}}.$$

TABLE II, LIST OF PARAMETERS FOR REFORMULATED PDE MODEL

| Negative electrode | Separator | Positive electrode |
|------------------------------------|------------------------------------|------------------------------------|
| $\sigma_{\text{tot}}^{\text{neg}}$ | | $\sigma_{\text{tot}}^{\text{pos}}$ |
| $\kappa_{\text{tot}}^{\text{neg}}$ | $\kappa_{\text{tot}}^{\text{sep}}$ | $\kappa_{\text{tot}}^{\text{pos}}$ |
| $D_{s,\text{tot}}^{\text{neg}}$ | | $D_{s,\text{tot}}^{\text{pos}}$ |
| V_e^{neg} | V_e^{sep} | V_e^{pos} |
| $D_{e,\text{tot}}^{\text{neg}}$ | $D_{e,\text{tot}}^{\text{sep}}$ | $D_{e,\text{tot}}^{\text{pos}}$ |
| t_+^0 | | |
| $k_{\text{step}}^{\text{neg}}$ | | $k_{\text{step}}^{\text{pos}}$ |
| $n_{s,\text{max}}^{\text{neg}}$ | | $n_{s,\text{max}}^{\text{pos}}$ |
| $R_{\text{film,tot}}^{\text{neg}}$ | | $R_{\text{film,tot}}^{\text{pos}}$ |
| θ_0^{neg} | | θ_0^{pos} |
| $\theta_{100}^{\text{neg}}$ | | $\theta_{100}^{\text{pos}}$ |

Electrical potential in the electrolyte at any point in the cell is now defined by the following PDE and associated boundary conditions:

$$\begin{aligned} \kappa_{\text{tot}} \frac{\partial^2}{\partial \bar{x}^2} \phi_e + \kappa_{D,\text{tot}} \frac{\partial^2}{\partial \bar{x}^2} \ln c_{e,\text{ratio}} + F j_{\text{tot}} &= 0 \\ \kappa_{\text{tot}} \frac{\partial}{\partial \bar{x}} \phi_e + \kappa_{D,\text{tot}} \frac{\partial}{\partial \bar{x}} \ln c_{e,\text{ratio}} \Big|_{\bar{x}=0} &= 0 \\ \kappa_{\text{tot}} \frac{\partial}{\partial \bar{x}} \phi_e + \kappa_{D,\text{tot}} \frac{\partial}{\partial \bar{x}} \ln c_{e,\text{ratio}} \Big|_{\bar{x}=3} &= 0. \end{aligned}$$

Normalized lithium concentration in the solid active materials at any point in the negative and positive electrodes is now defined by the following PDE and associated boundary conditions:

$$\begin{aligned} \frac{\partial n_s}{\partial t} &= \frac{1}{\bar{r}^2} \frac{\partial}{\partial \bar{r}} \left(D_{s,\text{tot}} \bar{r}^2 \frac{\partial n_s}{\partial \bar{r}} \right) \\ D_{s,\text{tot}} \frac{\partial n_s}{\partial \bar{r}} \Big|_{\bar{r}=1} &= -j_{\text{tot}} \\ D_{s,\text{tot}} \frac{\partial n_s}{\partial \bar{r}} \Big|_{\bar{r}=0} &= 0. \end{aligned}$$

Normalized lithium concentration in the electrolyte at any point in the cell is now defined by the following PDE and associated boundary conditions:

$$\begin{aligned} L_{e,\text{mod}} \frac{\partial c_{e,\text{ratio}}}{\partial t} &= \frac{\partial}{\partial \bar{x}} D_{e,\text{mod}} \frac{\partial}{\partial \bar{x}} c_{e,\text{ratio}} + \frac{1}{1-t_+^0} j_{\text{tot}} \\ \frac{\partial c_{e,\text{ratio}}}{\partial \bar{x}} \Big|_{\bar{x}=0} &= 0 \\ \frac{\partial c_{e,\text{ratio}}}{\partial \bar{x}} \Big|_{\bar{x}=3} &= 0. \end{aligned}$$

Finally, lithium flux density from the solid active materials to the electrolyte at any point in either electrode is now defined by the following algebraic equation:

$$\begin{aligned} j_{\text{tot}} &= 2j_{0,\text{tot}} \sinh \left(\frac{F}{2RT} \eta \right) \\ j_{0,\text{tot}} &= k_{\text{step}} \sqrt{c_{e,\text{ratio}}} \sqrt{n_{s,\text{max}} - n_{s,e}} \sqrt{n_{s,e}} \\ \eta &= \phi_s - \phi_e - U_{\text{ocp}}(n_{s,e}) - FR_{\text{film,tot}} j_{\text{tot}}. \end{aligned}$$

In this equation, we have assumed that $\alpha = 0.5$, which is common in the literature.

Initial normalized concentration of lithium in the electrolyte is denoted by $c_{e,\text{ratio}} = 1$. Initial normalized concentration of lithium in either electrode's solid active materials is determined from cell state of charge z via

$$n_{s,0} = n_{s,\text{max}} (\theta_0 + z(\theta_{100} - \theta_0)).$$

Table II lists the complete set of parameters that is required if one wishes to simulate the reformulated PDE model. (The ordering of parameters in the table is the same as in Table I, except that the reformulation removes some parameters from the model.) We also still need to know the OCP functions for the two electrode active materials. A total of 24 values must be identified, plus the two OCP functions. The reformulation has removed the requirement for finding 11 parameter values—a greater than 25% reduction.

With this reformulated model, we are still able to simulate the potential in the solid and electrolyte and the concentration of lithium in the electrolyte exactly; further, we are able to simulate the concentration of lithium in the solid as well as the lithium flux density to within scaling factors. If we are required to simulate these latter two quantities exactly, then we still require a cell teardown to measure a_s , A , L , and R_s . These geometric properties are relatively easy to measure using SEM imaging. However, we often don't need the exact values of these variables: knowing them to within a scaling factor is sufficient when computing power limits based on lithium depletion, for example.

III. OPEN-CIRCUIT VOLTAGE TESTS

We identify the model parameter values and functions using specialized laboratory tests that isolate groups of parameters. Equilibrium (thermodynamic) properties are found using pseudo-static open-circuit voltage tests; instantaneous (resistive) properties are found using pulse tests; and intermediate-frequency properties are found using electrochemical impedance spectroscopy (EIS) tests. These tests, and the parameters that are identified by them, are discussed in the following sections.

3.1. WHEN THE ELECTRODE CHEMISTRIES ARE KNOWN

The open-circuit potential relationships $U_{\text{ocp}}(n_s)$ for both electrodes are needed in order to compute the overpotential η in the model equations. Further, we require $n_{s,\text{max}}$, θ_0 , and θ_{100} for both electrode materials to initialize a simulation.

If the electrode chemistries are known, then some of these parameter values are available from the literature. The OCP functions $U_{\text{ocp}}(\theta)$ will be known, and we can compute $\theta = n_s/n_{s,\text{max}}$ if we are able to determine $n_{s,\text{max}}$. Therefore, we need only find $n_{s,\text{max}}$, θ_0 and θ_{100} for both electrodes.

To do so, we first charge the battery cell to 100% SOC to initialize the OCV test. The test begins by very slowly discharging the cell down to 0% SOC. (The desire is for the cell to be in a pseudo-equilibrium condition at all times;

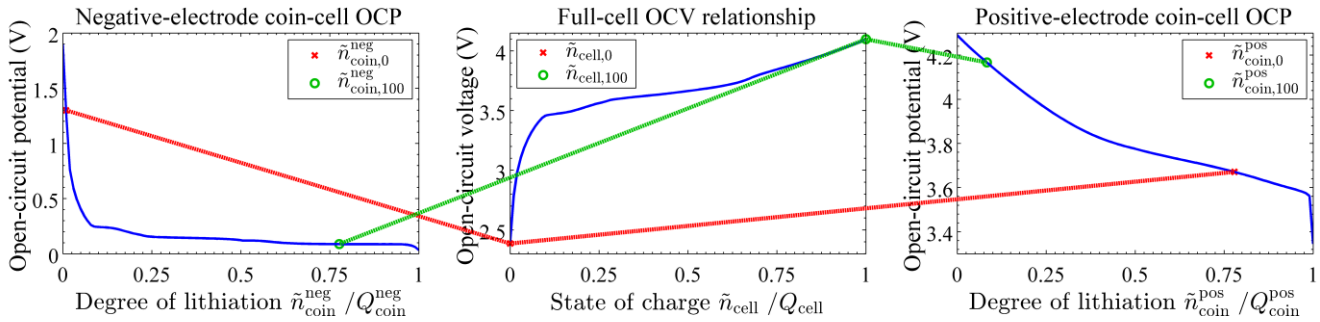


Fig. 1, Example showing relationship between electrode coin-cell OCP functions and cell OCV function.

however, that would require infinitely long test duration. A good compromise is a discharge rate of about C/30.) Then, the cell is very slowly recharged to 100% SOC. Voltage and net ampere-hours discharged at every point in the test are recorded. Cell open-circuit voltage can be approximated as the average of the charge and discharge voltages at every SOC during the test.

When the cell is at 100% SOC, then both electrodes will have stoichiometry equal to their respective θ_{100} values. Similarly, when the cell is at 0% SOC, then both electrodes will be at their respective θ_0 values. At every point in the test, the OCV is equal to the OCP of the positive electrode minus the OCP of the negative electrode at the present electrode θ values. To find θ_0 and θ_{100} for both electrodes, we perform a nonlinear optimization that matches the cell OCV curve with the difference between electrode OCP curves. The optimization is initialized with guesses for θ_0 and θ_{100} for both electrodes; then, these four values are adjusted to better match the OCV to the OCP curves. In MATLAB®, the `lsqnonlin` function from its Optimization Toolbox™ can be used, for example. This optimization takes on the order of a few seconds to complete.

Cell total capacity (in mol) is equal to

$$Q = n_{s,\max} |\theta_{100} - \theta_0|.$$

So, once we have optimized the θ values, we can use the maximum discharged capacity Q from the OCV test and the θ values to determine the values of $n_{s,\max}$ for each electrode.

3.2. WHEN THE ELECTRODE CHEMISTRIES ARE UNKNOWN

Different steps are required if the electrode chemistries are unknown. We are not aware of any way to avoid a minimal cell teardown in this case.

To find the needed functions and parameters, the cell is opened and coin cells are made of negative-electrode active materials versus lithium metal and positive-electrode active materials versus lithium metal. The same discharge/charge test as was outlined in Sect. 3.1 is performed on these coin cells (in addition to the full cell). However, for the coin cells, we don't know a priori the voltage limits for the electrodes that correspond to 100% and 0% cell SOC. Therefore, we assume some voltage limits and charge *above* the assumed maximum voltage and discharge *below* the assumed minimum voltage to

ensure that the OCP curves that we identify contain the range of stoichiometries that will be needed by the model.

Averaging the discharge and charge voltages for the coin cells at every net ampere-hour point in the test gives us OCP relationships as functions of excess lithiation beyond the (unknown) initial lithiation \vec{n}_{coin} of the coin cell, measured in ampere-hours. (When the coin cells are initially charged to the starting voltage for the OCP test, there is a nonzero unknown amount of lithium present, which must be identified to create an accurate model.) The OCP relationships are not yet functions of stoichiometry θ . Additional steps will be required to convert the OCP relationships to functions of θ .

We convert net ampere-hours discharged in an OCP test to moles discharged, denoted as \vec{n}_{coin} by multiplying by $3600/F$. By optimizing the fit between the cell OCV and the electrode OCP curves, we can find operating points $\vec{n}_{\text{coin},0}$ corresponding to θ_0 and $\vec{n}_{\text{coin},100}$ corresponding to θ_{100} . This is illustrated in Fig. 1, which shows OCP curves for example negative- and positive-electrode materials versus lithium metal, and the OCV curve for the overall cell. It also shows $\vec{n}_{\text{coin},0}$ and $\vec{n}_{\text{coin},100}$ values that optimize the fit between the OCV and OCP curves.

We have not yet found the initial lithiation of the coin cell, \vec{n}_{coin} nor the maximum theoretic capacity of the coin cell, $n_{\text{coin},\max}$. It turns out that we will not need to do so. However, by the end of the pulse test, we will be able to calculate these values from those that have been found, if it is of interest to do so.

In summary, by this point we have determined the general shape of the OCP curves. If the electrode chemistries are known, then we have also found $n_{s,\max}$, θ_0 and θ_{100} for both electrodes. If electrode chemistries are unknown, then we have instead found $\vec{n}_{\text{coin},0}$ and $\vec{n}_{\text{coin},100}$ for both electrodes and still need to find \vec{n}_{coin} and $n_{\text{coin},\max}$ to convert $\vec{n}_{\text{coin},0}$ values into θ values. These remaining values will be found by pulse testing.

IV. PULSE TESTS

The OCV tests isolated the pseudo-static thermodynamic properties of the cell. In contrast, the pulse tests are designed to isolate the instantaneous response of the cell to a pulse of input current. This corresponds to an ohmic resistance term.

In the model, lithium concentrations do not react instantly, so parameters corresponding to the solid and electrolyte

concentration equations are not identified by this test. Parameters corresponding to the lithium flux density and the two electric-potential equations are found instead.

Cell resistance is a function of cell SOC as well as the magnitude of the input current (resistance is nonlinear). These two facts allow us to collect sufficiently rich data to identify the majority of the model parameter values using a simple pulse test.

The test is simple. We first fully charge the cell. Then, the cell is allowed to rest until it reaches equilibrium. Next, a discharge pulse is applied, and the instantaneous change in voltage is recorded. This process is repeated at multiple cell SOC values and with multiple pulse magnitudes. Charge pulses can also be applied, and the instantaneous voltage change recorded. Resistance is then computed as the magnitude of the voltage change divided by the magnitude of the current pulse, and is tabulated versus SOC and rate.

To use these data to find model parameter values, we first formulate cell resistance as closed-form equations in terms of the unknown parameter values. Then we use nonlinear optimization to adjust the unknown values until the predicted resistances match the measured resistances as closely as possible. By the end of this step, we will have identified 15 of the 24 model parameter values, plus the two OCP functions.

4.1. CELL RESISTANCE

We are greatly aided by the reduced-order-model (ROM) equations of Lee et al. when determining cell resistance [6,8]. In Lee's ROM, the cell dynamics were approximated, but the instantaneous response was computed exactly in closed form. Since concentrations (and hence open-circuit potential terms) don't change instantaneously, we can write the immediate change in voltage in response to a pulse input as

$$\lim_{t \rightarrow 0^+} v(t) = F[R_{\text{film,tot}}^{\text{pos}} j_{\text{tot}}^{\text{pos}}(3, t) - R_{\text{film,tot}}^{\text{neg}} j_{\text{tot}}^{\text{neg}}(0, t)] + [\tilde{\phi}_e(3, t)]_1 + [\eta^{\text{pos}}(3, t) - \eta^{\text{neg}}(0, t)].$$

The lithium-flux-density and electrolyte-potential terms are linear, so their limit can be written in terms of Laplace-domain transfer functions as

$$\lim_{t \rightarrow 0^+} v_{\text{lin}}(t) = \lim_{s \rightarrow \infty} F[R_{\text{film,tot}}^{\text{pos}} J_{\text{tot}}^{\text{pos}}(3, s) - R_{\text{film,tot}}^{\text{neg}} J_{\text{tot}}^{\text{neg}}(0, s)] + [\tilde{\phi}_e(3, s)]_1.$$

We will see how to evaluate this expression in Sect. 4.2. The nonlinear terms can be computed by taking the limit of

$$\eta(\bar{x}, t) = \frac{2RT}{F} \operatorname{asinh} \left(\frac{j_{\text{tot}}(\bar{x}, t)}{2j_{0,\text{tot}}} \right)$$

where we will evaluate the instantaneous change in j_{tot} using transfer functions, and where we compute $j_{0,\text{tot}}$ as

$$j_{0,\text{tot}} = k_{\text{step}} \sqrt{c_{e,\text{ratio}}} \sqrt{n_{s,\text{max}} - n_s} \sqrt{n_s}.$$

For the pulse tests, $c_{e,\text{ratio}} = 1$ since the pulse is applied when the cell is in equilibrium. The parameter k_{step} is an unknown to be found by the pulse-test data. If the electrode chemistries are known, then $n_{s,\text{max}}$ was already found as part of the OCV test;

otherwise, it will be optimized as part of the pulse test. In either case, the pulse test will optimize $n_{s,0}$ for both electrodes such that we can compute n_s from cell SOC z and capacity Q as

$$n_s^{\text{neg}} = n_{s,0}^{\text{neg}} + zQ$$

$$n_s^{\text{pos}} = n_{s,0}^{\text{pos}} - zQ.$$

If the electrode chemistries are not known a priori, then the pulse tests will optimize values for both $n_{s,\text{max}}$ and $n_{s,0}$ for both electrodes, where the conversion between full-cell normalized electrode concentrations and coin-cell normalized electrode concentrations is done via:

$$n_s^{\text{neg}} = n_{s,0}^{\text{neg}} + Q \frac{\tilde{n}_{\text{coin}}^{\text{neg}} - \tilde{n}_{\text{coin},0}^{\text{neg}}}{\tilde{n}_{\text{coin},100}^{\text{neg}} - \tilde{n}_{\text{coin},0}^{\text{neg}}}$$

$$n_s^{\text{pos}} = n_{s,0}^{\text{pos}} - Q \frac{\tilde{n}_{\text{coin}}^{\text{pos}} - \tilde{n}_{\text{coin},0}^{\text{pos}}}{\tilde{n}_{\text{coin},100}^{\text{pos}} - \tilde{n}_{\text{coin},0}^{\text{pos}}}.$$

This relationship also allows us to solve for \tilde{n}_{coin} from n_s to look up an OCP value from the coin-cell experiments. It was derived using:

$$\tilde{n}_{\text{coin}}^{\text{neg}} = \tilde{n}_{\text{coin},0}^{\text{neg}} + z(\tilde{n}_{\text{coin},100}^{\text{neg}} - \tilde{n}_{\text{coin},0}^{\text{neg}})$$

$$\tilde{n}_{\text{coin}}^{\text{pos}} = \tilde{n}_{\text{coin},0}^{\text{pos}} - z(\tilde{n}_{\text{coin},100}^{\text{pos}} - \tilde{n}_{\text{coin},0}^{\text{pos}}).$$

Once we have found $n_{s,\text{max}}$ and $n_{s,0}$, we can compute n_s in both electrodes for any cell SOC of interest, and from that we can compute the stoichiometric operating points via $\theta = n_s/n_{s,\text{max}}$. Therefore, we can now compute the OCP curves for both electrodes as functions of θ .

4.2. TRANSFER FUNCTIONS FOR PULSE TESTS

In Lee et al. [6,8], a cell ROM is made by linearizing the PDE model and creating transfer functions of the electrochemical variables. These transfer functions shared a common impedance ratio

$$\nu^2(s) = \frac{\frac{1}{\sigma_{\text{tot}}} + \frac{1}{\kappa_{\text{tot}}}}{R_{s,e,\text{tot}} + \frac{1}{FD_{s,\text{tot}}} \left[\frac{\partial U_{\text{ocp}}}{\partial n_{s,e}} \Big|_{n_{s,0}} \right] \left[\frac{1}{1 - \sqrt{\frac{s}{D_{s,\text{tot}}}} \coth \left(\sqrt{\frac{s}{D_{s,\text{tot}}}} \right)} \right]},$$

where

$$R_{s,e,\text{tot}} = R_{\text{ct,tot}} + R_{\text{film,tot}}.$$

In [6], the charge-transfer resistance was found to be

$$R_{\text{ct,tot}} = \frac{RT}{F^2 j_{0,\text{tot}}},$$

when expressed in reformulated parameters. However, this equation was derived under the assumption that the cell current is small, which is not true for the pulse-testing system-identification step. In [10], Lee derived a different charge-transfer resistance that applies even for large pulses:

$$R_{\text{ct,tot}} = \frac{RT}{F^2 \sqrt{j_{0,\text{tot}}^2 + (i_{\text{app}}/(2F))^2}}.$$

We use this formulation of $R_{\text{ct,tot}}$ in the following.

TABLE III, PARAMETERS FOUND BY END OF PULSE TESTING

| Negative electrode | Separator | Positive electrode |
|------------------------------------|------------------------------------|------------------------------------|
| $\sigma_{\text{tot}}^{\text{neg}}$ | | $\sigma_{\text{tot}}^{\text{pos}}$ |
| $\kappa_{\text{tot}}^{\text{neg}}$ | $\kappa_{\text{tot}}^{\text{sep}}$ | $\kappa_{\text{tot}}^{\text{pos}}$ |
| $k_{\text{step}}^{\text{neg}}$ | | $k_{\text{step}}^{\text{pos}}$ |
| $n_{s,\text{max}}^{\text{neg}}$ | | $n_{s,\text{max}}^{\text{pos}}$ |
| $R_{\text{film,tot}}^{\text{neg}}$ | | $R_{\text{film,tot}}^{\text{pos}}$ |
| θ_0^{neg} | | θ_0^{pos} |
| $\theta_{100}^{\text{neg}}$ | | $\theta_{100}^{\text{pos}}$ |

By the initial-value theorem, we will need to find the limit of several transfer functions as s approaches infinity. In the limit, the impedance ratio (square root) becomes

$$\nu_{\infty} = \sqrt{\frac{1}{\kappa_{\text{tot}}} + \frac{1}{\sigma_{\text{tot}}}} \sqrt{\frac{1}{R_{s,e,\text{tot}}}}$$

This will be substituted into the following transfer functions.

The transfer function for lithium flux density in the negative electrode can be written in terms of the reformulated parameters as:

$$\frac{J_{\text{tot}}(z, s)}{I_{\text{app}}(s)} = \nu(s) \frac{\sigma_{\text{tot}} \cosh(\nu(s)z) + \kappa_{\text{tot}} \cosh(\nu(s)(z-1))}{F(\kappa_{\text{tot}} + \sigma_{\text{tot}}) \sinh(\nu(s))},$$

where $z = \bar{x}$ in the negative electrode. In the positive electrode, the transfer function is multiplied by -1 and we substitute $z = 3 - \bar{x}$. When s approaches infinity, we have

$$\frac{J_{\text{tot},\infty}(0)}{I_{\text{app}}(s)} = \frac{\nu_{\infty} (\sigma_{\text{tot}} + \kappa_{\text{tot}} \cosh(\nu_{\infty}))}{F(\kappa_{\text{tot}} + \sigma_{\text{tot}}) \sinh(\nu_{\infty})}$$

at the current-collector locations.

The transfer function for the linear part of the electrolyte potential at the positive-electrode current collector is

$$\begin{aligned} \frac{[\tilde{\Phi}_e(3, s)]_1}{I_{\text{app}}(s)} = & - \frac{(\sigma_{\text{tot}}^{\text{neg}} - \kappa_{\text{tot}}^{\text{neg}}) \tanh\left(\frac{\nu^{\text{neg}}(s)}{2}\right)}{\kappa_{\text{tot}}^{\text{neg}} (\kappa_{\text{tot}}^{\text{neg}} + \sigma_{\text{tot}}^{\text{neg}}) \nu^{\text{neg}}(s)} \\ & - \frac{(\sigma_{\text{tot}}^{\text{pos}} - \kappa_{\text{tot}}^{\text{pos}}) \tanh\left(\frac{\nu^{\text{pos}}(s)}{2}\right)}{\kappa_{\text{tot}}^{\text{pos}} (\kappa_{\text{tot}}^{\text{pos}} + \sigma_{\text{tot}}^{\text{pos}}) \nu^{\text{pos}}(s)} \\ & - \frac{1}{(\kappa_{\text{tot}}^{\text{neg}} + \sigma_{\text{tot}}^{\text{neg}})} - \frac{1}{\kappa_{\text{tot}}^{\text{sep}}} - \frac{1}{(\kappa_{\text{tot}}^{\text{pos}} + \sigma_{\text{tot}}^{\text{pos}})}. \end{aligned}$$

In the limit as s approaches infinity, this becomes

$$\begin{aligned} \frac{[\tilde{\Phi}_e,\infty(3)]_1}{I_{\text{app}}(s)} = & - \frac{(\sigma_{\text{tot}}^{\text{neg}} - \kappa_{\text{tot}}^{\text{neg}}) \tanh\left(\frac{\nu_{\infty}^{\text{neg}}}{2}\right)}{\kappa_{\text{tot}}^{\text{neg}} (\kappa_{\text{tot}}^{\text{neg}} + \sigma_{\text{tot}}^{\text{neg}}) \nu_{\infty}^{\text{neg}}} \\ & - \frac{(\sigma_{\text{tot}}^{\text{pos}} - \kappa_{\text{tot}}^{\text{pos}}) \tanh\left(\frac{\nu_{\infty}^{\text{pos}}}{2}\right)}{\kappa_{\text{tot}}^{\text{pos}} (\kappa_{\text{tot}}^{\text{pos}} + \sigma_{\text{tot}}^{\text{pos}}) \nu_{\infty}^{\text{pos}}} \\ & - \frac{1}{\kappa_{\text{tot}}^{\text{neg}} + \sigma_{\text{tot}}^{\text{neg}}} - \frac{1}{\kappa_{\text{tot}}^{\text{sep}}} - \frac{1}{\kappa_{\text{tot}}^{\text{pos}} + \sigma_{\text{tot}}^{\text{pos}}}. \end{aligned}$$

In summary, pulse-test resistances can be expressed in terms of all parameters found by the OCV tests plus the additional parameters listed in Table III. Optimizing the values in Table III so that predicted resistances match measured resistances at different levels of input current and

cell SOC gives us a little over half of the model parameters. Optimizing this set of parameters takes on the order of tens of seconds using the MATLAB® Optimization Toolbox™.

V. EIS TESTS

The remaining model parameter values may be found via EIS tests. To do so, we measure the frequency response of the cell around different SOC values and optimize the remaining model parameters so the model frequency response matches the measured frequency response as well as possible.

The small-signal transfer function of a cell can be expressed as [8]:

$$\begin{aligned} \frac{\tilde{V}(s)}{I_{\text{app}}(s)} = & FR_{s,e,\text{tot}}^{\text{pos}} \frac{J_{\text{tot}}(3, s)}{I_{\text{app}}(s)} - FR_{s,e,\text{tot}}^{\text{neg}} \frac{J_{\text{tot}}(0, s)}{I_{\text{app}}(s)} + \frac{[\tilde{\Phi}_e(3, s)]_1}{I_{\text{app}}(s)} \\ & + \frac{2RT(1-t_+^0)}{F} \left[\frac{\tilde{C}_{e,\text{ratio}}(3, s)}{I_{\text{app}}(s)} - \frac{\tilde{C}_{e,\text{ratio}}(0, s)}{I_{\text{app}}(s)} \right] \\ & + \left[\frac{\partial U_{\text{ocp}}^{\text{pos}}}{\partial n_{s,e}^{\text{pos}}} \right]_{n_{s,0}^{\text{pos}}} \frac{\tilde{N}_{s,e}^{\text{pos}}(3, s)}{I_{\text{app}}(s)} - \left[\frac{\partial U_{\text{ocp}}^{\text{neg}}}{\partial n_{s,e}^{\text{neg}}} \right]_{n_{s,0}^{\text{neg}}} \frac{\tilde{N}_{s,e}^{\text{neg}}(0, s)}{I_{\text{app}}(s)}. \end{aligned}$$

This can be turned into a frequency response by making the substitution $s = j\omega$. We have already seen transfer functions for the lithium flux density and the linear part of the electrolyte potential. To evaluate this frequency response, we further need transfer functions for the electrolyte concentration ratio and the solid concentration.

The transfer function for solid concentration in the negative electrode can be found to be

$$\begin{aligned} \frac{\tilde{N}_{s,e}(z, s)}{I_{\text{app}}(s)} = & \left[\frac{\sigma_{\text{tot}} \cosh(\nu(s)z) + \kappa_{\text{tot}} \cosh(\nu(s)(z-1))}{3FD_{s,\text{tot}}(\kappa_{\text{tot}} + \sigma_{\text{tot}}) \sinh(\nu(s))} \right] \\ & \times \left[\frac{\nu(s)}{1 - \sqrt{s/D_{s,\text{tot}}} \coth(\sqrt{s/D_{s,\text{tot}})}} \right]. \end{aligned}$$

In the positive electrode, the transfer function is simply multiplied by -1 .

The transfer functions for the electrolyte concentration ratio are quite lengthy, and we don't have room to reproduce them here. They can be found by taking the transfer functions for electrolyte concentration from [6,8], reformulating in terms of the new model parameters, and dividing by $c_{e,0}$. The $(1-t_+^0)$ term in the frequency response is absorbed into the transfer functions such that only the lumped parameters defined to date are needed to express it.

In summary, a cell's frequency response can be expressed in terms of all parameters found by the OCV and pulse tests plus all additional unknown cell parameter values. Optimizing the remaining unknown parameter values such that the predicted frequency response matches the measured frequency response at different cell SOC's give us the complete identified model except for t_+^0 , which is a value that we assume in this work (but, see discussion in Sect. VII, where we mention an additional step that can be used to find this value as well). Optimization of this set of parameters takes on the order of a few minutes using MATLAB®'s Optimization Toolbox™.

TABLE IV. PARAMETERS USED IN SIMULATION

| Symbol | Units | Negative electrode | Separator | Positive electrode |
|--------------------|--|------------------------|-----------------------|------------------------|
| L | μm | 128 | 76 | 190 |
| R_s | μm | 12.5 | — | 8.5 |
| A | m^2 | 1 | 1 | 1 |
| σ | S m^{-1} | 100 | — | 3.8 |
| ε_s | $\text{m}^3 \text{m}^{-3}$ | 0.471 | — | 0.297 |
| ε_e | $\text{m}^3 \text{m}^{-3}$ | 0.357 | 0.724 | 0.444 |
| brug | — | 1.5 | — | 1.5 |
| $c_{s,\text{max}}$ | mol m^{-3} | 26 390 | — | 22 860 |
| $c_{e,0}$ | mol m^{-3} | 2 000 | 2 000 | 2 000 |
| θ_0 | — | 0.05 | — | 0.78 |
| θ_{100} | — | 0.53 | — | 0.17 |
| D_s | $\text{m}^2 \text{s}^{-1}$ | 3.9×10^{-14} | — | 1.0×10^{-13} |
| D_e | $\text{m}^2 \text{s}^{-1}$ | 7.5×10^{-11} | 7.5×10^{-11} | 7.5×10^{-11} |
| t_+^0 | — | 0.363 | 0.363 | 0.363 |
| k | $\text{mol}^{-1/2} \text{m}^{5/2} \text{s}^{-1}$ | 1.94×10^{-11} | — | 2.16×10^{-11} |
| α | — | 0.5 | — | 0.5 |
| R_{film} | Ωm^2 | 0.0 | — | — |

VI. RESULTS

As a feasibility test of the proposed approach, we implemented the methodology in simulation. This has the advantage that the actual parameter values are known exactly, so identification results can be verified directly. It does have several limitations, however, as discussed in Sect. VII.

The assumed cell parameter values are from [2] and are listed in Table IV. In addition to the parameter values listed in the table, we also model the effective conductivities and diffusivities as

$$\begin{aligned}\sigma_{\text{eff}} &= \sigma \varepsilon_s^{\text{brug}} \\ \kappa_{\text{eff}} &= \kappa \varepsilon_e^{\text{brug}} \\ D_{e,\text{eff}} &= D_e \varepsilon_e^{\text{brug}};\end{aligned}$$

we model the electrolyte conductivity (in S m^{-1}) as

$$\begin{aligned}\kappa(c_e) &= 4.1253 \times 10^{-2} + 5.007 \times 10^{-4} c_e - 4.7212 \times 10^{-7} c_e^2 \\ &\quad + 1.5094 \times 10^{-10} c_e^3 - 1.6018 \times 10^{-14} c_e^4\end{aligned}$$

the negative-electrode OCP in V as

$$U_{\text{ocp}}^{\text{neg}}(\theta) = -0.16 + 1.32 \exp(-3.0\theta) + 10.0 \exp(-2000.0\theta),$$

and the positive-electrode OCP in V as

$$\begin{aligned}U_{\text{ocp}}^{\text{pos}}(\theta) &= 4.19829 + 0.0565661 \tanh(-14.5546\theta + 8.60942) \\ &\quad - 0.0275479 \left[\frac{1}{(0.998432 - \theta)^{0.4924656}} - 1.90111 \right] \\ &\quad - 0.157123 \exp(-0.04738\theta^6) \\ &\quad + 0.810239 \exp[-40(\theta - 0.133875)].\end{aligned}$$

In this case, we assumed that we “knew” the chemistries of the two electrodes, so simply must find the θ values for both electrodes via the OCV tests. These were identified with high precision.

Data for the pulse tests were collected by simulating the FOM in COMSOL Multiphysics for different equilibrium SOC initializations and for different charge and discharge pulse magnitudes. Care had to be taken to add second-order smoothing to the input pulse to avoid problems with simulation convergence. Resistance was measured as the absolute voltage change between the equilibrium voltage and the cell voltage measured shortly after the application of the current pulse (the short delay was necessary to account for the time lag of the second-order smoothing), divided by the input-current pulse magnitude. These data, normalized to the C rate of the cell, are plotted in Fig. 2. We see that cell resistance is a nonlinear function of input-current magnitude and SOC. The fact of this nonlinearity is critical for the pulse testing to be able to extract multiple parameters from the same test. If the resistance were linear, we would not be able to distinguish between the components that comprise its calculation; because it is nonlinear, we are able to do so.

Nonlinear optimization was performed to optimize values for the parameters listed in Table III. Candidate values for these parameters were inserted into the equations that predict cell resistance; these resistances were then compared to the measured resistances of Fig. 2; the candidate values were then adapted to optimize the fit between the predicted and measured resistances. At the end of the optimization, the difference between the measured and predicted resistances was very small (on the order of $\text{n}\Omega$), and is plotted in Fig. 3. Optimized pulse-test parameter values are presented in Table V.

We see that the conductivities were identified very well. The worst-case result was on the order of 2% relative error (σ_{tot} for the negative electrode). The k_{step} parameters were identified with negligible error and the film-resistance values had high *relative* error, but low *absolute* error: the errors were not significant at the output of the model.

Data for the EIS tests were collected using a small-signal reduced-order model [8], although different approaches could have been used (e.g., see [11]). These data are plotted in Figs. 4 and 5. We see some nonlinear variation with respect to SOC, but not nearly as much as for the pulse-test data. (This uniformity limits our ability to identify different parameters in the model uniquely. In a physical cell, we would expect more variation than this.)

Nonetheless, the identification results using this data were quite good. Identified parameter values are listed in Table VI. The biggest challenge at this point is in estimating the lumped electrolyte values $L_{e,\text{mod}}$. All other parameters were estimated well.

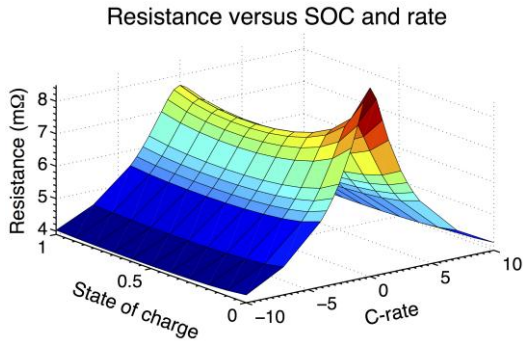


Fig.2, Resistance of Doyle cell.

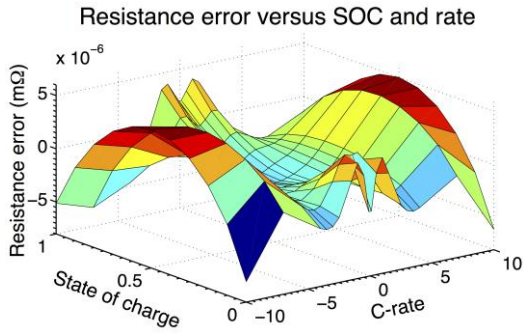


Fig.3, Error in estimates of Doyle-cell resistance.

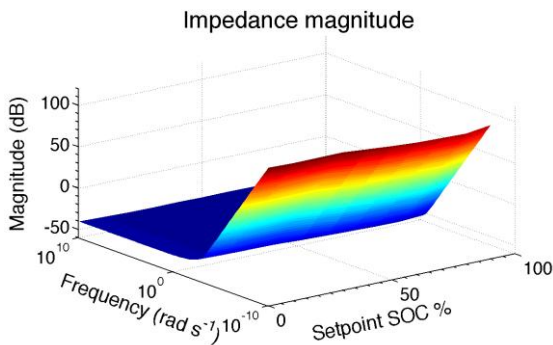


Fig. 4, Doyle-cell impedance magnitude.

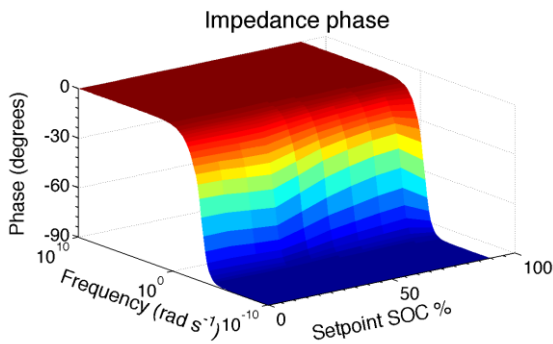


Fig.5, Doyle-cell impedance magnitude.

VII. DISCUSSION

These results have demonstrated that the proposed methodology works quite well in an ideal setting—when the actual cell dynamics exactly match the model of the cell

TABLE V, IDENTIFIED PARAMETERS VIA PULSE TESTS

| Symbol | Units | Negative electrode | Separator | Positive electrode |
|----------------------------|----------|------------------------|-----------|------------------------|
| True parameter values | | | | |
| κ_{tot} | S | 175.65 | 164.12 | 854.38 |
| σ_{tot} | S | 3.680×10^5 | | 5940 |
| $R_{film,tot}$ | Ω | 0 | | 0 |
| k_{step} | s^{-1} | 2.077×10^{-4} | | 3.408×10^{-4} |
| Estimated parameter values | | | | |
| κ_{tot} | S | 175.64 | 164.12 | 854.46 |
| σ_{tot} | S | 3.785×10^5 | | 5944 |
| $R_{film,tot}$ | Ω | 1.07×10^{-7} | | 8.60×10^{-11} |
| k_{step} | s^{-1} | 2.077×10^{-4} | | 3.408×10^{-4} |

TABLE VI, IDENTIFIED PARAMETERS VIA EIS TESTS

| Symbol | Units | Negative electrode | Separator | Positive electrode |
|----------------------------|---------------|-----------------------|-----------------------|-----------------------|
| True parameter values | | | | |
| $D_{s,tot}$ | s^{-1} | 4.01×10^3 | | 7.23×10^2 |
| $D_{e,mod}$ | $mol\ s^{-1}$ | 6.16×10^{-4} | 3.00×10^{-3} | 5.76×10^{-4} |
| $L_{e,mod}$ | mol | 2.25×10^{-1} | 2.71×10^{-1} | 4.16×10^{-1} |
| t_+^0 | — | 0.363 | | |
| Estimated parameter values | | | | |
| $D_{s,tot}$ | s^{-1} | 4.01×10^3 | | 7.23×10^2 |
| $D_{e,mod}$ | $mol\ s^{-1}$ | 6.13×10^{-4} | 2.98×10^{-3} | 5.73×10^{-4} |
| $L_{e,mod}$ | mol | 2.04×10^{-1} | 3.12×10^{-1} | 1.94×10^{-1} |
| t_+^0 | — | Assumed to be 0.363 | | |

dynamics, when measurements are noise-free, and when the input to the cell for different tests can be controlled accurately. We have begun to apply this methodology to actual lithium-ion cells and find that the method also works there, albeit with a few caveats.

It turns out there is some difficulty associated with collecting reliable pulse-test data, especially at high pulse-current magnitudes. One possibility is that the equipment used to generate the pulses is not capable of producing ideal Heaviside step functions; in practice, an oscillation is evident in the input current as the cell tester attempts to converge to the commanded current level, which biases the results. Therefore, we use the pulse testing to give only approximate values to the parameters in Table III, but rely on data collected from the subsequent tests to refine the estimates.

Due in part to the difficulty of collecting reliable pulse-test data, we also conduct an additional steady-state resistance test. The additional data is helpful in achieving convergence of

consistent parameter value sets. Further, it allows us to identify t_+^0 and $c_{e,0}$ uniquely.

Additionally, the cell model used in the work presented here did not consider the effects of a double-layer capacitance. It turns out that this capacitance tends to charge and discharge quickly so that from a practical point of view it does not have a large impact on long-term model predictions. Nevertheless, it does significantly change the EIS results at high frequencies. We therefore find it necessary to include the double-layer capacitance in our methodology to identify model parameters for physical cells.

Finally, we do not address error bounds on the identified parameters within this work. We plan to use the methods proposed in [9] to do so in future research. Indeed, results of system ID on physical cells is a topic of planned future publications.

VIII. CONCLUSION

We believe that physics-based models of lithium-ion cells will be required by future battery-management systems in order to optimize the performance/lifetime tradeoff for large battery packs. For this to be practical, we must be able to identify the parameter values of the physics-based models. In the past, manufacturers have been reluctant to disclose this information, so we must find other ways to discover it.

This paper has proposed a methodology that can be used to find physics-based lithium-ion cell-model parameter values. We began by reformulating the equations to eliminate redundant and unobservable dimensional parameters from the model—these parameters are not necessary to being able to simulate the model equations. We then proposed OCV, pulse, and EIS testing to collect data to be used when finding the parameter values. Each test isolated a group of parameters such that the optimizations required to perform the parameter fits was minimized in scope, which makes it quite fast.

If electrode chemistries are known, no cell teardown is needed. The entire system-identification process can be accomplished via cell-level testing only. If electrode chemistries are unknown, a minimal teardown is required to form coin cells from the electrode materials in order to determine OCP data. This is a relatively straightforward and inexpensive task.

We used simulation in this paper to create the data to be used by the methodology so that we could have known “truth” values for all parameters against which to compare results. The identified parameter values agreed with the truth values very well in all cases. For physical cells, we mentioned some additional steps that should be taken to improve on these methods. We plan to publish results for physical cells in the near future.

VIII. DISCLAIMER

The information, data, or work presented herein was funded in part by an agency of the United States Government. Neither

the United States Government nor any agency thereof, nor any of their employees, makes any warranty, express or implied, or assumes any legal liability or responsibility for the accuracy, completeness, or usefulness of any information, apparatus, product, or process disclosed, or represented that its use would not infringe privately owned rights. References herein to any specific commercial product, process, or service by trade name, trademark, manufacturer, or otherwise does not necessarily constitute or imply its endorsement, recommendation, or favoring by the United States Government or any agency thereof. The views and opinions of authors expressed herein do not necessarily state or reflect those of the United States Government or any agency thereof.

IX. ACKNOWLEDGMENT

The information, data, or work presented herein was funded in part by the Advanced Research Projects Agency-Energy (ARPA-E), U.S. Department of Energy, under Award Number DE-AR0000271.

This work used the EAS Data Center or EAS Cloud, which is supported by the College of Engineering and Applied Science, University of Colorado Colorado Springs.

REFERENCES

- [1] X. Hu, S. Li, and H. Peng, “A Comparative Study of Equivalent Circuit Models for Li-ion Batteries,” *Journal of Power Sources*, **198**, 359–367, 2012.
- [2] M. Doyle, J. Newman, A.S. Gozdz, C.N. Schmutz, and J-M Tarascon, “Comparison of Modeling Predictions with Experimental Data from Plastic Lithium Ion Cells,” *J. Electrochem. Soc.*, **143**(6), 1890–1903, 1996.
- [3] K.A. Smith, C.-Y. Wang, “Power and Thermal Characterization of a Lithium-Ion Battery Pack for Hybrid-Electric Vehicles,” *Journal of Power Sources*, **160**, 662–673, 2006.
- [4] G.L. Plett, *Battery Management Systems, Volume II: Equivalent-Circuit Methods*, Artech House, 2016.
- [5] J.L. Lee, A. Chemistruck, and G.L. Plett, “Discrete-Time Realization of Transcendental Impedance Functions, with Application to Modeling Spherical Solid Diffusion,” *Journal of Power Sources*, **206**, 367–377, 2012.
- [6] J.L. Lee, A. Chemistruck, and G.L. Plett, “One-Dimensional Physics-Based Reduced-Order Model of Lithium-Ion Dynamics,” *Journal of Power Sources*, **220**, 430–448, 2012.
- [7] J.L. Lee, L. Aldrich, K. Stetzel, and G.L. Plett, “Extended Operating Range for Reduced-Order Model of Lithium-Ion Cells,” *Journal of Power Sources*, **255**, 85–100, 2014.
- [8] G.L. Plett, *Battery Management Systems, Volume I: Battery Modeling*, Artech House, 2015.
- [9] J.C. Forman, S.J. Moura, J.L. Stein, and H.K. Fathy, “Genetic Identification and Fisher Identifiability Analysis of the Doyle–Fuller–Newman Model from

- Experimental Cycling of a LiFePO₄ Cell,” *Journal of Power Sources*, **210**, 263–275, 2012.
- [10] J.L. Lee, *Reduced-Order Physics-Based Model of Lithium-Ion Batteries*, PhD dissertation, University of Colorado Colorado Springs, Ch. 6, 2012.
- [11] M. Doyle, J.P. Meyers, and J. Newman, “Computer Simulations of the Impedance Response of Lithium Rechargeable Batteries,” *J. Electrochem. Soc.*, **147**, 99–110, 2000.



Governing the market entry of marine energy by symptom-adapted interventions: (i) reduction of detail complexity; and (ii) managing dynamically complex tasks

通过随症状干预来进行海洋能的市场进入治理： (一) 减排细节复杂性；(二) 管理动态复杂任务

Ralf Bucher^{1*}, Ian Bryden²

¹University of Edinburgh, Institute for Energy Systems, Mayfield Road, Edinburgh, EH9 3JL, UK

²University of the Highlands and Islands, Ness Walk, Inverness, IV3 5SQ, UK

r.bucher@sms.ed.ac.uk

Accepted for publication on 12th October 2015

Abstract – Governing the market entry of marine energy represents a challenging endeavour that is confronted by a series of obstacles. The harsh marine environment places considerable demands on the quality of the deployed structures and devices. Apart from technological difficulties, achieving funding is a central problem as investors show a clear preference for more mature, proven technologies. To overcome the present pre-profit phase, two different solution approaches are required: one for solving complicated technology-related or organisational tasks and another for strategic remits. In the paper, a methodology to systematically identify critical success factors is presented, and propositions to tackle detail and dynamic complexity, correlated with the commercialisation of marine energy, are made.

Keywords – Marine energy, market entry, detail and dynamic complexity, system dynamics modelling.

I. INTRODUCTION

Marine energy finds itself in a decisive transition phase with operating full-scale demonstrators but an outstanding proof of the technological concept in a commercial power generation environment. Consequently, the industry goal to deliver projects of up to 50 MW by 2020 [1] requires critical evaluation, especially when considering the setbacks and delays experienced in the last years.

Managing the market entry of tidal stream and wave power represents an ambitious undertaking. In the course of a recent expert interview series, the top-ranked risks for utility-scale

project implementations were identified as *uncertainty in device performance* and *achieving funding*. To ensure continuous progress on the way towards subsidy-free electricity generation, diverse problem-solving competencies are necessary. On one side, we encounter technical difficulties that require profound engineering know-how and on the other, tasks of a more strategic nature that require qualitative assessment capabilities and advanced management concepts.

The tasks correlated with the commercialisation of marine energy can be sub-divided into questions of *detail complexity* (also referred to as *complicacy*) and *dynamic complexity*. Reducing the core problem *uncertainty in device performance* is a challenging but conventional engineering task, whereas *achieving funding* is more demanding and requires the ability to cope with many interlinked impact factors at different time scales (i.e. a classic example for dynamic complexity). In this paper, the distinctly different strategies for solving detail-complex problems and appropriately managing dynamically complex tasks are described.

II. OBJECTIVE OF THE RESEARCH

The underlying objective of this research is to de-risk and streamline the commercialisation of power generation by tidal stream and wave power technologies. The provision of problem-specific analyses and solution approaches aims to rapidly achieve a solid and sustainable market breakthrough.

The research is oriented around the hypothesis:

The market entry of marine energy can be de-risked by symptom-adapted interventions: (i) reduction of detail complexity; and (ii) managing dynamically complex tasks by qualitative feedback modelling.

The long-term focus is on establishing marine energy as a market competitive generation alternative with commercially viable projects implemented on a regular basis.

III. RESEARCH PRINCIPLE AND METHODOLOGY

In the scientific literature on complexity research, the fundamental difference between detail and dynamic complexity is underlined [2,3]. Studies in the field of system dynamics revealed that in conventional management mainly aspects of detail complexity are considered, but that the real leverage lies in understanding dynamic complexity [4]. Senge [5] states, that most planning tools and analytical methods are not equipped to handle dynamic complexity.

In this contribution, a comprehensive approach to manage dynamic complexity correlated with the maturation and market entry process of marine energy has been chosen. The integration of a wide spectrum of perspectives in a systematic and transparent manner is a core principle applied in this research¹. Different sources of knowledge are compiled to identify an optimum commercialisation strategy.

As for dynamically complex situations, a reduction of complexity can be counterproductive, qualitative feedback modelling is seen as the preferred approach [6]. In this case, expert interview information as input data and numerical modelling by system dynamics software is required.

In the course of the present research, several system dynamics models were built to fulfil the requirements of a qualitative feedback modelling process. In the initial model, the effects of dynamic complexity were considered by identifying the long-term top-level driving factors for the commercialisation of marine energy. Based on the achieved finding to focus on *showcasing commercial-scale projects/successful demonstrators*, two further system dynamics models, concentrating on aspects of detail and dynamic complexity, were developed. In order to cross-check and substantiate the results, diametrically opposite perspectives were taken to analyse the supporting and hindering impacts on the marine energy development and maturation process.

The following chronological tasks have been performed: (i) elaboration of a target-oriented questionnaire; (ii) conduction of expert interviews; (iii) compression of information by ordering terms; (iv) configuration of system dynamics

¹ By contacting 136 selected representatives from 15 stakeholder groups, we received 71 feedbacks out of which originated 11 personal and 15 telephone interviews as well as 20 filled-out questionnaires. Two questionnaires had to be discarded because they were incomplete. As a result, the knowledge of 44 managers, experts and specialists from 13 stakeholder groups was ultimately retained for the analysis. A total number of 2,129 individual replies had to be grouped in order to formulate higher-level correlations as the input for computer-based system dynamics analyses.

computer models; (v) calculated ranking of impact factors and determination of top-level driving factors; (vi) allocation of representative core statements; and (vii) elaboration of strategies to de-risk the technology and to govern the market entry process.

IV. WHICH TASKS ARE COMPLICATED AND WHICH ARE DYNAMICALLY COMPLEX?

4.1. LARGE-SCALE ENGINEERING & CONSTRUCTION PROJECTS

Söderlund [7] formulates that large-scale transformation projects (for which the maturation process and market launch of marine energy is an example) are characterised by involving several hundred individuals, different technologies, numerous knowledge bases, complex contractual structures and a wide range of development activities with parallel operations.

Sterman [8] demonstrates in the context of large-scale engineering and construction projects, that they consist of many *interdependent components, involve multiple feedback processes, non-linear relationships, accumulation or delay functions*, and belong, as such, to the group of *complex dynamic systems*. He emphasises that cause and effect can be subtle and *obvious interventions can produce non-obvious consequences*.

Within a research on project management, Ahern et al. [9] make the important distinction between detail-complex and dynamically complex projects. They criticise that – in line with the finding of Hayek [10] that dynamically complex tasks cannot be completely specified in advance – traditional project management privileges planning and downplays the role of learning. *Planning and problem-solving must be dealt with differently*, as summarised by Swinth [11].

4.2. DETAIL COMPLEXITY (TECHNICAL COMPLICACY)

Detail complexity is characterised by *many interacting elements and a large number of combinatorial possibilities*. The respective tasks are characterised by their high level of technical or organisational complicacy. Nevertheless, they can be planned and handled by the application of prior knowledge, skills and tools. By definition, detail-complex tasks or projects can be completely specified in advance. In the context of marine energy, questions of detail complexity arise in the framework of machinery/component design (blades, rotor, nacelle, foundations, electrical system, protection, controls), in subjects related to deployment, operation and retrieval or in multi-faceted organisational tasks (legal permits, regulatory and consenting process, finance applications).

A simplified formula to describe detail complexity is to exponentiate the number of potential states of each element by the number of elements [12]. This formula is not adequate to calculate dynamic complexity.

4.3. DYNAMIC COMPLEXITY

In the course of a technology convergence process, a project can change its respective characteristics. In aviation history, as exemplarily described by Ahern et al. [9], aircraft design progressed from being a complex project (when the

technology was poorly understood) to a complicated project (when detailed designs are documented for production assembly). Nevertheless, as described by Snowden [13], a one-off project may not transition from being complex to becoming complicated until it is delivered and retrospectively comprehended in its entirety.

Dynamic complexity can arise even in simple systems with low combinatorial diversity and often shows aspects of counter-intuitive behaviour [14,15]. In the course of working on dynamically complex projects, continuous learning and

reliable knowledge formation are paramount. Engwall [16] formulates this within a project management context by saying that it is necessary to continuously create knowledge over the complete project life cycle.

In Table 1, the most typical attributes of complex dynamic systems are presented and correlated to their appearance in the course of the commercialisation of marine energy. In this context, the term *system* refers to a set of rules that governs the *market entry and commercialisation process of marine energy*.

TABLE 1, DYNAMIC COMPLEXITY IN COMMERCIALISING MARINE ENERGY [14,17 – BOTH ADAPTED]

| Attribute | Root cause | Form of appearance |
|---|---|---|
| On-going transformations in the embedding socio-technical system [18] | Innovation and change processes occur at many levels and at different time scales. | The unstable global economic situation constitutes a dynamic environment and changing strategic priorities (nuclear power phase-out, fracking) alter policy orientation. |
| | —► Considering a business environment in which other renewables operate price-competitive to conventional sources and the <i>epochal transformation of the European energy system</i> , the commercialisation strategy needs to be regularly adapted to socio-political developments. | |
| Non-linear development and unsteady system behaviour | Non-linearity arises when (i) multiple factors interact, i.e. by complicated information pathways with many decision points; (ii) cause and effect are distant in time and space; and (iii) effect is rarely proportional to cause. | Leete et al. [19] and Wyatt [20] examined investor attitudes and found that most of them are unlikely to make any future investments in early stage device development. Venture capital investors are not closed to the industry completely, but the current level of risk and uncertainty about future revenues are discouraging them from investing. |
| | —► The commitment of investors is key for the commercialisation of marine energy. The present unpredictability of the costs and the length of time required to develop the technologies limit the incentive to invest and contribute to the <i>unsteady and non-linear progress in the sector</i> . | |
| Counter-intuitive effects and policy resistance | The complexity of the system makes it difficult to fully understand it. The attention is often drawn to symptoms rather than to underlying causes. Many seemingly obvious solutions to problems fail or worsen the situation. | The quality of challenges that the sector faces is illustrated by the decision of Siemens to sell Marine Current Turbines (a key tidal stream device developers) only two years after its acquisition. Siemens is looking to exit marine energy, saying the development of the market and the supply chain has taken longer to grow than expected [21]. |
| | —► The recent decision of Siemens to divest of MCT is a concern for the sector [22] and reveals the <i>difficulty of forecasting the pace of development</i> towards reaching commercial generation. | |
| Adaptive characteristics | Evolution and learning lead to the selection and proliferation of the best concept(s) while others become extinct. Achieving a milestone alters the state of the system, thus giving rise to a new situation, which then influences the next decisions. | Marine energy represents a <i>radical innovation</i> and is driven by the need to de-risk the technology and achieve funding. Before becoming recognised as a mature power generation method, marine energy needs to prove a range of referenceable application cases. The attainment of this <i>array-scale success</i> will represent a major turning point and is expected to finally trigger industry-scale deployment. |
| | —► The economic success of marine energy depends on demonstrating market-readiness. By the game-changing <i>array-scale success</i> , competition between suppliers will shift to a new set of parameters of which the most important one is price [23]. <i>The development trajectory adapts</i> . | |
| Tightly coupled | Heterogeneous stakeholders interact intensively with one another and the natural world. | Interaction of diverge stakeholders such as governments, certifiers, investors, academia, consultancies, developers, owners, operators, manufacturers and test site operators. |
| | —► To successfully realise the marine energy market launch, the <i>regularly coordinated interaction of the policy, technology and finance sectors</i> is necessary. | |

V. GOVERNING THE MARKET ENTRY

In the course of this research, in total, three system dynamics computer models were developed [24]. As the first model serves as a strategic indicator, all reported positive and negative impact factors on the final target of *full commercial*

power generation by marine energy were coherently grouped and inter-correlated. The model was built one-on-one to the interview replies so that it directly reflects the experience and expectations of a wide range of stakeholders. Out of a total of 234 qualitative replies, directly defining the positive and negative impacts on the defined target, seven *representative*

group terms were defined and the individual replies allocated accordingly. In a subsequent step, 16 positive (supporting/accelerating/reinforcing) and 22 negative (hindering/delaying/countervailing) generic terms were formulated to correlate the individual interview replies in a systematic manner according to their number of occurrences [25,26]. The calculated results of the simulations are presented in Table 2. On the left hand side, the impact factors with negative effect

and on the right hand side the ones with positive effect on achieving market-competitive generation are represented. As the singular characteristics of government involvement and decisions are outside the range of this research, the highest ranked positive and negative top-level driving factors (*strong and long-term commitment from government* and *fluctuating or unclear political support*) were not examined in further detail.

TABLE 2, SPLIT RANKING OF TOP-LEVEL DRIVING FACTORS (POSITIVE AND NEGATIVE IMPACT FACTORS)

| Negative (hindering/delaying/countervailing) | Rank | Positive (supporting/accelerating/reinforcing) | Rank |
|--|------|---|------|
| Fluctuating or unclear political support | 47 | Strong and long-term commitment from government | 100 |
| Lack of investor confidence | 45 | Showcase commercial-scale projects/demonstrators | 51 |
| Fragmented initiatives by unexperienced parties | 44 | Engagement industry/academia | 22 |
| Conflicts of interest (fishermen, shipping routes) | 23 | Cost-effective way to harvest marine energy | 18 |
| Low ability of developers to work together | 17 | Collaboration and consolidation between companies | 15 |

The need to *showcase commercial-scale projects/successful demonstrators* and the identified *lack of investor confidence* are directly interdependent as investment decisions depend on track records of continuous device operation. In the centre of this area of conflict, we find the eagerly-awaited *array-scale success*, as passing this interim milestone will give confidence in the innovative sector and de-risk investments.

Subsequently, two more precisely focussed models were built to identify the top-level driving factors for achieving the *array-scale success*. In order to cross-check and substantiate the findings, diametrically opposite perspectives were taken by processing the entities of supporting and hindering impacts.

VI. SYMPTOM-ADAPTED INTERVENTIONS TARGETING ON ROOT CAUSES

6.1. REDUCTION OF DETAIL COMPLEXITY

For detail-complex (or complicated tasks), the application of complexity-reducing measures is expedient [27]. Apart from technology-related questions, detail complexity also appears within stakeholder-internal business management and in tasks of organisational nature. The following measures for complexity-reduction were identified in the course of processing the multi-disciplinary expert interview data:

- (i) Standardisation and certification: Standards are one of the most important elements in the development of any industry [28]. A project developer’s head of offshore operations emphasised, when asked for the most valuable experience gained by the early movers, the *experienced negative impact of missing standardisation*. One interviewee summed up the situation by saying *no standards, no results*. Considering the urgent need for consensus over standardisation, the over-engineering in oil and gas standards was addressed as being potentially hindering for the development of marine energy.
- (ii) Multi-applicable technologies and joint concepts: In the course of the interviews, a power utility ocean energy manager outlined that one of the top-priority tasks in the work of academia and research should be to concentrate

on *multi-applicable technologies* and *compatible devices and components* (e.g. moving parts, cable connectors, controls). To ensure compatible component design, effective supply chain management and leveraging logistics are required. Significant benefits are seen in *joint deployment and maintenance* programmes.

- (iii) Systems engineering: When asked about the potential to reduce the cost for utility-scale project implementations, the CEO of a wave energy firm emphasised the recognition to orientate their development and research strategies at the US space-/aircraft industry and here especially on the systems engineering principles². In the course of the design and deployment of marine energy converters and correlated power infrastructure, *regular system functionality checks*, focussing on operation in open sea, grid-connected, multi-device arrays, are recommended. This statement correlates with the central objective in systems engineering *to consider the finally envisaged functionality already in early project stages*.
- (iv) Reliability modelling: As a key risk for reaching commercial generation, senior members of classification societies stressed *uncertainty about reliability* and emphasised the necessity to focus on it. In order to achieve a satisfactory technology reliability record, the experts recommended concentrating on reliability in system design and introducing *reliability engineering*.

6.2. MANAGING DYNAMIC COMPLEXITY

As a way of dealing with novel and complex tasks, Swinth [11] proposes *joint problem solving* which comprises a *common goal-orientation*, the *linkage of organisational centres* and the definition of an *overall consistent set of actions*. Within an inductive study on product innovation in continuously changing organisations (which are considered by the authors as *complex adaptive systems*), Brown and Eisenhardt [29] proclaim the importance of *extensive communication* and *design freedom* to create improvisation

² The term *systems engineering* can be traced back to the Bell Telephone Laboratories in the 1940s. A.D. Hall presented 'A Methodology for Systems Engineering' (ISBN 0-442-03046-0) at Princeton University in 1962.

within current projects. They summarise that successful firms rely on *experimental products* and *strategic alliances*.

Due to on-going transformations in the embedding socio-technical system, that *encompass the co-evolution of technology and society* [18], the actual lines of strategic development of the marine energy sector need to be regularly re-adjusted. The following concepts are proposed by scholars working in the field of complex systems research:

- (i) **System dynamics techniques:** As an initial step in approaching the characteristics of complex systems, in the mid-1950s, Forrester [30] developed system dynamics as *a methodology and mathematical modelling technique for framing, understanding and discussing complex issues and problems*. Richardson [31] defines system dynamics as *a computer-aided approach to policy analysis and design*. Wu et al. [32] introduce system dynamics as *a manner of systematic thinking that integrates a large number of causal relationships among variables and simulates real systems through high-speed computer processing power*. Forrester [33] describes the system dynamics approach as *a tool for knowledge-based decision-making*. Yim et al. [34] explain that *system dynamics methods support decision-making and enable managers to act under dynamic and non-trivial environments*.
- (ii) **Qualitative feedback modelling:** With a focus on power projects, Groesser [35] argues that dynamic complexity is often the root cause for non-successful projects and introduces *qualitative feedback modelling* as a method to effectively deal with dynamic complexity. In the course of the present research, *qualitative feedback modelling* is not realised in the original form of working based on problem-specific relationship-diagrams, but by directly targeting the final goal of commercial power generation by marine energy. Feedback modelling is hereto realised at a more fundamental level by considering the marine energy commercialisation process as a complex system of which the dynamic characteristics are captured by semi-structured interviews with all active stakeholder groups [26]. The obvious analogy of this process with a closed-loop control circuit and its clearly defined (technical) terms helps to remove barriers [36–39].

As the presented concepts to deal with detail and dynamic complexity were successfully applied in similar environments, they are suitable to support de-risking the market entry of marine energy. The initial hypothesis is confirmed.

VII. CONCLUSION

There are a series of obstacles to the market entry of marine energy. Root causes for the slow commercialisation process are concerns regarding device reliability and difficulties in attracting investment. To successfully establish marine energy as a mature power generation alternative, in-depth engineering capabilities and advanced management skills are required. In order to identify optimum measures, a particular task needs to be assessed in its entirety and corresponding strategies

selected. To solve machinery-related or organisational challenges, a good standard of innovation management and experience is required. Nevertheless, such specialist tasks are, in their principal characteristics, comparable to routinely executed R&D³ activities in high-technology industry sectors.

The more comprehensive and strategically demanding tasks are to attract financing and to successfully embed the innovative generation method into the continuously changing *socio-technical environment*. To be able to adapt to such a discontinuous and non-transparent environment, systemic thinking and evolutionary steering mechanisms are required. The strategy must be flexible and re-adjustable to new trends and priorities.

The commercialisation of marine energy can be regarded as a complex dynamic system that has the capacity to change and learn from experience. There is the necessity to be mindful of the numerous time-driven impact factors and to enable learning by strengthening collaborative problem solving [40,41]. The use of cross-category expert interview data and unbiased system dynamics modelling assure the important open-integrative instead of detailed-specialist character of the research. Based on such a multi-disciplinary attempt, an all-encompassing appraisal becomes possible by avoiding concentrating in a limiting manner on stakeholder-specific views or interests.

Engwall [16] describes that *project execution is seldom a process of implementation, rather it is a journey of knowledge creation*. Reliable communication and efficient knowledge integration are seen as keys for success. The motivation for cooperative interaction to jointly de-risk the concept is given by the aim to rapidly overcome the pre-profit phase [42].

The correct strategic alignment of the sector depends on the input of all key stakeholders. The process of information gathering by *stakeholder-wide expert interviews* and the use of *system dynamics tools* to determine the currently relevant *top-level driving factors* provide a reliable foundation for governing the market entry of marine renewables.

ACKNOWLEDGEMENT

The study is part of a PhD research into strategic risk management for marine energy projects at the Institute for Energy Systems, University of Edinburgh, UK. The first author is grateful to Prof I. Bryden, Prof G. Harrison and H. Jeffrey for their continuous support and inspiring discussions. Thanks to all interview participants and to the anonymous reviewers for providing helpful suggestions.

REFERENCES

- [1] European Ocean Energy Association (2013) Industry Vision, www.oceanenergy-europe.eu [20/02/2014]
- [2] Sterman, J.D. (1994) Learning in and about complex systems, *System Dynamics Review* 10(2-3), pp291–330

³ *Research and development* is a general term for activities in connection with corporate or governmental innovation.

- [3] Schwaninger, M. (2009) Complex versus complicated: The how of coping with complexity, *Kybernetes* 38(1/2), pp83–92, DOI 10.1108/03684920910930286
- [4] Sterman, J.D. (2010) Does system dynamics improve people's understanding of accumulation?, *System Dynamics Review* 26(4), pp316–334
- [5] Senge, P. (1990) *The fifth discipline: The art and practice of the learning organisation*, ISBN 978-0553456349, Crown Publishing, New York
- [6] Cooper, K. & Lee, G. (2009) Managing dynamics of projects and changes, *Proceedings of the International System Dynamics Conference*, USA
- [7] Söderlund, J. (2010) Knowledge entrainment and project management, *International Journal of Project Management* 28, pp130–141
- [8] Sterman, J.D. (1992) *System dynamics modelling for project management*, MIT, Cambridge, USA
- [9] Ahern, T. & Leavy, B. (2014) Complex project management as complex problem solving, *International Journal of Project Management* 32, pp1371–1381
- [10] Hayek, F.A. (1945) The use of knowledge in society, *American Economic Review* 35(4), pp519–530
- [11] Swinth, R.L. (1971) Organizational joint problem-solving, *Management Science* 18(2), pp68–79
- [12] Schwaninger, M. (2009) *Intelligent organizations: Powerful models for systemic management*, Springer, ISBN 978-3540851615
- [13] Snowden, D. (2002) Complex acts of knowing: Paradox and descriptive self-awareness, *Journal of Knowledge Management* 6(2), pp100–111
- [14] Sterman, J.D. (2001) System dynamics modelling: Tools for learning in a complex world, *California Management Review* 43(4)
- [15] Sterman, J.D. (2002) *Systems thinking and modelling for a complex world*, Massachusetts Institute of Technology, Engineering systems division, esd-wp-2003-01.13-esd
- [16] Engwall, M. (1998) *The project concept(s): On the unit of analysis in the study of project management*, Kluwer, Boston, pp25–35
- [17] Groesser, S. (2012) Dynamische Komplexität ist die große Herausforderung für das Management, *CFO aktuell* 6(2), pp67–72
- [18] Geels, F.W. (2004) From sectoral systems of innovation to socio-technical systems: Insights about dynamics and change from sociology and institutional theory, *Research Policy* 33, pp897–920
- [19] Leete, S. et al. (2013) Investment barriers and incentives for marine renewable energy in the UK: An analysis of investor preferences, *Energy Policy* 60, pp866–875
- [20] Wyatt, S. (2014) Financing marine energy: The role of innovation in reducing risk, 5th International Conference on Ocean Energy, Canada
- [21] Siemens (2014) Siemens says tidal sector too “niche”: MCT put on selling block, www.tidaltoday.com [26/11/2014]
- [22] IEA-OES (2014) Annual Report, available from www.ocean-energy-systems.org [accessed 20/04/2015]
- [23] Teece, D.J. (1986) Profiting from technological innovation, *Research Policy* 15, pp285–305
- [24] Bucher, R. (2013) Strategic risk management in marine energy, 10th European Wave and Tidal Energy Conference, Denmark
- [25] Bucher, R. & Bryden, I. (2014) Overcoming the marine energy pre-profit phase, 2nd Asian Wave and Tidal Energy Conference, Tokyo, Japan
- [26] Bucher, R. & Bryden, I. (2014) Strategic orientation for ocean energy market roll-out, *Journal of Energy Challenges and Mechanics* 1(2), pp1–10
- [27] Groesser, S. (2011) Projects fail because of dynamic complexity, *Projektmanagement aktuell* 22(5), pp15–25
- [28] DNV (2001) Qualification procedures for new technology, Recommended practice, Det Norske Veritas
- [29] Brown, S.L. & Eisenhardt, K.M. (1997) The art of continuous change: Linking complexity theory and time-paced evolution in shifting organizations, *Administrative Science Quarterly* 42(1), pp1–34
- [30] Forrester, J.W. (1971) Counterintuitive behaviour of social systems, *Technology Review*, Vol. 73, No. 3, pp52–68
- [31] Richardson, G.P. & Sterman, J.D. (1996) *Proceedings of the 1996 International System Dynamics Conference*, System Dynamics Society
- [32] Wu, J.-H., Huang, Y.-L. & Liu, C.-C. (2011) Effect of floating pricing policy: An application of system dynamics on oil market after liberalisation, *Energy Policy* 39, pp4235–4252
- [33] Forrester, J.W. (1961) *Industrial dynamics*, The MIT Press, Massachusetts Institute of Technology, Cambridge, USA
- [34] Yim, N.-H., Kim, S.-H., Kim, H.-W. & Kwahk, K.-Y. (2004) Knowledge based decision making on higher level strategic concerns: System dynamics approach, *Expert Systems with Applications* 27, pp143–158
- [35] Groesser, S. (2011) Measurement of dynamic complexity, *Proceedings of the 29th International System Dynamics Conference*, Washington DC, USA
- [36] Schwenke, M. & Groesser, S. (2014) *Modellbasiertes Management für dynamische Problemstellungen*, Duncker & Humblot, Berlin, pp139–150
- [37] Senge, P. & Sterman, J.D. (1992) Systems thinking and organizational learning, *European Journal of Operational Research* 59(1), pp137–150
- [38] Diehl, E. & Sterman, J.D. (1995) Effects of feedback complexity on dynamic decision-making, *Organizational Behavior and Human Decision Processes* 62(2), pp198–215
- [39] Sterman, J.D. (1989) Modelling managerial behaviour, *Organizational Behavior and Human Decision Processes* 43(3), pp301–335
- [40] Saynisch, M. (2010) Mastering complexity and changes in projects, economy, and society via PM-2, *Project Management Journal* 41(5), pp4–20
- [41] Remington, K. (2011) *Leading complex projects: Comprehend complexity*, Gower Publishing, ISBN 978-1409419051
- [42] Bucher, R. & Jeffrey, H. (2014) Creation of investor confidence: The top-level drivers for reaching maturity, 5th International Conference on Ocean Energy, Canada



Law of inertia and the primal energy in the cellular automaton universe

元胞自动机宇宙内的惯性定律和原始能源

Simon Berkovich

Department of Computer Science, The George Washington University, Washington, DC 20052, USA

berkov@gwu.edu

Accepted for publication on 20th October 2015

Abstract - In the Cellular Automaton Universe material objects acquire the property of inertia automatically as relocating formations driven by the underlying clocking mechanism. In this way, the core effect of inertia reveals the hidden source of all motions in the physical world. The corresponding energy can be extracted by a process of recurring transformations of material configurations producing a sort of parametric amplification.

Keywords - Law of inertia, Parametric Amplification, Cellular Automaton Universe, Clean energy

I. INTRODUCTION

The world faces crisis of global sustainability with complicated challenges on a scale never before seen in human history. Those include various threats to ecology, dearth of resources - primarily, energy, and serious biomedicine problems. Unfortunately, the worldview of contemporary science does not provide sufficient means to confront these urgent existential challenges for the humanity. The tremendous achievements in modern life are the results of advancements in technology rather than a breakthrough in science. Technology can thrive on incorrect science; and even more, it can provide inspirations to new theories.. Thus, the Industrial Revolution was formed by the invention of the steam engine considering heat as a caloric liquid before the discoveries of thermodynamics and the kinetic theory of matter. As Lord Kelvin said, "The steam engine has given more to science than science has given to the steam engine". Nowadays, we witness all-encompassing Information Revolution, which allows to effectively portray the organization of the physical Universe and the Life on Earth as a technological marvel of the "Internet of Things" arising in the framework of a Cellular Automaton

model [1] Beyond the 'Big Data' environment for information control as described in [2], this contraption may provide an abundant supply of energy needed for actuation (see [3,4]). The energy agitating the physical Universes comes ultimately from the clocking activities of the underlying Cellular Automaton infrastructure. In our current view, these clocking activities reveal themselves at the physical level not directly, but through the property of inertia. In this paper, we will discuss how the extraction of clean and abundant energy from the workings of the inertia in the Cellular Automaton Universe could be effectually organized.

II. THE CELLULAR AUTOMATON MODEL OF THE UNIVERSE

2.1. THE ULTIMATE DRIVE OF THE MATERIAL PROCESSES

"It is important to realize that in physics today, we have no knowledge of what energy is" [5]. In our understanding, energy is the ability to move matter. Energy appears in different forms in physical chemical, and biological processes, and is evaluated by the effects it has on matter. The conservation law states: energy cannot come from nowhere, nor disappear into nothingness; the total amount of energy in co-measurable terms remains constant. A sarcastic depiction of this law: "Energy is never created nor destroyed, it simply goes from one *formula* to another" presents an ironic truth.

Traditional physics takes the property of inertia for granted, i.e. it does not consider that realization of uniform motion is associated with a continuous consumption of energy. Actually, the uniform motion of the material formations in the Cellular Automaton Universe appears free if one neglects the impetuses

of the Cellular Automaton clocking. However, in the general balance of the law of conservation of energy, these impetuses have to be taken into account with some corresponding conversion coefficient, similarly to Joule's balancing of heat with mechanical energy. In other words, the hidden driving force of the Cellular Automaton mechanism goes on par with all other forms of energy. Moreover, it is the fundamental cause of all motions, and thus, the innermost source of all energy in the Universe.

In fact, motion without an enduring motive power seems perplexing. Thus, Aristotle believed that objects are moved only as they were pushed, and any given motion is reduced to a certain Prime Mover. A notorious problem for this point of view was why arrows shot from a bow continued to fly. A concrete explanation for the flying arrow problem was proposed, assuming; for example, that the arrow creates behind it a vacuum, into which air rushed and applied a force to the back of the arrow. Nowadays, a similar explanation is considered for the paradoxical NASA Warp drive effect [6,7] employing hypothetical pushing from the curved space time and quantum vacuum, as proposed by M. Alcubierre. [8].

Recent NASA experiments have allegedly demonstrated a new propulsion technology; it requires no propellant and by electromagnetic radiation in a resonant cavity generates a small amount of thrust that is not attributable to any classical electromagnetic phenomenon. Thrust that was produced was apparently just above the margin of error, anywhere between 50 and 70 micronewtons, with a reported error bar between 15 and 30 micronewtons. The effect is incredible, like a famous adventure of Baron Münchhausen who pulls himself out of a mire by his own hair, since it violates the principle of momentum conservation stating that the total linear momentum of an isolated system remains constant regardless of changes within the system. This follows from Newton's second and third laws.

What requires some revision is Newton's first law, the "Law of inertia", stating that every object will remain at rest or in uniform motion in a straight line unless an external force is applied to it. According to scrupulous Poincaré analysis, the notion of inertia is neither an a priori truth nor an experimental fact; it is rather a supposition that "the movements of all material molecules of the universe depend on the differential equations of the second order"[9]. Also, a crucial support for our Cellular Automaton approach gives Maxwell's consideration that: the law of inertia, would be without meaning, unless we admit the possibility of defining absolute rest and absolute velocity [10].

2.2 THE CONCEPT OF CELLULAR AUTOMATON ETHER INFRASTRUCTURE (CAETERIS)

A cellular automaton is a grid of nodes whose states are transformed in discrete steps depending on the states of the surrounding neighbors. The idea of representing the physical world with cellular automata was conceived by K. Zuse and E. Fredkin (see [11, 12] Potentials of the cellular automata for the representation of the physical world are best envisioned with the well known Conway's "Game of Life", where certain "patterns" present stable relocating configurations. Thus, it is tempting to find a Rule producing a collection of stable relocating configurations, which could be identified with the elementary constituents of matter. The cellular automaton model for the physical Universe is a high-tech resurrection of the classical concept of ether where motion of the material formations is performed by reconfigurations over the medium rather than by passing through it. Notably, such a construction avoids confrontation with the postulate of relativity and induces the property of inertia.

Realization of the cellular automaton model of the Universe involves two major concerns. First: trying to find a cellular automaton Rule that can produce the complex behavior of physical objects seems impossible. Second: it is not clear whether local transformations can account for the apparent non-locality of the Universe. Indeed, to rely on brute force search for the Rule is hopeless. But starting with the firm design requirements rather than guessing upon the desired outputs one immediately recognizes the necessity for a distributed mechanism of clocks synchronization, which has to be robust and fault-tolerant.

The indispensable design requirement for such synchronization removes any arbitrariness in the choice of the primitive Rule. The cellular automaton mechanism of Nature must contain a grid of mutually synchronizing circular counters; the system is characterized by a distribution of the phases θ ($0 < \theta < 2\pi$) defining the states of the counters. Astoundingly, but this approach solves the problem: It turns out that the whole richness of the physical world condenses in a plain sentence: "All physical phenomena are different aspects of the high-level description of distributed processes of mutual synchronization in a network of digital clocks" [13]. The developed model was named CAETERIS (Cellular Automaton EThER InfraStructure). Workings of this model have been presented in several publications starting [14], in many various aspects they are described in [15-19]. For the purpose of our paper, we will concentrate here mostly on the synchro activities of the model producing basic material formations (Fig.1)

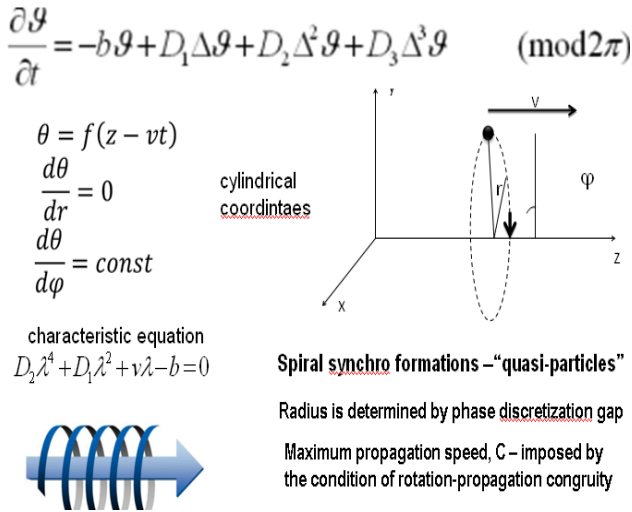


Fig.1 Traveling wave helicoidal solutions

The given equation of synchronization includes a non-linearity factor - a restriction from below on the spatial derivative determined by the realization of fault-tolerance. The collection of helicoidal traveling wave solutions exactly correspond to the spectrum of the stable elementary particles of matter (Fig. 2.)

| Type of kernel | PHASE DEPENDENCES along the generatrix | PROPAGATION SPEED | |
|--|--|-------------------------|---|
| | | intermediate $V < C$ | maximum $V = C$ |
| Real exponents increasing decreasing $M_e \ll M_p$ | θ $f(z) = A_1 e^{kz}$ $f(z) = A_2 e^{-kz}$ | Proton Electron | Electro-Magnetic Field Photon |
| Imaginary exponents Neutrino masses are smaller $M_{\nu e} < M_{\nu \mu} < M_{\nu \tau}$ | θ $f(z) = A_1 \cos \sqrt{\frac{D_1}{D_2}} z$ $f(z) = A_2 \cos \sqrt{\frac{D_2}{D_3}} z$ $f(z) = A_3 \cos \sqrt{\frac{D_3}{D_1}} z$ | | Neutrinos electron muon tauton |

Fig.2 Spectrum of stable elementary particles

Both fundamental solutions of increasing exponent, for the proton: $\exp(\mathbf{b}/\mathbf{v}) \cdot \mathbf{s}$ and decreasing exponent; for the electron: $\exp(-\mathbf{v}/D_1) \cdot \mathbf{s}$; depend on the velocity \mathbf{v} in the same way. Namely with the increase of \mathbf{v} , both functions along the generatrix - \mathbf{s} become smaller; this implies that protons and electrons reactions to the presumed manipulations for energy extractions will be coordinated.

As to the neutron (Fig. 3), it is a composite semi-stable particle with half-life of about 15 min.. The generatrix function of the neutron presents a linear combination of the indicated fundamental exponential solutions for the electron and the proton connected with a sinusoidal segment of neutrino. These components are weakly hold jointly at generatrix. The neutron together with other less stable composite particles is presented in Fig.3.

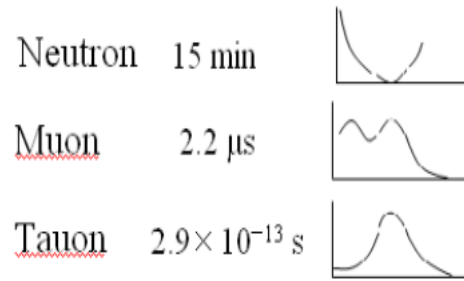


Fig.3. Semi-stable composite particles

The neutron decays as its generatrix splits into joined components: $\mathbf{n} = \mathbf{p}^+ + \mathbf{e}^- + \mathbf{\nu}$. Neutron is a proton trailed by neutrino and electron, it has a greater mass than proton. In a similar way can be described the radioactive decays by weak interactions of less stable particles - muons and taons. Muon is an electron trailed by neutrino, it has properties similar to those of electrons, but its mass is much greater; taon is an electron trailed by neutrino and proton, it has higher instability and some hadronic features due to the influence of a rear increasing exponent.

The helicoidal synchro formations of the CAETERIS model actually exhibit the basic properties of the fundamental physical phenomena. Besides the discussed law of inertia those include: an upper bound on the propagation speed – the speed of light, antimatter as dual solutions having an opposite sense of rotation, slight asymmetry between matter and antimatter - the enigmatic prevalence of matter, which arises from the necessity for an arbitration protocol, and much more.

Besides traveling wave helicoidal “synchro formations” creating the basic componentry of the material world the CAETERIS model includes an operational background of very fast spreading diffusional solutions. The origin of these solutions is associated with the paradox of instantaneous impact in parabolic equations. This paradox shows that representation of spreading diffusion by

parabolic equations is a mathematical idealization, behind which there should be some very fast propagating wave mechanism. The pop-up instantaneous impact produces gravitation with amplification in cosmological scale [20]. This could resolve the conundrum of dark matter, see article [21], worrying “How long can we keep on looking for dark matter?”

The opinion that “the action-at-the-distance” is inadmissible from the philosophical standpoint is flawed. There is absolutely nothing outlandish in having a system with two types of processes developing in substantially different time scales. In fact, it is a typical situation for relatively slow material systems under drastically faster information control. The appearing effects of “nonlocality” are decisively involved in the organization of the Holographic Universe. . This holographic mechanism reveals itself in the strangeness of quantum mechanics behavior, and in the intricacy of biological information processing [2,17].

2.3 EXTRACTING “INERTIA” ENERGY FROM CELLULAR ATOMATON ACTIVITIES

As long as Cellular Automaton mechanism produces freely propagating material formations as exemplified in Fig. 1 and 2 no deviations from the law of inertia, and hence no manifestation of force, appears at the level of the physical world. Therefore, to enjoy the Cellular Automaton energy it is necessary to diverge material formations from the indicated traveling wave conditions. In a simplest way this can be achieved by deflecting the axis of a helicoidal kernel from the propagation direction. (Fig. 4)

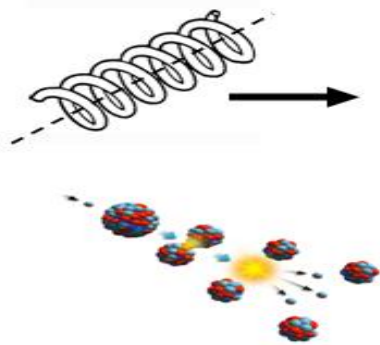


Fig.4. Extracting “inertia” energy by distortions of canonical formations for uniform motion: from slight deflections of a given direction to major disarrangements in atomic fission

To reinstate canonical solutions the cellular automaton mechanism has to employ supplementary activities. At the level of the physical world reinstallations of a distorted

material object to a required pattern appear as a result of an action of a force, i.e. as utilization of some energy. Presumably, the observed NASA Warp Drive effect could occur in such circumstances as soon as the utilized electromagnetic radiation scatters atoms directions. Cellular Automaton transformations turning them back to a proper way would be felt as a small thrust. Similarly, independent material bodies due to random atomic fluctuations may also experience some miniscule spontaneous pushes questioning the exactness of the law of inertia.

For a massive extraction of the primal Cellular Automaton energy the applied transformations of matter have to be radical. The Fig.4 illustration presents a palpable example of the atomic energy when the transformations of the involved matter are substantial: one big nucleus fissions into many different fragments - two smaller nuclei and additional particles to maintain the process. Thus, to return these deeply disfigured fragments to canonical Cellular Automaton matter would take a lot of efforts resulting in the release of vast energy. In case of extremely violent particle collisions the created debris may not always be reconfigurable back to viable material formations, and such situation may show up a defiance to basic conservation principles.

An intermediate situation presents the unusual “excess heat” effect associated with the mechanism of Low Energy Nuclear Reactions (LENR). This widely considered mechanism raises a number of concerns since it confronts the established body of knowledge in nuclear physics. In our view; LENR devices get their energy from the Cellular Automaton inertia through relatively milder material reconfigurations. These reconfigurations may just involve splitting the generatrix function; as shown in Fig.3; this is associated with radioactive decays due to weak interactions. According to our interpretation, of the “excess heat” effect, its outputs are sensitive to the direction of inertial propagation, i.e. to the changes of the absolute positioning of the apparatus. This circumstance can be used to withstand the serious problem of LENR instability.

III. CONCLUSION

Apart from the exotic idea of the Cellular Automata, the presented interpretation of inertia leads to a new conceptual scheme for the interpretation of classical mechanics. Material objects are uniformly propagating formations whose relative interactions are described with respect to the frame of reference where the motion by inertia occurs. In the Cellular Automaton Universe, the hidden energy of inertia comes out as a real physical energy when canonical cellular automaton formations of material objects are disrupted.. The clocking efforts trying to return the distorted material formations to a canonical form are perceived as a force applied to the material object. According to considered Poincaré deliberations upon inertia [9], such a process should be described by second order differential equations elucidating Newton’s Second Law of Motion:: $\mathbf{F} = \mathbf{m} \cdot (\mathbf{d}^2\mathbf{x}/\mathbf{dt}^2) = \mathbf{m} \cdot \mathbf{a}$, along with the additive characterization of

the mass expounding its seemingly careless ‘circular’ definition as a product of density by volume. In a non-inertial frame of reference the cellular automaton compulsion to uniform motion may be interpreted as a “fictitious” force, like in Coriolis effect. In our interpretation, the Foucault pendulum extracts its rotational energy from the Cellular Automaton mechanism, not from the impacts of the Earth, as becomes apparent in the idealized case of a frictionless pivot. Variations of atom alignments in macromolecule structures can be used to accumulate the Cellular Automaton energy in the form of chemical energy for muscles operations.

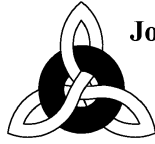
Consideration of the Cellular Automaton mechanical implications can be extended to electromagnetism. It is a well-recognized physical fact that energy from an electric power station to a customer is not transferred through electric lines, but rather enters the customer wires from outside according to the Poynting vector of the electromagnetic field. The absolute orientation of the wire with respect to the Cellular Automaton propagation may affect the electrical resistivity. This may produce an anisotropy in the exploding wires phenomenon. In stationary situations the suspected anisotropy in electrical wires may be revealed if a miniscule heating from inertia energy could cause a noticeable impact on the resistivity, e.g. for high purity superconductors in the intermediate state. Thus, in [22] there was observed a hysteresis bump on a transition from normal to superconductive state, so for a different orientation of the sample attracting to it less heat energy from the inertia relocations, this bump may be diminished.

This inertia energy is readily available everywhere on Earth. The presented theory elucidates many paradoxical situations in Nature when a source of operational energy is difficult to identify (see [4]), in particular, for biology (motility), meteorology (turbulence), and geophysics (ball lightning). Besides its academic significance, the given theory is of obvious practical value for all energy production technologies, primarily for the explanation of LENR, specifically addressing its complication with instability.

REFERENCES

- [1] Simon Berkovich, “Physical world as an Internet of Things”, COM.Geo’11, Proceedings of the 2nd International Conference on Computing for Geospatial Research and Application, Article No. 66, **ACM**, New York, NY, 2011.
- [2] Simon Berkovich “Formation of Artificial and Natural Intelligence in Big Data Environment”, *Springer, Network Science and Cybersecurity, Advances in Information Security*, Volume 55, pp. 189-203, 2014.
- [3] Simon Berkovich, “Generation of clean energy by applying parametric resonance to quantum nonlocality clocking”, *Nanotech* 2011, Vol. 1, pp.771-774.
- [4] Sustainability Problems and a Novelty in the Concept of Energy”, *Springer, Network Science and Cybersecurity, Advances in Information Security*, V.61, pp.119-133, 2014.
- [5] Richard Feynman, “Six Easy Pieces”, Addison-Wesley Publishing Company, 1996.
- [6] Elizabeth Howell, No Warp Drive Here: NASA Downplays ‘Impossible’ EM Drive Space Engine http://www.space.com/contact_author.php?a=Uld4cGVtRmlaWFJvSUVodmQyVnNiQ3BqYjIIMFlXTjBLaIFxWld4cGVtRmlaWFJvYUc5M1pXeHNMbU5o
- [7] Brady, David, White, Harold G, March, Paul, Lawrence, James T, Davies, Frank J., “Anomalous Thrust Production from an RF Test Device Measured on a Low-Thrust Torsion Pendulum” <http://ntrs.nasa.gov/search.jsp?R=20140006052>
- [8] Alcubierre drive, Wikipedia, https://en.wikipedia.org/wiki/Alcubierre_drive
- [9] H. Poincaré, ‘Science and Hypothesis’, Dover Publications, New York, 1952.
- [10] James Clerk Maxwell, “Matter and motion” Dover Publications, New York, 1991.
- [11] Konrad Zuse, “The Computing Universe”, *International Journal of Theoretical Physics*, 21, Nos. 6/7, pp. 589-600, 1982.
- [12] David L. Chandler, “In the beginning was the Rule”, *New Scientist*, issue 2400, page 32, 21 June 2003.
- [13] S. Berkovich, “Spacetime and matter in cellular automaton framework”, *Nuclear Physics B*, 6, pp. 452-454, 1989.
- [14] S. Berkovich, “Mutual Synchronization in a Network of Digital Clocks as the Key Cellular Automaton Mechanism of Nature. Computational Model of Fundamental Physics”, Synopsis, Rockville, MD, 1986, ISBN 0-9613945-1-X.
- [15] S. Berkovich, "Cellular automaton modeling of the phenomena of fundamental physics", Proceedings of the 19th Annual Pittsburgh Conference on Modeling and Simulation, vol. 19, Part 2, pp. 895-906, 1988.
- [16] S.Y. Berkovich, "Cellular Automaton as a Model of Reality: Search for New Representations of Physical and Informational Processes", Moscow University Press, Moscow, Russia, 1993 (translated into Russian); http://www.chronos.msu.ru/old/RREPORTS/berkovich_avtomaty.pdf
- [17] S. Berkovich and Hanan Al-Shargi, “Constructive Approach to Fundamental Science”, *University Publishers*, San Diego, CA, 2010.
- [18] Jingzheng Qin, “Elementary Particles of Matter in a Cellular Automaton Framework”, GWU, Master thesis, May 2012, <http://pqdtopen.proquest.com/#abstract?dispub=1510409>
- [19] S. Y. Berkovich, “On the “barcode” functionality of the DNA, or The phenomenon of Life in the physical Universe”, Dorrance Publishing Co, Pittsburgh, PA, 2003.

- [20] S. Berkovich, "An operational mechanism featuring gravity amplification", *Hadronic Journal*, Vol. 35, 2, pp. 175-208, 2012 ISSN:[0162-5519](#).
- [21] "No end in sight", *New Scientist*, issue 3026, page 5, 20 June, 2015.
- [22] Berkovich S. Ya., Kan Ya. S., Rabukhin L. B, "Concerning the destruction of superconductivity with direct current". *JETP Letters*, Volume 1, Issue 4, page 108 (1965).



On the optimisation of a cylinder/plate configuration with the aim to improve the energy harvesting of vortex induced vibrations

用以提高涡激振动能量收集之气缸/板结构优化

Till Biedermann*, Frank Kameier, Robert Heinze

Institute of Sound and Vibration Engineering ISAVE, University of Applied Sciences Duesseldorf, Duesseldorf 40474, Germany

till.biedermann@hs-duesseldorf.de

Accepted for publication on 12th October 2015

Abstract - With the objective of energy harvesting by use of vortex induced vibrations on a cylinder/plate configuration different approaches for maximising the amplitude of oscillation modes were pursued. By investigating the sound emissions of a small-scale cylinder/plate setup, a maximisation of the vortex-induced wall-forces on a rigidly mounted cylinder can be described. The surface-forces induce pressure fluctuations that propagate with the speed of sound and cause dipole shaped Aeolian tones. Thus, the present wall-forces of the cylinder directly correlate with the acoustic phenomena. Regression functions were formulated to describe the effect of the investigated parameters Reynolds number, turbulence intensity, plate length, plate thickness and vertical displacement between plate and cylinder, quantitatively for each analysed response variable. An optimal set of parameters can be defined with respect to the given boundary conditions that guarantees high surface-forces on the cylinder and consequently leads to an improved system.

Keywords - energy harvesting, vortex induced vibrations, aeroacoustics, cylinder/plate configuration

I. INTRODUCTION

Given an elastically mounted cylinder in a steady flow, when exceeding a critical Reynolds number, vortices start to separate from the cylindrical surface. If the vortex shedding frequency (f_{VSF}), described by the Strouhal law in Eq. (1), equals the eigenfrequency (f_{Eigen}) of the cylinder-spring-system, a transition to an excited mode takes place and the cylinder starts oscillating.

$$f_{Eigen} [Hz] = f_{VSF} = Sr/d_{cyl} \cdot U_0 \tag{1}$$

Where Sr is the Strouhal number, d_{cyl} the cylinder diameter and U_0 the incoming flow velocity. Use of the idle strokes of the cylinder, caused by vortex-induced vibrations (VIV), enables the harvesting of energy, Fig. 1. Especially energy-rich water flows offer great possibilities and good efficiencies for this new technological approach, even at low-speed conditions ($U_0 \leq 3$ m/s). Studies during the last decade promise good results and a huge range of applications such as wastewater flows or applications at riverbeds and beneath the floating platforms of offshore wind energy parks. One key issue of this system, when implementing in environmental applications, is the dependency of the system efficiency on a constant flow at a certain velocity, able to provide the matching vortex shedding frequency to the eigenfrequency of the system in order to guarantee the excitement.

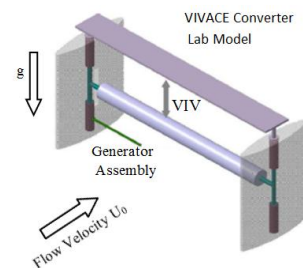


Fig.1, Energy harvesting with cylinder in self-excitement. Technology of vortex induced vibrations for aquatic clean energy VIVACE [1].

Recent investigations have revealed that placing a rigidly mounted geometrical body such as a square cylinder or a plate in the wake of the cylinder may stabilise the system behaviour

over a wide range of incoming flow rates and enables the VIV technology to be used at varying flow conditions. With reaching an excited mode of the cylinder-spring-system the vortex shedding frequency ‘locks-in’ to the eigenfrequency of the dynamic system. Further increase of the flow velocity does not lead to a dropout of the excited condition. Furthermore, the oscillation amplitudes increase significantly with an attached body in the cylinder wake.

This leads to a higher energy harvesting capability per stroke. An alteration of the system behaviour takes place by the reduction of the vortex shedding frequency caused by the body in the cylinder wake. The resulting amplitudes are highly sensitive to the gap between both bodies and the dimensions of the downstream body itself. A small non-dimensional gap of g/d (i.e. $g/d = 0.5$), where d is the cylinder diameter and g the absolute distance, reveals the highest amplitudes, Fig. 2. Up to now, the aerodynamic principles, which secure the reinforcement of the oscillation amplitude and stabilisation of the excitation mode, have been the topic of only few investigations.

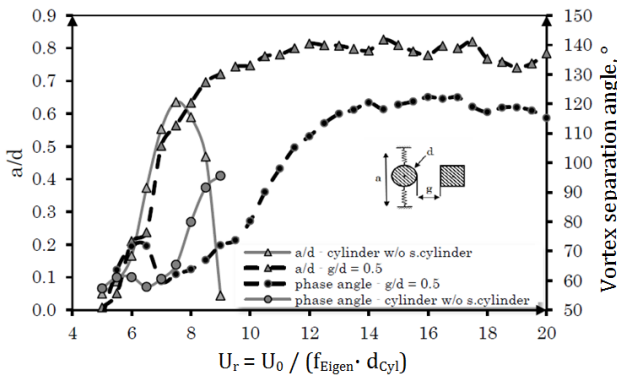


Fig.2, Experimental results of Particle Image Velocimetry (PIV) study. Trend of vibration amplitude (a/d) and vortex separation angle as function of the reduced flow velocity U_r with flow velocity U_0 , cylinder-spring eigenfrequency f_{Eigen} and cylinder diameter d_{Cyl} [3].

The lift forces on the cylinder wall, which are highly dependent on the separating angles of the vortices (Fig. 2), are causal for the oscillating movement. Low separation angles result in longer energisation durations of the vortices and thus higher lift forces. The wake-body represents a damping device and thus has an upstream effect on the separation process of the laminar boundary layer on the cylinder. Recapitulatory, it can be said that the resulting lift forces and thus the efficiency of this cylinder/plate configuration depends on a variety of aerodynamic and geometrical parameters.

The aim of the current study is to deepen the understanding of the acting principles of a cylinder/plate configuration in a steady flow and to provide an informative basis on how to design geometrically beneficial wake-bodies as well as how to manipulate aerodynamic parameters in order to receive the most efficient system. Knowledge on the effect of different geometric and aerodynamic parameters might contribute to an optimal design and consequently to an improvement of the energy efficiency and stability of the oscillating system. For

this purpose, the reduction of the originally discussed system from an elastically mounted to a rigidly mounted cylinder simplifies the system and reduces the experimental uncertainties in order to gain knowledge on basic acting principles on the cylinder wall. Moreover, numerical flow simulations and the analysis of the acoustic emissions of a rigidly mounted cylinder in a flow offer a simple and accurate method to characterise the acting forces on the cylinder wall due to separating vortices [7].

The alternately separating vortices that constitute the cause of the lift forces act as a pressure dipole, which induces pressure differences into the surrounding fluid of the cylinder, Fig. 3. These pressure differences propagate at sound velocity and cause Aeolian tones with a peak frequency equal to the vortex shedding frequency (f_{VSF}), Eq. (2).

$$f_{Aeolian}[Hz] = f_{VSF} = Sr/d_{Cyl} \cdot U_0 \tag{2}$$

Besides the VSF, the acoustic measurements provide further information such as the sound pressure level (SPL), which indicates the magnitude of the acting surface forces, Eq. (3). The vortex shedding frequency as well as the resulting sound pressure level are functions of the distance between cylinder and plate.

$$SPL [dB] = 10 \cdot \lg \left(\frac{p_{rms}^2}{p_0^2} \right), \quad p_0 = 2 \cdot 10^{-5} Pa \tag{3}$$

Where p_{rms} is the root-mean-square value of the sound pressure and p_0 the reference value. The acoustic treatment is advantageous compared to the measurement of wall-forces due to its simplicity and the possibility to carry out measurements with disturbing quantities reduced to its minimum. Furthermore, a variety of response variables can be analysed by simultaneously keeping the experimental volume manageable.

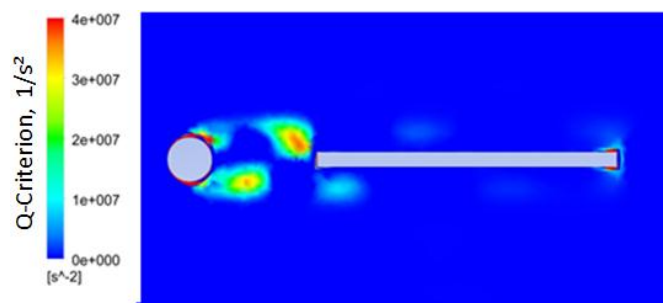


Fig.3, Visualised Q-Criterion. Numerical analysis of a rigidly mounted small-scale cylinder/plate configuration via ANSYS CFD [8].

To enable extensive acoustic investigations of the cylinder/plate configuration, a scaling to small cylinder / plate dimensions has been necessary in order to prevent 3-D effects as well as to treat the configuration in the anechoic chamber that is restricted by limited dimensions of the open jet wind tunnel at the ISAVE.

II. EXPERIMENTAL SETUP

2.1. TEST RIG & MEASUREMENT FACILITIES

The conduction of the free field measurements of the radiated cylinder/plate interaction noise took place in the open jet wind tunnel in the ISAVE, situated in a 4 m x 6 m anechoic chamber. The nozzle exit is a quadratic section with a lateral length of 0.15 m. The low speed wind tunnel can achieve turbulence intensities as low as 1.5% and Mach numbers as high as 0.12 while maintaining a very low background noise at frequencies above 50 Hz.

A cylinder with $d = 3$ mm was aligned horizontally at the nozzle exit of the low speed open jet wind tunnel. The cylinder under investigation was fitted with endplates, four times the cylinder diameter and Scruton helices on both sides' outer sections to avoid three-dimensional effects as well as to suppress vortex shedding aside from the test region.

A plate with varying geometric dimensions was placed in the wake of the cylinder. Starting at a non-dimensional distance between cylinder and plate of $g/d = 1.5$ the plate was traversed in streamwise direction up to a distance of $g/d = 12$ at a traversing speed of $0.4 \text{ mm}\cdot\text{s}^{-1}$.

The use of a Matlab®-controlled traversing system with minimum steps of 0.1 mm allowed the continuous adjustment of the distance between cylinder and plate. A 1/4" ICP condenser microphone was rigid-placed at a distance of 100 mm beneath the cylinder to measure the emitted narrow band spectrum of the dipole noise while altering the cylinder/plate gap. Data acquisition took place by use of Mueller BBM-VAS-PAK acoustic software and a 24-channel frontend at sampling rates of 16 kHz and a resulting frequency resolution of 4 Hz while applying Hanning windowing and overlapping of 36%.

Preliminary investigations into the influence of a variety of different parameters on the noise radiation revealed a set of five characteristic parameters, Table 1. Extensive hot wire measurements were necessary to ensure an accurate description of the turbulence intensity Tu and the open jet flow velocity U_0 . The mathematical description of the influence of the parameters on response variables still to be defined, took place by use of a statistical approach. The use of non-dimensional parameters allows a comparison to large-scale applications in future work. The flow speed range under investigation is between 12 m/s and 29 m/s or Reynolds numbers based on the cylinder diameter of 2200 to 5500 respectively. The turbulence intensity of the incoming flow is a flow characteristic considered to have an outstanding relevance. The use of turbulence grids results in a large range of turbulence intensities between 2.4% and 7.8%. The turbulence intensity is considered isotropic.

TABLE 1, NON-DIMENSIONAL PARAMETERS, BASED ON THE CYLINDER DIAMETER $D = 3$ MM.

| Parameter | Unit | Min | Max |
|--------------------------|------|------|------|
| Re | [--] | 2252 | 5520 |
| Tu | [%] | 2.4 | 7.8 |
| l_{Plate} | [--] | 0.67 | 4.0 |
| d_{Plate} | [--] | 0.17 | 1.33 |
| $h_0, \text{Displacem.}$ | [--] | -0.5 | 0.5 |

The definition of plate length and plate thickness bases on the cylinder diameter to provide comparable values to large-scale applications. The vertical displacement between cylinder and plate defines the vertical distance between the centrelines of both bodies. The values of investigation differ in a non-dimensional range of -0.5 to 0.5 based on the cylinder diameter.

2.2. EXPERIMENTAL METHODOLOGY

According to the n-permutation, the measurement of the experimental system by varying the parameters (k) of interest in five levels each (n), results in a number of 3125 measurement points, Eq. (4). Applying the statistical approach of Design of Experiments (DoE) reduces the experimental volume and the number of trials to measure (MT) ads up to 43 without relevant loss of information on the system behaviour, Eq. (5).

$$MT_{n-per} = n^k = 3125 \tag{4}$$

$$MT_{DoE} = 2^k + 2 \cdot k + 1 = 43 \tag{5}$$

The Design of Experiments methodology is based on the definition of an experimental space, consisting of a full factorial core, star points that label the upper and lower experimental boundaries and a central point, defined as the experimental adjustment where all parameters are on their intermediary values [2], Fig. 4. Based on this experimental composition of the DoE methodology, the analytical statistics gathers on the population from a subset.

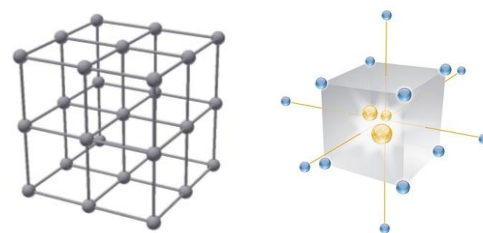


Fig.4, Comparison of a classical grid measurement design (left) and a central composite design with pseudo-orthogonal and rotatable features (right) [5].

Due to its structured composition the presented methodology offers, apart from the remarkable reduction of measurement points, the definition of regression function that describes the response variable (RV) by means of all influencing parameters (IP) in first and second order as well as

interdependencies between the influencing parameters, Eq. (6). Analyses of the statistical significance allow the elimination of parameters with impacts on the response variable smaller than the statistical spread.

$$RV_i = f \left\{ \sum_{j=1}^n \left((IP_j + IP_j^2) + \sum_{k=1}^n (IP_j IP_{j+k}) \right) \right\} \begin{cases} i = 1..4 \\ j = 1..5 \\ k = 1..4 \end{cases} \quad (6)$$

The execution of the experiment had to be divided into three days and the utilisation of *blocking* compensated potential perturbations. The trials of the strategically planned experiment were performed in a randomised order within each block. A randomised sequence secures the reduction or elimination of unknown and uncontrollable disturbing quantities.

III. EXPERIMENTAL RESULTS

Analysing the measured narrow band spectrum while altering the gap between plate and cylinder, results in the definition of different response variables that are evaluated in dependence on the investigated parameters, Table 2.

The first response variable is the non-dimensional distance between cylinder and plate where the sound pressure level starts to rise significantly and Aeolian tones are observed. This variable defines the start of the vortex shedding process at the cylinder ($g/d_{Start,SPE}$). Secondly, the vortex shedding frequency is of high interest to gain knowledge on its system behaviour as a function of the investigated parameters. Division of the VSF by the VSF of a single cylinder in a flow at the same inflow velocity permits a direct comparison between both systems, with and without attached plate ($f_{VSF,Config}/f_{VSF,Single}$). Third, the maximum overall sound pressure level ($OASPL_{Max}$) provides information on the magnitude of acting forces. Finally, the distance at which the acoustic emissions reduce significantly ($d(g/d)_{Start,Stop}$) is of interest due to its indication as marginal distance where the plate influences the vortex separation process at the cylinder. This response variable is defined as the non-dimensional distance between start and end of the sound pressure enhancement (SPE).

TABLE 2, RESPONSE VARIABLES TO BE ANALYSED VIA DOE METHODOLOGY. NON-DIMENSIONAL PARAMETERS BASED ON CYLINDER DIAMETER $D = 3$ MM.

| Variable | Unit |
|---------------------------------|------|
| $g/d_{Start,SPE}$ | [--] |
| $f_{VSF,Config}/f_{VSF,Single}$ | [--] |
| $OASPL_{Max}$ | [dB] |
| $d(g/d)_{Start,Stop}$ | [--] |

The Reynolds number under investigation causes in combination with the other investigated parameters vortex shedding frequencies $500 \text{ Hz} < f_{VSF} < 2000 \text{ Hz}$, Fig. 5. Attaching the plate in the immediate wake of the cylinder suppresses the separation of vortices and thus impedes the generation of tonal noise. Exceeding a certain cylinder/plate

gap, dependent on the individual parameter levels, the vortex shedding process can take place.

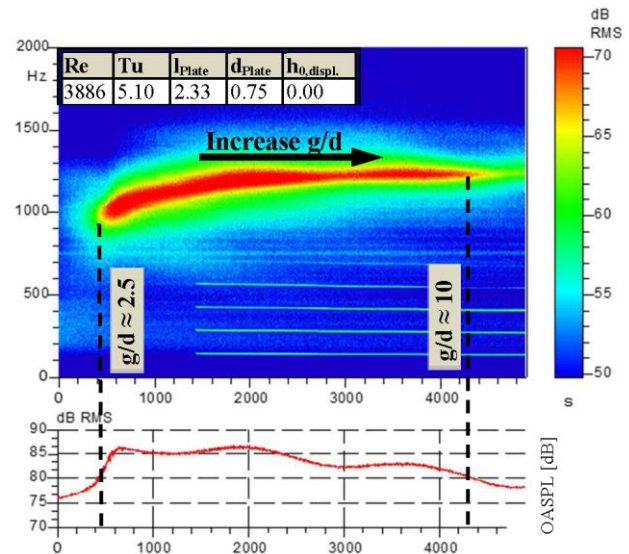


Fig.5, Spectrogram of the SPL over the measurement time, representing the continuous increase of the distance between plate and cylinder. Additional plot of the overall sound pressure level OASPL. Central point trial.

The greater the gap between both geometrical bodies the higher is the VSF until it reaches the VSF, described by the Strouhal law for single cylinders with Strouhal numbers in a range of $0.2 < Sr < 0.21$ and $300 < Re < 10^5$.

The systematic Design of Experiments approach enables to define regression functions that describe the influence of the different parameters on the defined response variables, Table 3. Analyses of the statistical significance of the parameters and elimination of the non-significant terms result in a high accuracy of these functions.

TABLE 3, DEFINITION OF LINEAR COMBINATION FACTORS THAT RESULT IN THE REGRESSION FUNCTIONS TO DESCRIBE THE RESPONSE VARIABLES.

| $g/d_{Start,SPE}$ | f_{Config}/f_{Single} | $OASPL_{Max}$ | $d(SPL)_{Max}$ |
|---|---|--|---|
| [--] | [--] | [dB] | [--] |
| -3.69E0 | 1.48E0 | 6.5E1 | 1.43E1 |
| 1.75E-3·Re | -8.39E-5·Re | 8.86E-3·Re | 1.35E-3·Re |
| -9.57E-8·Re ² | -7.72E-2·Tu | -7.08E-7·Re ² | -5.45E-1·Tu |
| 7.45E-1·Tu | 2.36E-3·Tu ² | -4.36E0·Tu | -3.18E0·l _{Plate} |
| 4.81E-1·l _{Plate} | -8.56E-2·l _{Plate} ² | 1.6E-1·Tu ² | -5.54E0·d _{Plate} |
| -4.89E-2·l _{Plate} ² | 1.66E-2·l _{Plate} ² | 2.78E0·l _{Plate} | -4.16E0·h ₀ |
| 2.75E-1·d _{Plate} | -2.28E-1·d _{Plate} | -3.92E-1·l _{Plate} ² | -4.87E0·h ₀ ² |
| 8.92E-1·h ₀ | 7.19E-2·d _{Plate} ² | -9.33E0·d _{Plate} | -3.29E-4·Re·Tu |
| -7.61E-1·h ₀ ² | 1.14E-1·h ₀ ² | 3.56E0·d _{Plate} ² | 5.19E-1·Tu·l _{Plate} |
| -1.90E-4·Re·Tu | 1.2E-5·Re·Tu | 5.84E0·h ₀ ² | 1.63E0·l _{Plate} ·d _{Plate} |
| -4.27E-2·Tu·l _{Plate} | -4.69E-3·l _{Plate} ·h ₀ | 8.34E-4·Re·Tu | 1.38E0·l _{Plate} ·h ₀ |
| -3.13E-1·d _{Plate} ·h ₀ | | | |

Carried out validation experiments in form of several measurements at parameter levels deviant to the ones analysed in the DoE analyses result in a good agreement and high accuracy of the analysed system and regression functions. Hence, the mapping of the obtained findings and dependencies of the influencing parameters to large-scale applications for further validation is approvable.

3.1. PLATE THICKNESS

Variation of the plate thickness results in a significant change of the response variable. Increasing this parameter causes a reduction of the vortex shedding frequency to lower magnitudes following a primarily linear scaling with slight influences of the quadratic term with opposing trend, Fig. 6. The reduction of the vortex shedding frequency (VSF) originates out of the raised flow resistance induced by the plate and indicates an upstream effect. Due to the rise of the flow resistance, the vortex separation angle in the laminar boundary layer decreases and results in a longer vortex energetisation duration, defined as the time duration between the separation of the boundary layer from the cylindrical wall and the final shed of the fully developed vortex. Vortices of high energy induce strong pressure differences and thus emit a high SPL what indicates high surface forces. Further, it leads to the necessity of a higher cylinder/plate gap, correlated to the vortex formation length, to achieve significant tonal noise.

The vortex formation length (VFL) that describes the required streamwise space needed to enable the full development and cut-off-process of the vortices restricts the minimum distance between cylinder and plate.

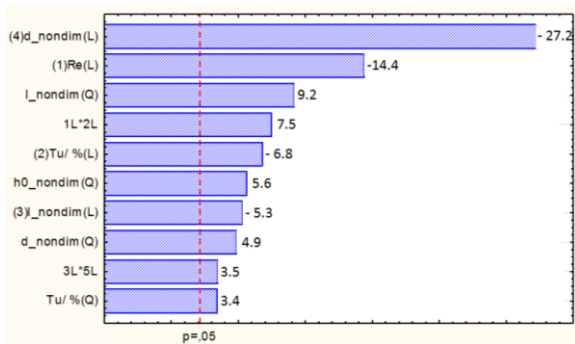


Fig.6, Analyses of the statistical significance of the influencing parameters on the response variable of the VSF. Barrier of statistical significance p = 5 %. Positive values enhance the response variable, negative constrain the response variable.

3.2. PLATE LENGTH

The plate length was found to have a strong influence on the emitted sound pressure level (OASPL_{Max}). A significant rise of the OASPL requires a minimum plate length. Further investigation allocates this dependency as an acoustical phenomenon, not transferable to the aerodynamic system behaviour. At a certain plate length the separated vortices start to impinge on the plate surface and generate, apart from the cylinder surface, a second acoustical source what

consequently leads to a rise of the OASPL, Fig. 7. With regard to the aerodynamic performance of the cylinder/plate configuration, the plate length only shows a negligible influence.

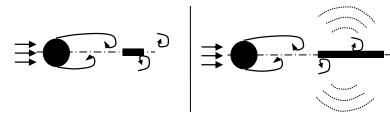


Fig.7, Schematic representation of the aeroacoustic effect of the plate length.

3.3. TURBULENCE INTENSITY

The start of the vortex shedding process and thus the generation of tonal noise highly depends on the turbulence intensity (Tu). The isotropic turbulence intensity (Tu_{iso}), defined as the quotient of standard deviation (U_{rms}) and mean flow velocity (U_{mean}), Eq. (7), forms a perturbation in the approaching flow of the cylinder and affects the linear boundary layer on the cylinder wall.

$$Tu = \frac{\sqrt{u'^2+v'^2+w'^2}}{\sqrt{3*(\bar{u}^2+\bar{v}^2+\bar{w}^2)}} \rightarrow Tu_{iso} = \frac{\sqrt{U'^2}}{U_{mean}} = \frac{U_{rms}}{U_{mean}} \quad (7)$$

Where [u',v',w'] represent the velocity fluctuation and [u,v,w] the mean velocity components of the velocity vector. The perturbation that acts similar to tripping of the flow results in a low separation angle at the cylinder wall. Thus, high turbulence intensities reduce the vortex shedding frequency but result in low cylinder/plate gaps while the shedding process takes place, Fig. 8. The influence on the VSF is mainly of linear character. Analogue to the variation of the plate thickness, low separation angles lead to vortices of higher energy and accordingly to increased wall-forces. Besides the important linear influence of the turbulence on the minimum distance between cylinder and plate, the interdependency between the Reynolds number and the turbulence has an even higher importance. Either very small or high products of turbulence intensity and Reynolds number effect low start distances. The maximum of this interdependency lies in a region of intermediate values (Tu · Re = 19800 ± 5%).

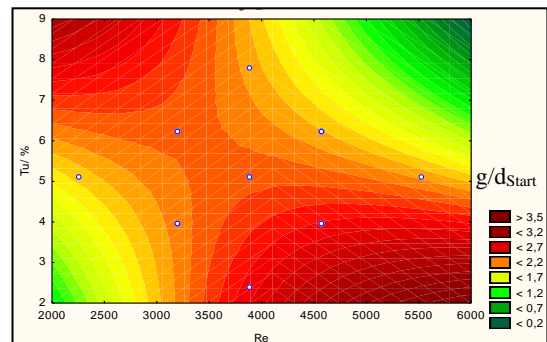


Fig.8, Contour plot, illustrating the influence of Reynolds number and turbulence intensity on the minimum distance between plate and cylinder (g/d_{start}).

This system behaviour has to be analysed very carefully due to the fact, that the definition of the turbulence intensity bases

on the velocity and showed a slight dependence on the velocity magnitude in preliminary investigations.

3.4. VERTICAL DISPLACEMENT

The vertical displacement of the plate with regard to the cylinder position shows an effect on the cylinder/plate gap similar to the one existing at high turbulence intensities. Moreover, a high vertical displacement influences the vortex formation length (VFL) in a quadratic manner, increases the vortex shedding frequency and reduces the cylinder/plate gap at which the plate exerts influence on the separation process at the cylinder.

In comparison to a horizontal aligned plate, in-line with the cylinder, a high vertical displacement enables the vortex separation at significant lower gaps. Due to the reduced blocking ratio on one side of the cylinder, the vortices are separating at early stages and start to interact with the developing vortices on the opposite side of the cylinder [6]. The fact that the plate is displaced and therefore affects the separation process at higher horizontal distances only with minor forces, leads to a VSF similar to the ones of single placed cylinders, described by the Strouhal law, Eq. (2). This phenomenon is in accordance with the influence on the total affecting distance, which is reduced in a quadratic manner the higher the displacement.

3.5. REYNOLDS NUMBER

Aside from the plate thickness, the Reynolds number represents the main influencing parameter on the vortex shedding frequency. According to the Strouhal law, the flow velocity and thus the Reynolds number influences the VSF proportionally with a linear dependency, Eq. (2).

Analysing the non-dimensional response variable of the VSF, divided by the VSF of a single cylinder reveals a decrease of the response variable with increasing Reynolds number. The underlying effect is reasonable. The higher the Reynolds number the higher the VSF in both cases, with and without plate but in case of an attached plate the rise of the VSF turns out to be disproportional and thus the gap between both divided parameters increases with increasing Reynolds number. With regard to the overall sound pressure level ($OASPL_{Max}$), the Reynolds number represents the main influence. With increasing Reynolds number, the absolute VSF rises and more separated vortices per time unit induce pressure differences in the surrounding fluid of the cylinder. Consequently, the $OASPL$ increases.

IV. CONCLUSION

Answers to elementary questions regarding the evaluation of the system response as a function of five parameters were found. The key factors of the investigated process were extracted and levels of the different parameters were analysed to deliver an improved performance. Furthermore, key, main and interaction effects were described accurately.

Key factors that affect the aerodynamic performance and in particular the vortex separation angle in the laminar boundary

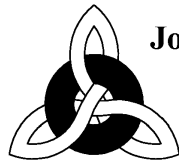
layer on the cylindrical wall of the rigidly mounted cylinder/plate configuration are the Reynolds number (linear), the plate thickness (linear), the vertical displacement (quadratic) and the turbulence intensity (linear plus interdependencies with Reynolds number). The vortex formation length which defines the necessary minimum length to guarantee the development of the vortices (dependent on Reynolds number and turbulence intensity) results in a value at intermediate levels in a range of $g/d \geq 2.2$. This non-dimensional distance defines the lower restriction of the cylinder/plate configuration. The plate length does not represent a significant aerodynamic issue while the plate thickness highly affects the separation angle of the vortices at the cylinder surface. Transferring the reduced rigidly mounted system to the initially regarded oscillating system enables the use of thick but short and aerodynamically optimised plates to increase the resulting oscillation amplitudes by simultaneous reducing the flow resistance of the body. The effects of vertical displacement are expected but in case of an oscillating system of debatable relevance due to the fact that the cylinder strokes are of vertical direction. However, in case of transient oscillation a plate displacement leads to lower cylinder/plate gaps and thus to an increased effect of the plate on the oscillation principle. The implied effect of contracting the affectional distance would be a disadvantage without consequence in case of an oscillating system.

A plate designed with the aim of enforcing the acting lift forces on the cylinder surface due to flow separation would require a high plate thickness ($d_{Plate}/d_{Cylinder} \geq 1.3$), a moderate vertical displacement to enable a transient oscillation at low cylinder/plate gaps ($\pm 0.2 \leq h_0/d_{Cylinder} \leq \pm 0.4$) and moderate to high turbulence intensities ($4.9\% \leq Tu \leq 7.5\%$). The level of vertical displacement and plate thickness contradict each other in case of a rigidly mounted system because the high blocking ratio of the thick plate causes low separation angles that contribute to low separation angles where a vertical displacement acts contrary. Given an elastically mounted system, this conflict resolves due to the vertical movement of the cylinder. The optimal Reynolds number represents a parameter that should be designed in accordance to the eigenfrequency of the cylinder-spring-system.

To verify the found dependencies, further numerical and experimental investigations in the optimum configuration are necessary by applying the defined optimal parameter levels to an elastically mounted system. With regard to a practical application of the cylinder/plate configuration instead of a single oscillating cylinder, energetic considerations are necessary. The attached plate reduces the vortex shedding frequency of the system and thus the strokes per time but the amplitudes of each stroke increases and the system is more stable because of the previously described 'lock-in' effect in Section I. Of question is whether the increased amplitudes compensate for the loss in frequency.

REFERENCES

- [1] K. Raghavan. *Energy Extraction from a Steady Flow Using Vortex Induced Vibration*. Ph.D. Dissertation, University of Michigan, USA, 2007.
- [2] K. Siebertz. *Statistische Versuchsplanung*. VDI-Book, Springer-Verlag, Heidelberg, Berlin, Germany, 2010. DOI 10.1007/978-3-642-05493-8_11
- [3] R. Heinze, S. Beckers, T. Wahl and F. Kameier. *Enforcement of Flow-Induced Oscillations of a Circular Cylinder due to Interference Effects – Numerical Simulations and Experimental Studies*. AIAA Paper: 2013. DOI 10.2514/6.2013-3096
- [4] D. Haase. *Ein neues Verfahren zur modellbasierten Prozessoptimierung auf der Grundlage der statistischen Versuchsplanung am Beispiel eines Ottomotors mit elektromagnetischer Ventilsteuerung*. Ph.D. Dissertation, TU Dresden, Dresden, Germany, 2004.
- [5] J. Munk. *Design of Experiments*. Online-Article, Six Sigma Daily, Tampa, USA, 2013.
- [6] D. Sumner. *Two circular cylinders in cross-flow: A review*, Paper in Journal of Fluids and Structures , University of Saskatchewan, Saskatchewan, Canada: 2010. DOI:10.1016/j.jfluidstructs.2010.07.001
- [7] M. Winkler, K. Becker, C. Doolan, F. Kameier. *Aeroacoustic Effects of a Cylinder–Plate Configuration*. AIAA Paper: 2012. DOI: 10.2514/1.J051578
- [8] R. Heinze. *Experimentelle und numerische Untersuchung von Interferenzeffekten bei Zylinderumströmungen*, Ph.D. Dissertation, TU Berlin, Berlin, Germany: 2015.



**Journal of Energy Challenges
and Mechanics**

ISSN 2056-9386

<http://www.nscj.co.uk/JECM/>

Editor:

Dr. Henry Tan
University of Aberdeen, Scotland, United Kingdom

Scope:

Since James Watt, a Scottish inventor, improved efficiency of the steam engine, human civilization relies more and more on a steady supply of energy. Today we are at a transitional age. On the one hand, we see technology advances in the exploration and development of oil and gas, a depleting resource; we see growth in handling aging and decommissioning. On the other hand, we see ideas and plans for new energy infrastructure. This journal is about energy challenges and the underlying mechanics, involving multiple disciplines in science, technology, management and policy-making. Mechanics, fundamentally, is about force and the related behaviours, where force is about relationships, including those physical, human and social. For mechanics, the journal covers interactive boundaries with many other disciplines. For energy, topics include both fossil fuels and many different forms of renewable energy; also, issues related to energy economy, energy policy, efficiency, safety, environment and ecology will also be covered.



Cove Bay, Aberdeen, Scotland, United Kingdom